トロイダル双極子共鳴を有するシリコンメタサーフェスの開発と応用

長谷部，宏明

(Degree)
博士（工学）

(Date of Degree)
2024-03-25

(Date of Publication)
2025-03-01

(Resource Type)
doctoral thesis

(Report Number)
甲第8932号

(URL)
https://hdl.handle.net/20.500.14094/0100490157

博士論文

トロイダル双極子共鳴を有する
シリコンメタサーフェスの開発と応用

2024 年　1 月

神戸大学大学院工学研究科

長谷部　宏明

Abstract

Metasurfaces have emerged as a new type of optical component composed of 2-D arrays of sub-wavelength electromagnetic structures. For the optical region, optical nanoantennas are used as the building blocks. They provide efficient manipulation of the light in a nanoscale by their resonances. Recently, in addition to the fundamental modes (*i.e.* electric and magnetic multipole), a toroidal dipole mode has attracted attention because this mode can efficiently confine electromagnetic fields in nanoscale. This is useful for light-matter interaction enhancement. Although the applications of toroidal dipole metasurfaces have rapidly emerged in a few years, the practical applications have still been explored. In this thesis, we develop a metasurface which shows a toroidal dipole resonance (Chapter 2) and demonstrate their applications (Chapter 3 to 6).

In Chapter 1, general information of metasurfaces is provided. First, we summarize the fundamentals and capabilities of optical nanoantennas which are very important to obtain desired optical responses of metasurfaces. Following nanoantennas' knowledge, we provide the recent progresses of the metasurface.

In Chapter 2, we propose a metasurface composed of two- dimensional hexagonal array of very thin Si nanodisk supporting toroidal dipole mode. In calculations, we find strong electromagnetic field enhancement, which results in absorption enhancement (120-fold) compared to a same thickness Si flat film. From the field distributions and multipole decomposition analyses, we reveal that toroidal dipole modes which are induced inside individual nanodisk and inter-nanodisks cause the strong electromagnetic field confinement. Following the design of the structure by numerical simulations, we develop the metasurfaces. We exploit a colloidal lithography technique to fabricate large-area metasurfaces composed of hexagonal arrays of Si nanodisks. We demonstrate the 30-fold absorption enhancement and the tunability of the absorption wavelength in a wide range (670 ~ 858 nm).

In Chapter 3, we observe the photoluminescence enhancement from near-infrared emitting quantum dots placed on top of the metasurface. We conduct the lifetime measurement and the angle-resolved PL spectroscopy to reveal the origin of the PL enhancement. From these results and numerical simulations, we demonstrate that the out-of-plane emission is strongly enhanced by the metasurface, which results in enhanced detection efficiency.

In Chapter 4, we try to enhance the S-T direct excitation of Ru complex by a magnetic field enhanced by a toroidal dipole resonance. We control the wavelength of toroidal dipole resonances from the tail of S-S absorption to the S-T transition energy of Ru complex and conduct photoluminescence excitation measurement of Ru complex on Si metasurfaces. We experimentally demonstrate photoluminescence is 35-fold enhanced at the S-T transition energy where photoluminescence of Ru complex on the silica substrate (reference) is very small. In Chapter 5, we develop a functional metasurface composed of a thin Si nanodisk array and photosensitizing molecules as a photochemical reaction platform. For a model reaction, we examine the performance of this functional metasurface by detecting singlet oxygen ($^1O_2$) generated via Dexter energy transfer from the T_1 state of $RuPc(py)_2$ under the illumination of photons corresponding to the direct $S_0 \rightarrow T_1$ transition energy. We demonstrate enhancing photosensitizer activity under ~400 meV below the S-S transition.

In Chapter 6, we study a hexagonal array of low-aspect-ratio silicon nanodisks formed on a silicon thin film for a photodetection below Si bandgap as one of the applications utilizing a large confined electric field of a toroidal dipole resonance. The field confinement brings about narrow-band absorption when the extinction coefficient (κ) is very small, *e.g.,* $\kappa = 10^{-2} \sim 10^{-3}$. This suggests that defect-related sub-band gap absorption of silicon can be enhanced by utilizing the modes. At the resonance wavelengths, the photocurrent is substantially enhanced; the enhancement factor reaches 30-fold at around 1300 nm which is below the band gap of Si. The observed narrow-band photodetection can be used as a current-detection-type refractive index sensor operating in the near infrared range.

In Chapter 7, we summarize all results and present future outlook.

Acknowledgement

First of all, I would like to thank Prof. Minoru Fujii for being my advisor through my laboratory life. His support helped me to overcome a lot of problems in my experiments, come up with new ideas, write papers, make presentations, and so on. These experiences should be helpful in my future life.

I appreciate Associate Professor Hiroshi Sugimoto. From his attitude, I learned not only the knowledge of nanophotonics but also important things for research such as thinking deeply but taking action.

I also thank Associate Professor Taniyuki Furuyama at Kanazawa university for synthesizing ruthenium complexes. One of our research topics, developing a metasurface for the photochemical platform application, wouldn't be a success without his support.

I thank Prof. Guillermo P. Acuna, Dr. Karol Kołątaj, and Nicole Siegel Navarro for all their support of research at University of Fribourg in Switzerland. It was great experience for me to learn a lot about DNA origami and enjoy the life.

Finally, I appreciate all people who are related to me.

Contents

Abstract ii
Acknowledgement v
Chapter 1 Introduction of Metasurface 1
1.1 Optical Nanoantenna 2
1.1.1 Mie Scattering 2
1.1.2 Toroidal Multipole Mode 5
1.1.3 Function of Optical Nanoantennas 7
1.2 Metasurface 15
1.2.1 Metasurface using Electric and Magnetic Resonances 15
1.2.2 Metasurface using Toroidal Dipole Resonance 18
1.3 Chapter Overview 19
Chapter 2 Toroidal Dipole Resonance in Si Nanodisk Hexagonal Array 22
2.1 Numerical Simulations 22
2.1.1 Single Si Nanodisk 22
2.1.2 Si Nanodisk Hexagonal Array 24
2.2 Fabrication of Si Nanodsik Hexagonal Array 33
2.3 Transmittance, Reflectance, and Absorptance Spectra 38
2.4 Conclusion 41
PART I : Light-Matter Interaction Enhancement by Toroidal Dipole Resonance 42
Chapter 3 Purcell Enhancement and Emission Directional Control 42
3.1 Experimental Methods 42
3.2 Results and Discussion 45
3.3 Conclusion 51
Chapter 4 Singlet-Triplet Direct Transition Enhancement of Molecules by Magnetic Field Enhancement 52
4.1 Experimental Methods 54
4.2 Results and Discussion 58
4.3 Conclusion 68
Chapter 5 Enhancement of Singlet Oxygen Generation Efficiency 70
5.1 Experimental Methods 71
5.2 Results and Discussion 74
5.3 Conclusion 80
PART II : Optelectronic Device Application Utilizing Toroidal Dipole Resonance 82
Chapter 6 Toroidal dipole-induced photocurrent enhancement below the band gap 82
6.1 Numerical Simulations 84
6.1.1 Structures and Parameters 84

6.1.2 Mode Assignment 85
6.1.3 Absorption with Different Extinction Coefficient 88
6.2 Experimental Methods 94
6.3 Results and Discussion 95
6.4 Conclusion 100
Chapter 7 Summary and Outlook 101
Reference 103
List of Achievement 116
Publications 116
Conference 116
Award 118

Chapter 1

Introduction of Metasurface

Electromagnetic wave manipulations in the optical frequency range are traditionally realized by bulk optical elements such as lens, prism, mirror, diffractive grating, and fiber. They have been widely used and still being improved, while their geometrical sizes and focus spot are restricted due to the diffraction limit ($\sim\lambda/2$). Additionally, we have to combine several optical elements to obtain desired profiles (*e.g.* we need a linear polarizer and a $\lambda/4$ plate to realize circular polarized beam), which becomes an obstacle to their miniaturization and realizing integrated photonic circuits.

Metasurfaces have emerged as new type of optical components composed of 2-D arrays of sub-wavelength electromagnetic structures, known as metamaterial or meta-atom. They need only a few hundred nanometers or less in the thicknesses, which breaks the diffraction limit and opens "flat optics"[1]. A lot of configurations (*i.e.* homogeneous or gradient array, period, the material, and the shape of meta-atoms) of metasurfaces have been already proposed from microwave to visible range to realize desired optical properties. The implementations and capabilities of metasurfaces are summarized in **Figure 1-1**. The subjects of metasurfaces are categorized as nearfield (electromagnetic field) enhancement, wavefront control, and slow light management (waveguide). From them, lots of targets and applications derive as shown in Figure 1-1. The development of metasurfaces is rapidly growing by developing nanofabrication technologies such as an electron beam lithography, and now, a company commercially starts to sell "meta"-lenses consisting of optical nanoantennas.

To fabricate metasurfaces for optical frequency range, they are constructed by "optical nanoantennas" as metamaterials. The size of nanoantennas is from a few ten to several hundred nanometers, which is below the diffraction limit. The concept of optical nanoantennas is similar

to well-established antennas for radio frequency such as Yagi-Uda antennas and parabolic antennas. In analogy to its radiowave and microwave counterparts, an optical antenna is defined as "*a device designed to efficiently convert free-propagating optical radiation to localized energy, and vice versa*"[2]. Optical nanoantennas realize this role with their optical resonances, which are very important to design metasurfaces. In this chapter, we introduce fundamental knowledge of nanoantennas and the recent progress of metasurfaces.

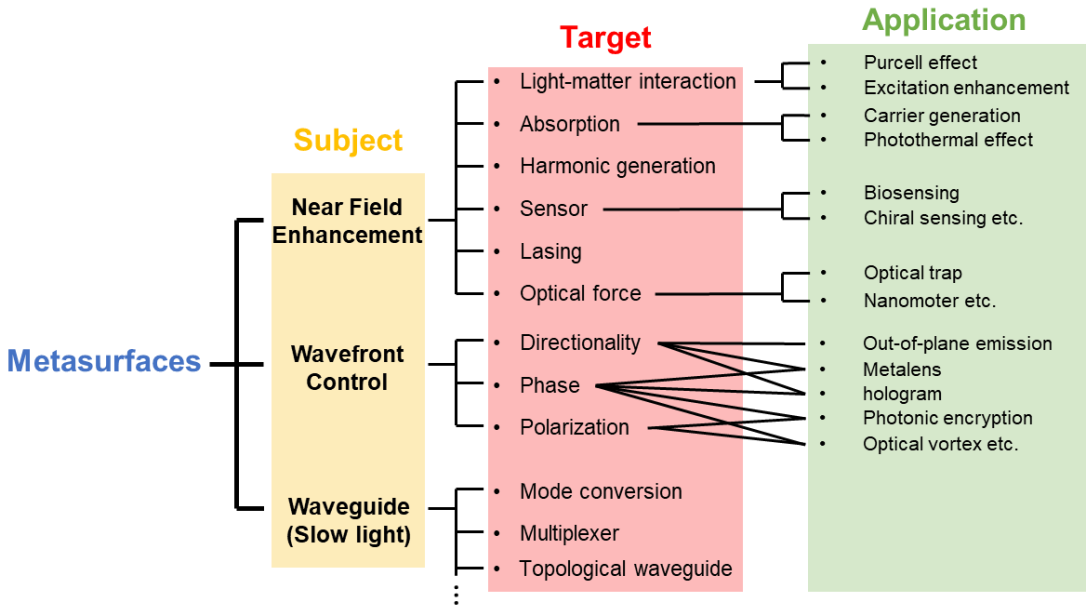

Figure 1-1 *Implementations and capabilities of metasurfaces*

1.1 Optical Nanoantenna

1.1.1 Mie Scattering

The scattering and absorption light by a particle are calculated by Maxwell's equations when a particle becomes as small as the light wavelength. In 1908, Gustav Mie developed the theory about the scattering and absorption light problem of the particle that is perfect sphere and put in a vacuum[3]. They are written as:

$$Q_s = \frac{2}{(k_0 r)^2}\sum_{l=1}^{\infty}(2l+1)(|a_l|^2 + |b_l|^2)\ \ (scattering\ efficiency)\ , \tag{1}$$

$$Q_{ext} = \frac{2}{(k_0 r)^2}\sum_{l=1}^{\infty}(2l+1)Re(a_l + b_l)\ \ (extinction\ efficiency), \tag{1}$$

$$Q_{abs} = Q_{ext} - Q_{sca}\ (absorption\ efficiency), \tag{2}$$

where r is the radius of the particle, k_0 is the k vector of incident light, respectively. a_l and b_l are called "Mie coefficients", expressed by

$$a_l = \frac{n^2 j_l(nk_0 r)[kr_0 j_l(k_0 r)]' - j_l(k_0 r)[nk_0 r j_l(nk_0 r)]'}{n^2 j_l(nk_0 r)[kr_0 h_l(k_0 r)]' - h_l(k_0 r)[nk_0 r j_l(nk_0 r)]'}, \tag{3}$$

$$b_l = \frac{j_l(nk_0 r)[kr_0 j_l(k_0 r)]' - j_l(k_0 r)[nk_0 r j_l(nk_0 r)]'}{j_l(nk_0 r)[kr_0 h_l(k_0 r)]' - h_l(k_0 r)[nk_0 r j_l(nk_0 r)]'}, \tag{4}$$

where n is the complex refractive index of the particle, j_l is the first spherical Bessel function, and h_l is the first spherical Hankel function, respectively. Although they seem very complex, we can derive them from the equation of the boundary condition between the particle and the surrounding medium.

The Mie coefficients express electric and magnetic radiation field patterns. **Figure 1-3** shows the field distributions from each Mie coefficient ($l = 1,2$). They show two different type modes. a_l shows the transverse magnetic (TM) modes which have no radial magnetic field components. We conventionally call them electric multipole mode (*i.e.* electric dipole (ED) and electric quadrupole (EQ) mode from the lowest order) because of the number of electric field nodes. In contrast, b_l shows the transverse electric (TE) modes which have no radial electric field components. We call them magnetic multipole mode (*i.e.* magnetic dipole (MD) and magnetic quadrupole (MQ) mode from the lowest order) because of the number of magnetic field nodes.

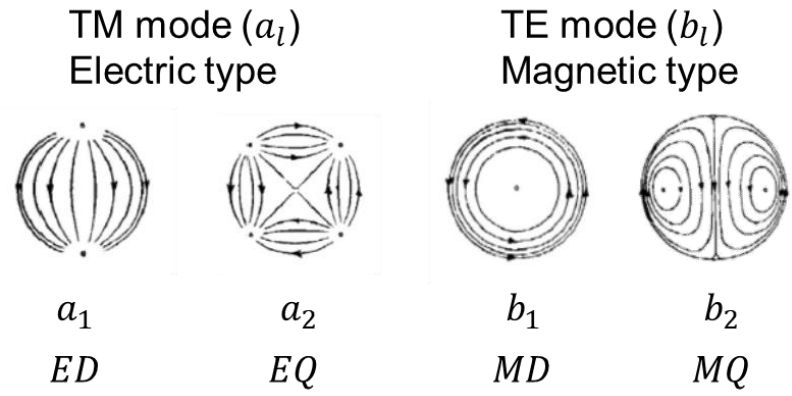

Figure 1-3 *Electric field patterns of normal modes*[3]

For optical nanoantennas, there are two material choices: metals (*e.g.* Au, Ag, Al) and high refractive index dielectrics (*e.g.* Si, GaP, Ge). Both nanoantennas have unique optical responses, but they are totally different. **Figure 1-2** shows the scattering spectra of gold (Au) and silicon (Si) nanosphere with 140 nm in diameter calculated by Mie scattering theory (eq.(1)). Au nanosphere has only one peak, while Si nanoantenna has two peaks. In the case of metal nanoantennas, the resonances stem from the collective oscillation of free electrons by incident electric field, well-known as localized surface plasmon resonance[4] (LSPR) which is an electric type resonance (a_l). To realize magnetic response with plasmonic nanoantennas, split ring, U and V shape nanoantennas that can create circulating currents by the electrons oscillation induced by LSPR have been proposed[5–8]. On the other hand, a high-refractive index dielectric nanoantenna has not only the electric type resonances but also the magnetic type resonances when $2r = \lambda/n$

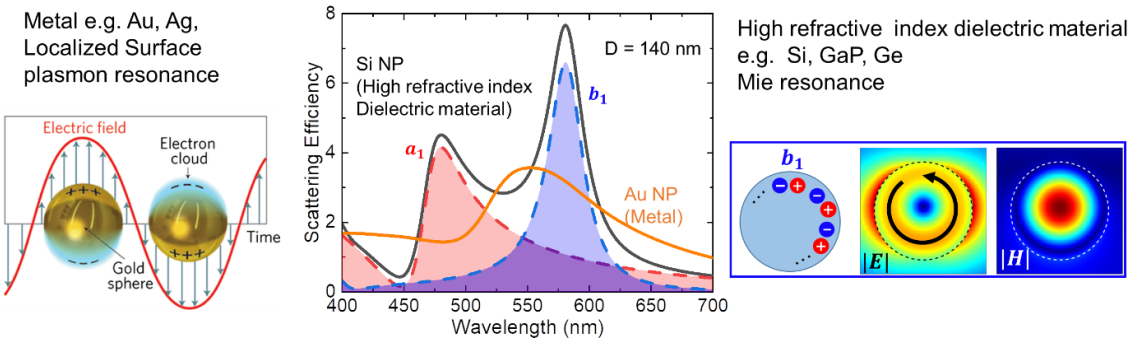

Figure 1-2 *Scattering spectra of (orange)Au and (black) Si nanosphere with 140 nm in diameter.* [4]

even though it is a very simple structure. This is because of the coupling of incoming light to the circular displacement currents of the electric field[9]. The resonances induced by dielectric nanoantennas are called “Mie resonance”. Mie resonances clearly appear when the refractive index of the material is over 2 and low-loss[9], such as TiO_2, Si, GaP, and so on[10,11].

1.1.2 Toroidal Multipole Mode

The field distribution of toroidal mode consists of a poloidal current on the surface of a torus and a magnetic dipole loop inside it[12](**Figure 1-4**). Since Y.B Zeldovich introduced it to explain the nonradiation state in 1957[13], toroidal multipoles have been handled in the field of nuclear[14–16], and solid state physics[17–19]. Also in nanophotonics, toroidal multipole mode has been recently considered as the third multipole family in addition to electric and magnetic multipole modes[20–24].

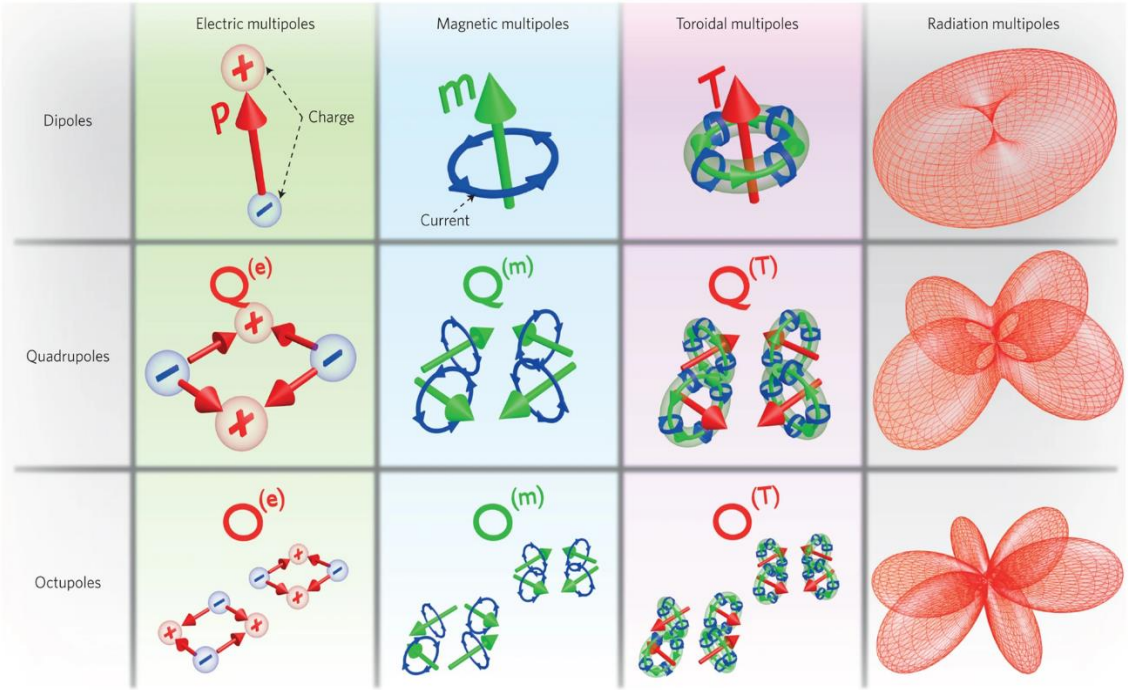

Figure 1-4 *Schematic image of electric, magnetic, and toroidal multipole modes*[12]

However, there is a controversy if the toroidal mode is an exact mode or not[25–27]. Toroidal moment terms don't appear in Mie scattering theory. This is because the radiation pattern (farfield contribution) of toroidal mode is the same as that of the electric mode and we cannot and don't distinguish them in the derivation of Mie scattering theory that uses the boundary condition. When we focus on the displacement current $\boldsymbol{J}(\boldsymbol{r})(= -i\omega\varepsilon_0(\varepsilon-1)\boldsymbol{E}(\boldsymbol{r}))$ in the structure (nearfield contribution), the electric dipole moment[28] is written as:

$$\boldsymbol{p_{exact}} = -\frac{1}{i\omega}\left\{\int \boldsymbol{J}(\boldsymbol{r}) j_0(kr) d^3\boldsymbol{r} + \frac{k^2}{2}\int 3\big(\boldsymbol{r}\cdot\boldsymbol{J}(\boldsymbol{r}) - r^2\boldsymbol{J}(\boldsymbol{r})\big)\frac{j_2(kr)}{(kr)^2} d^3\boldsymbol{r}\right\}, \tag{5}$$

where ε_0 and ε are the dielectric constant of vacuum and relative permittivity, and $\boldsymbol{E}(\boldsymbol{r})$ is the electric field inside the structure. In long-wave approximation, the above equation is written as:

$$\boldsymbol{p_{exact}} \sim -\frac{1}{i\omega}\left\{\int \boldsymbol{J}(\boldsymbol{r}) d^3\boldsymbol{r} + \frac{k^2}{10}\int \Big(\big(\boldsymbol{r}\cdot\boldsymbol{J}(\boldsymbol{r})\big)\boldsymbol{r} - 2r^2\boldsymbol{J}(\boldsymbol{r})\Big) d^3\boldsymbol{r}\right\} \tag{6}$$

The first term is corresponding to the electric dipole moment in the Cartesian coordinate, while the second term is the toroidal dipole moment. This is a reason why the toroidal mode is considered as third multipole family. In fact, the toroidal mode has a different *time* and *space* symmetry from electric and magnetic modes[29,30] (**Table 1**), which is also one of the reasons. Recently, strong toroidal dipole responses[31–34] have been achieved in nanoantennas (metamaterials), and it is very important to consider three types multipoles for desired functions.

Table 1 *Electric($\vec{p}$), magnetic ($\vec{m}$), and toroidal ($\vec{t}$) dipole's behavior under time and space symmetry. "+" and " –" means "even" and "odd", respectively. $\vec{g}$ is "axial" toroidal dipole moment which originates in poloidal magnetic fields and circulating electric dipole in it. We don't discuss this mode in this work because it cannot be excited by the plane wave light, basically.* [29,30]

	$\vec{p}$	$\vec{m}$	$\vec{t}$	$\vec{g}$
Space inversion $r \to -r$	−	+	−	+
Time inversion $t \to -t$	+	−	−	+

Introducing this toroidal multipole concept, we can find an interesting phenomenon "anapole state[23,35–37]", which is nonradiating state caused by destructive interference between electric and toroidal dipole mode (**Figure 1-5**). The electric and toroidal dipole moment are written with displacement current as follows:[36]

$$\boldsymbol{p} = -\frac{\mathbf{1}}{\boldsymbol{i\omega}} \int \boldsymbol{J}(\boldsymbol{r}) d^3\boldsymbol{r} \tag{7}$$

$$\boldsymbol{T} = \frac{k}{10\omega} \int \Big((\boldsymbol{r} \cdot \boldsymbol{J}(\boldsymbol{r}))\boldsymbol{r} - 2r^2 \boldsymbol{J}(\boldsymbol{r}) \Big) d^3\boldsymbol{r} \,. \tag{8}$$

Then, the total scattering field that the dipoles contribute is expressed by

$$\boldsymbol{E_{sca}} = \frac{k^2}{4\pi\varepsilon_0} \{ \boldsymbol{n} \times \boldsymbol{p} \times \boldsymbol{n} + ik\boldsymbol{n} \times \boldsymbol{T} \times \boldsymbol{n} \} \,. \tag{9}$$

When $\boldsymbol{p} = -ik\boldsymbol{T}$, which means both multipole intensities are same and they are out-of-phase, the scattering intensity becomes 0. Note that the internal displace current is non-zero. This means the incident field is confined and large field enhancement occurs in the structure. These anapole phenomena have recently been observed experimentally in a high aspect-ratio nanodisk[36].

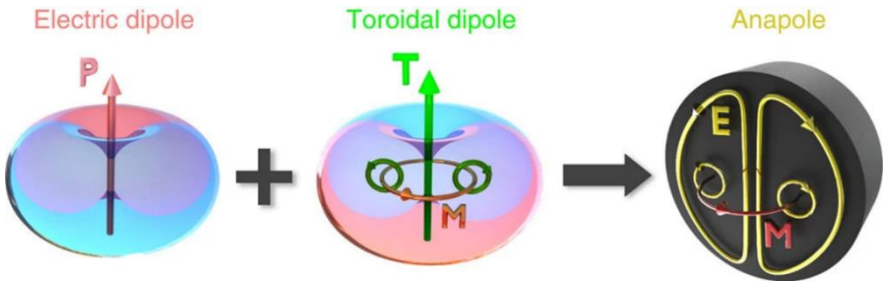

Figure 1-5 *Schematical image of emerging anapole state.* [36]

1.1.3 Function of Optical Nanoantennas

- Controlling Radiation Directionality

From Mie scattering theory, the backward (reflection) and forward (transmission) scattering intensity is described as

$$G(180^o) = \left(\frac{4}{(2\pi r/\lambda)^2}\right)\left|\sum_{n=1}^{\infty}\left(n+\frac{1}{2}\right)(-1)^n(b_n - a_n)\right|^2 \quad (backward) \tag{10}$$

$$G(0^o) = \left(\frac{4}{(2\pi r/\lambda)^2}\right)\left|\sum_{n=1}^{\infty}\left(n+\frac{1}{2}\right)(b_n + a_n)\right|^2 \quad (forward). \tag{11}$$

When $a_n = b_n$, the backward scattering is perfectly suppressed, and vice versa when $a_n = -b_n$. This effect is called "Kerker effect"[38]. In 1983, Kerker discovered the backward scattering in a magnetic sphere ($\mu \neq 1$) is suppressed when the permittivity satisfies $\varepsilon_r = \mu_r$. When we regard the particle that has Mie resonance as "meta-atom", a_n , b_n can be assumed to ε_r, μ_r, respectively. The schematic image of this effect is in **Figure 1-6**(a)[39]. The farfield radiation of an electric dipole

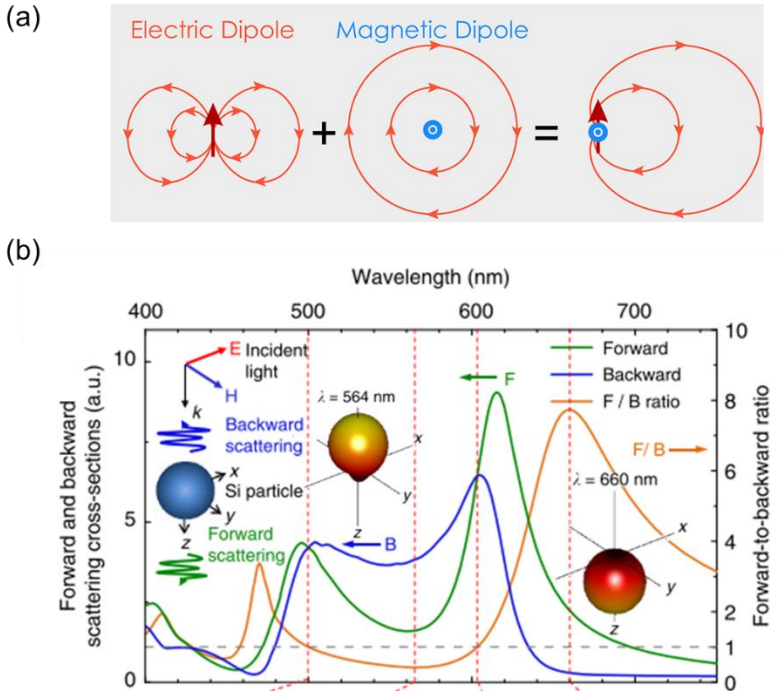

Figure 1-6 *(a)Schematic image of Kerker effect with electric and magnetic dipole interference*[39]*. The arrows in field patterns indicate the vector of electric field. (b) the forward and backward scattering and forward-to-backward ratio (F/B) spectra of a Si nanosphere with 150 nm in diameter*[40]*.*

constructively interferes with that of a magnetic dipole in the forward, while it destructively interferes in the backward. Figure 1-6(b) shows the forward and backward scattering and forward-to-backward ratio (F/B) spectra of a Si nanosphere with 150 nm in diameter[40]. The scattering spectra are different between forward and backward because of the interference between electric and magnetic modes. In the F/B spectrum, we can see the directionality is strongly enhanced at 660 nm (forward) and 564 nm (backward), where $a_1 = b_1$ and $a_1 = -b_1$ are respectively satisfied. Recently, to realize arbitrary directional scattering not only forward and backward with multipole interference, a lot of structure are proposed such as asymmetric dimers[41,42], hetero dimers[43,44], U (V) shape nanoantennas[45,46].

Controlling radiation properties is important not only for scattering but also for quantum emitters(*e.g*. quantum dots and organic dyes). The emission control from quantum emitters is very important to improve the collection efficiency because of reducing undesired losses such as the radiation out of N.A. of a lens and that into the substrate. First, Yagi-Uda type nanoantenna[47] which mimics a conventional radio frequency antenna was proposed. It consists of some nanoantennas as a reflector, a feed, and directors (**Figure 1-7**(a)). Curto *et al.* first demonstrated the unidirectional emission with plasmonic Yagi-Uda nanoantenna from quantum dots experimentally in 2010[48]. Alexander *et al.* also proposed a dielectric Yagi-Uda nanoantenna which is low-loss and can achieve high diresctionality[49]. After that, more compact nanoantennas for unidirectional emission have been proposed. The one is a metal nanoantenna dimer. When an emitter is put on precise position, it couples with LSPRs of two metal nanoantennas with the phase delay, which results in the unidirectional emission[50] (Figure 1-7(b)). Recently, Acuna's group experimentally demonstrated this effect with a gold nanorod dimer constructed on DNA origami[51]. Another is a nanoantenna that has magnetic responses such as high-refractive index dielectric nanoantennas[49,52,53], metal nanoparticle trimers[54,55], and so on. In this case, the electric dipole emitter coherently excites the electric and magnetic dipole resonances, which results in canceling out a certain direction radiation of the exciting dipole source. Cihan *et al.* demonstrated 25-fold

enhanced top-to-bottom emission ratio from MoS_2 on a silica substrate with Si nanowire compared to that without a nanoantenna (Figure 1-7(c))[53].

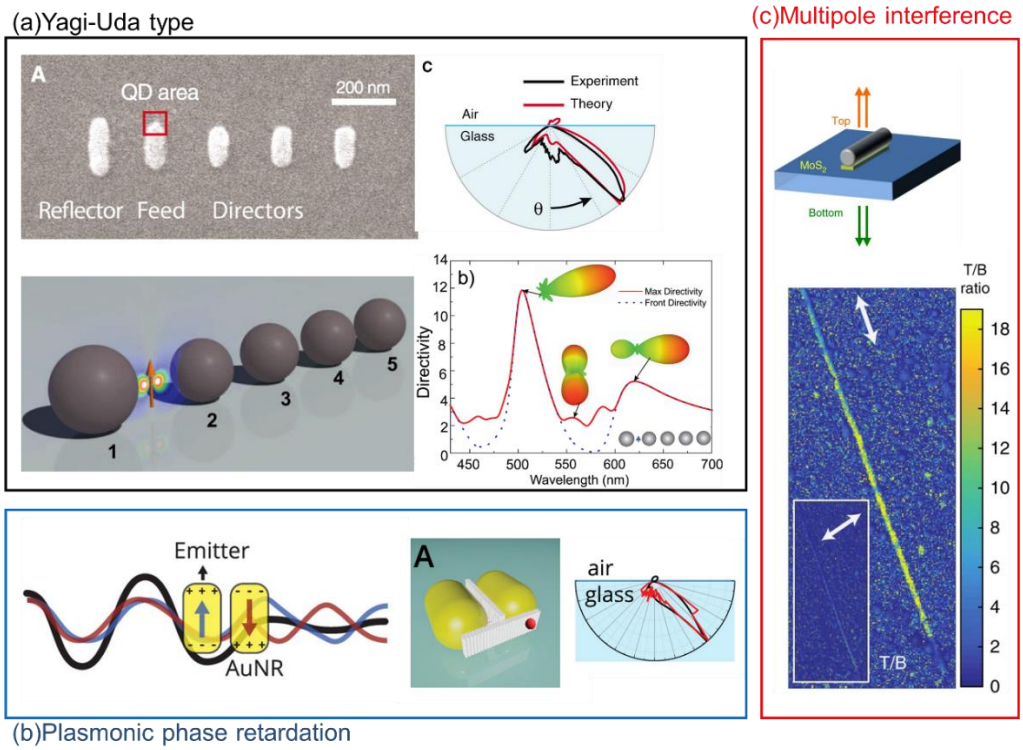

***Figure 1-7** 3 types of controlling radiation nanoantennas (a)Yagi-Uda nanoantenna[48,49] (b) plasmonic phase reterdation[51] (c) multipole interference[53]*

- Spontaneous emission enhancement (Purcell effect)

E. M. Purcell theoretically discovered that the relaxation time of nuclear magnetic moment transition is promoted from ~10^{21} sec to a time of the order of minutes when a nuclear magnetic medium and small metallic particles are mixed[56]. The first observation was in 1970 by K.H Drexhage. He demonstrated that the decay time of Eu^{3+} ions on a silver mirror can be modified by changing the distance between the emitter and the mirror[57]. This effect is called "Purcell effect". The enhancement factor of a spontaneous emission probability (Purcell factor) is written as follow:

$$f = \frac{3\left(\frac{\lambda}{n}\right)^3}{4\pi^2} \cdot \frac{Q}{V}, \tag{12}$$

where λ is a wavelength, n is the refractive index of the medium, Q is the quality factor, and V is the mode volume. This factor relates to the increase in the photonic density of states. The schematic image is shown in **Figure 1-8**(a). The new relaxation passes of the emitter, regardless of whether radiating or non-radiating passes, are introduced by a cavity, resulting in promoting the decay rate. In an experiment, this factor can be determined by the decay rate obtained by lifetime measurement, γ_{cav}/γ_0. Note that γ_{cav} includes both radiative and non-radiative decay rates.

Quantum emitters have mainly two kinds of transitions: electric dipole transition (*e.g.* typical molecules, quantum dots) and magnetic dipole transition (*e.g.* rare earth ion). Optical nanoantennas have been required to enhance both transition emissions. In the case of electric dipole transition, both plasmonic and dielectric nanoantennas show a strong Purcell effect[58–61]. Using a gap between a plasmonic nanoparticle and a mirror, over 800 of Purcell factor was achieved[59], while enhancing and modifying fluorescence spectra were achieved with a dielectric nanoantenna thanks to the sharp multipole resonances and low-loss nature in the optical frequency, which results in a radiative decay rate enhancement[58]. Dielectric nanoantennas also get attention for enhancing magnetic dipole emission because they have magnetic multipole resonances, and the magnetic Purcell effect is theoretically predicted with arbitrary shaped dielectric nanoantenna[62–65]. Recently, magnetic dipole transition has been experimentally observed with a composite structure of Eu^{3+} complex with Si nanosphere[66].

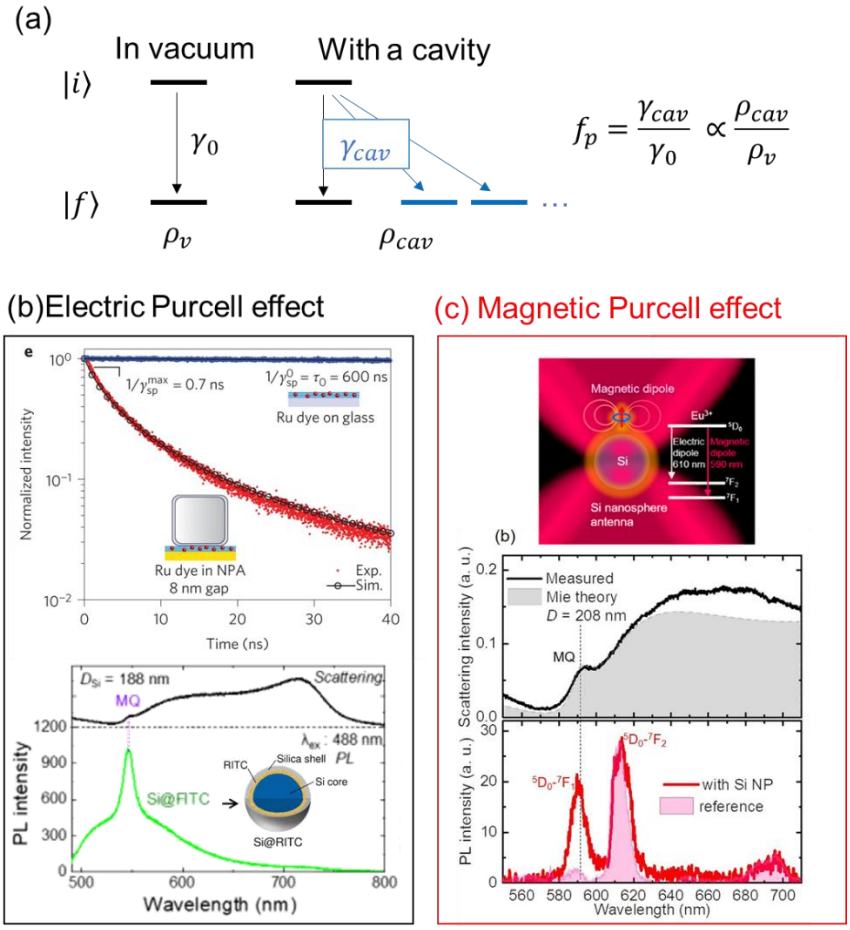

Figure 1-8*(a)Schematic image of increasing the density of states. (b)Purcell effect of an electrc dipole transition with a plasmonic*[59] *(up) and a dielectric nanoantenna*[58] *(bottom). (c)Experimental proof of magnetic Purcell effect with dielectric nanoantenna*[66].

- Field enhancement

Optical nanoantennas generate strong electromagnetic field in their nearfield because the light is confined in the region smaller than the wavelength (below the diffraction limit), which realizes strong light-matter interaction that is impossible with bulky optical lens.

*(a) Excitation enhancement of other materials (***Figure 1-9** *(a))*

The excitation rate of an emitter can be described with Fermi's golden rule,

$$\gamma_{i\to f} = \frac{2\pi}{\hbar}|\langle f|\mathcal{H}|i\rangle|^2\rho_f, \tag{13}$$

where $|i\rangle$ and $|f\rangle$ indicate an initial and a final state, ρ_f is the density of state of the final state, respectively. $\mathcal{H}$ is the light-matter interaction Hamiltonian written as

$$\mathcal{H} = -\boldsymbol{p}\cdot\boldsymbol{E}(\boldsymbol{r}) - \boldsymbol{m}\cdot\boldsymbol{B}(\boldsymbol{r}) - [\boldsymbol{q}\boldsymbol{\nabla}]\cdot\boldsymbol{E}(\boldsymbol{r}) - \cdots, \tag{14}$$

where $\boldsymbol{p}, \boldsymbol{m}$, and $\boldsymbol{q}$ are an electric and a magnetic dipole transition moment and electric quadrupole tensor, and $\boldsymbol{E}(\boldsymbol{r})$ and $\boldsymbol{B}(\boldsymbol{r})$ are electric and magnetic fields at the emitter position, respectively. In general, we consider only the first term because other terms' contributions are several orders smaller (*i.e.* electric dipole approximation), and the emitted light intensity is proportional to $|\boldsymbol{E}|^{2n}$ for a n-photon process[67]. Nanoantennas can generate electric field enhancement outside themselves, which contributes to increasing the excitation efficiency of the materials at the vicinity of nanoantennas.

However, the high order term (*i.e.* magnetic dipole, electric quadrupole transition) mainly contributes to the molecular excitation when the electric dipole transition is forbidden such as the $S_0 \rightarrow T_1$ transition of molecules. For example, the excitation rate depends on $|-\boldsymbol{m}\cdot\boldsymbol{B}|^2$ in the magnetic dipole transition. From this point of view, dielectric nanoantennas are very attractive because the optical magnetic field is greatly enhanced at the magnetic multipole resonances, which opens magnetic light-matter interaction. However, we have not utilized this field because it is localized inside the structure. In chapter4 and 5, we develop a metasurface that has an accessible enhanced magnetic field and apply it to a new photochemical platform.

(b) Self-Absorption enhancement

The nanoantennas, especially dielectric ones with magnetic multipole resonances, create an enhanced electric field inside the structures, which results in absorption enhancement because the absorbed power is proportional to $\kappa|\boldsymbol{E}|^2$, where κ is the extinction coefficient. The efficient light absorption of semiconductors (e.g. Si, TiO_2) is essentially for photocarrier generation that can be used for photodetection[68–71], photocatalyst[72], photothermal effect[73–75] ,and higher harmonic generation[22,76,77].

(c) Optical force

When the particle is irradiated by the light, it feels some pressure known as "optical force". This force occurs by the interaction between the electric dipole of the particle and the electric field of the light. Arthur Ashkin *et al.*, who got a Novel prize in 2018, first demonstrated the particle trapping by a tightly focused beam, known as "optical tweezer"[78]. Optical force is now used for widespread applications like manipulating nanoparticles, biomolecules, and so on.

Time averaged optical force is expressed by [79,80]

$$\langle \boldsymbol{F} \rangle = \frac{\alpha'}{4} \boldsymbol{\nabla}(\boldsymbol{E}^* \cdot \boldsymbol{E}) + \frac{c k_0 \alpha''}{\varepsilon_0} \left(\frac{1}{c^2} \langle \boldsymbol{S} \rangle + \boldsymbol{\nabla} \times \langle \boldsymbol{L_s} \rangle \right), \tag{15}$$

where c is the speed of light, k_0 is the absolute value of the wavevector, $\boldsymbol{E}$ is the sum of the incident and scattered electric field, $\langle \boldsymbol{S} \rangle$ is the total Poynting vector, $\langle \boldsymbol{L_s} \rangle$ is the average spin angular momentum, and α' and α'' are the real and imaginary parts of the particle dipole polarization. The first term describes the gradient force which means dragging the particle toward the maximal field intensity region when $\alpha' > 0$. The nanoantennas can manipulate a single particle with subwavelength scale and low laser power intensity because they can confine the electric field below the diffraction limit[81–84]. The second term is curl-spin force related to optical torque. Recently, it has been theoretically reported that the optical nanovortex can be realized by a Si nanoantenna, which is expected for a plethora of applications in microfluidics and lab-on-a-chip devices[80].

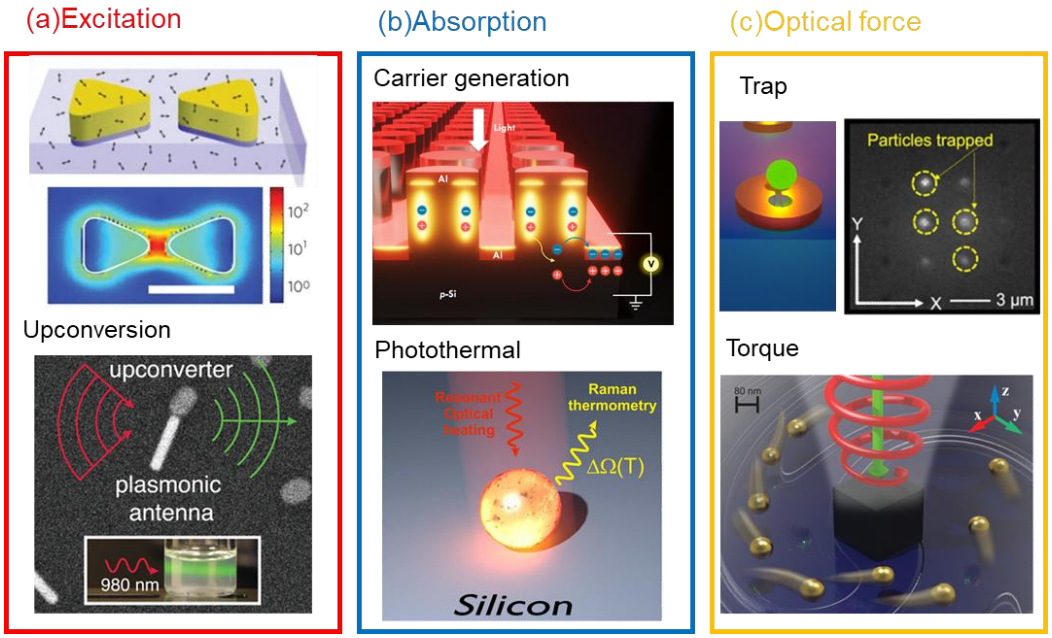

Figure 1-9 *Application of field enhancement(a)excitation enhancement by electric field induced by nanoantennas*[67,201]*, (b)absorption enhancement*[69,75]*, (c)Optical force*[80,81]

1.2 Metasurface

Metasurfaces maximize a capability of single nanoantenna and exploit them to develop new optical elements. Up to now, a lot of applications have been proposed and demonstrated. Here, we introduce the recent progress of metasurfaces from two aspects: using electric and magnetic resonances and toroidal dipole resonances.

1.2.1 Metasurface using Electric and Magnetic Resonances

- Metalens (Wavefront control)

The most commercially attractive application of metasurfaces is metalens[85–89]. This can miniaturize the optical components in cameras or some detecting devices, reduce noises, and elicit optical information such as polarization and phase. There are two types of metalens; a phase gradient and a scattering modification type. The first one is composed of some different shape nanoantennas. Their resonances are controlled to generate 2π phase shift gradually in the unit cell,

which results in bending the wavefront of incident light[90,91](**Figure 1-10**(a)). The latter one uses the uni-directional scattering of nanoantennas. Compared to the former one, it needs smaller unit cells keeping bending and transmittance efficiency. Dominguez *et. al* demonstrated over 0.99 numerical aperture lens can be realized using this concept[92] (Figure 1-10(b)).

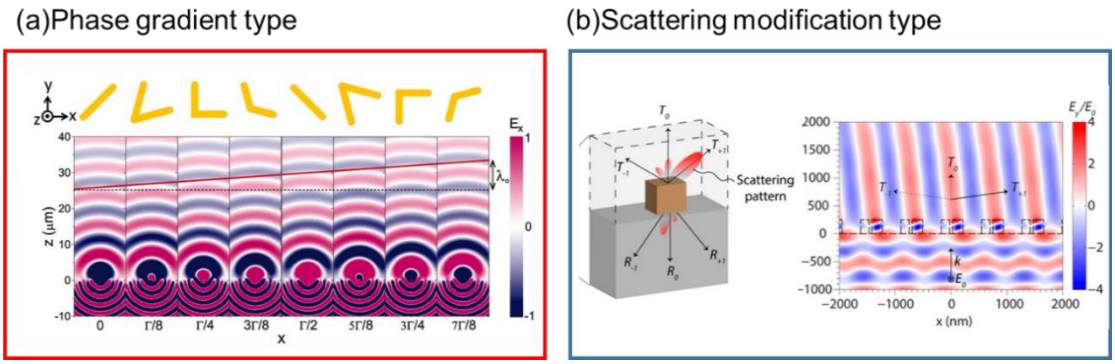

Figure 1-10 *2 types of metalens (a)Phase gradient type*[91]*. (b) Scattering modification typenanoantenna*[92]

- Coupling with quantum emitters

Although the individual nanoantennas have the capability of PL modulation, metasurfaces are also very attractive platforms because they exploit interference between each nanoantennas[93,94], surface lattice resonances[95–98], and embedded eigenstates known as the bound state in the continuum (BIC)[99,100], which results in high Q resonances and extremely high electromagnetic field enhancement. Liu *et. al.* reported about 110-fold PL enhancement was observed by embedding quantum dots in nanostructures[101]. They also showed the spatial emission from the metasurface was modified corresponding to its dispersion in real space. Zhang *et. al.* simultaneously realized low threshold lasing and almost purely circular polarized emissions from a metasurface with dye doped polymer[102]. The metasurface which can make the emission from dyes an azimuth vortex beam was also proposed[103]. In addition to the abilities described above, the metasurfaces offers manifold opportunities for manipulating dipolar emitter placed at vicinity[100].

- Perfect Absorption

Realizing high absorption in ultrathin semiconductors in the visible and near-infrared regions is essential for efficiently generating photocarriers, suppressing dark currents, and developing ultrafast optoelectronic devices with low material cost[104]. In the early 1900s, some reseachers discovered the absorption upper-limit of the lossy films which are thinner than the wavelength without a backreflector is 50%[105–107]. However, metasurfaces can overcome this limit and achieve perfect absorption. From the coupled mode theory, if a metasrface supports a single resonance, the 50% power absorption is achieved when the leakage energy rates inside and outside the structures (*i.e.* the radiative and nonradiative loss) are equal, known as the critical coupling condition[108]. When a metasurface supports two opposite symmetry resonances, such as electric and magnetic dipole modes (please refer to Table 1), the stored energy is written by[109]

$$|a|^2 = \Sigma_{j=1}^{2}\left(\frac{2\delta_j\gamma_j}{\left(\omega-\omega_j\right)^2+\left(\gamma_j+\delta_j\right)^2}\right), \tag{16}$$

where γ_j and δ_j are the radiative and nonradiative loss rates and ω_j is the resonance frequency of each modes, respectively. When $\omega = \omega_j$ and $\gamma_j = \delta_j$, the absorption of each mode reaches 50%, which means total absorption .Recently, perfect absorption has been theoretically indicated with metasurfaces that have subwavelength ($\sim 0.3\lambda$) thickness[70,104,110–112] and some researchers demonstrated nearly perfect absorption[112] and improved photodetection efficiency[113]. These devices that introduce nanoantennas are expected to be integrated into on-chip optelectronics because we can reduce the size[70,104].

Additionally, a lot of applications have been proposed such as single molecule sensor[114], perfect mirror[115,116], and photonic encryption[117–119], etc.

1.2.2 Metasurface using Toroidal Dipole Resonance

Since Kaelberer *et. al.* demonstrated a pure toroidal dipole resonance with a 3D metasurface which has 4 standing sprit ring resonators in the unit cell in the microwave region in 2010[120], toroidal dipole metasurfaces in the optical region have been actively proposed. The first toroidal dipole metasurface in the optical region was numerically proposed by Huang *et. al.* using the same configuration as in microwave region but scaling down 4 split ring nanoresonators[121]. However, lateral excitation is needed to obtain a toroidal dipole resonance and the fabrication is very difficult in nanoscale[122]. On the other hand, planar toroidal dipole metasurfaces have been suggested. They can be fabricated by top-down processes easily and the toroidal dipole resonance is excited by the normal incidence light to the surface. There are two kinds of planar toroidal dipole metasurfaces which have oligomer that is composed of magnetic dipole resonance nanoantennas in a unit cell[123–126] or a single nanoantenna that has a toroidal dipole mode[127–130], respectively. These toroidal dipole metasurfaces have relatively high quality factors and high electromagnetic field enhancement compared to electric and magnetic dipole resonances, and now, the interest has changed from how to realize and observe toroidal dipole resonance to its applications[131,132]. Jeong *et.al.* demonstrated the high figure of merit (~78) refractive index sensor based on a toroidal dipole resonance experimentally[133]. Utilizing high electric field confinement, Tripathi *et.al.* demonstrated room-temperature lasing action with low threshold and high coherence[134]. Cui *et.al.* observed over 400-fold PL enhancement from Ge quantum dots embedded in Si nanodisks, but they didn't reveal the origin of the enhancement[135]. Recently, the optical trapping capability was demonstrated[136]. Although the applications of toroidal dipole metasurfaces have rapidly emerged in a few years, the practical applications have been still explored. Especially, the electric and magnetic fields are simultaneously strongly enhanced at a toroidal dipole resonance, but the enhanced magnetic field is ignored in most cases.

1.3 Chapter Overview

In this thesis, we focus on both electric and magnetic field enhancement of toroidal dipole dielectric metasurfaces and show their new applications. Chapter overview is shown in **Figure 1-11**. First of all, we propose and develop toroidal dipole metasurfaces which are composed of 2-D hexagonal aligned Si nanodisks that have a toroidal dipole mode in Chapter 2. Then, we show the application of them. In Chapter 3 to Chapter 5, we demonstrate two kinds of light-matter interaction enhancement: an electric dipole emission and a singlet to triplet transition excitation of the molecules. In Chapter 6 , we detect the photocurrent enhancement related to the defect related absorption by exploiting the strong absorption enhancement of the toroidal dipole metasurface. The details are written below.

In Chapter 2, we propose a metasurface composed of two- dimensional hexagonal array of very thin (height: 20 ~ 50 nm, diameter: 200 ~ 450 nm) Si nanodisk supporting toroidal dipole mode. In calculations, we find strong absorption enhancement (120-fold) compared to a same thickness Si flat film even though the Si volume is 26% reduced. From the field distributions and multipole decomposition analyses, we reveal that absorption enhancement arises from the highly confined field by toroidal dipole mode that is induced inside individual nanodisk and inter-nanodisks. Following the design of the structure by numerical simulations, we develop the metasurfaces in 2.2. The method of large scale fabrication of metasurfaces, which is necessary for a lot of applications, is still explored. We exploit a colloidal lithography technique to fabricate large-area metasurfaces composed of hexagonal arrays of Si nanodisks. We demonstrate the 30-fold absorption enhancement and the tunability of the absorption wavelength in a wide range (670 ~ 858 nm).

In Chapter 3, we observe the PL enhancement from near-infrared emitting quantum dots placed on top of the metasurface. We conduct the lifetime measurement and the angle-resolved PL spectroscopy to reveal the origin of the PL enhancement. From these results and numerical

simulations, we demonstrate that the out-of-plane emission is strongly enhanced by the metasurface, which results in enhanced detection efficiency.

In Chapter 4, we try to enhance the S-T direct excitation of Ru complex by a magnetic field enhanced by a toroidal dipole resonance. Typical optical transition (*e.g.* a S-S transition) occurs by the electric field of light as mentioned. However, the high order term (*i.e.* magnetic dipole, electric quadrupole transition) contributes to the optical excitations when the electric dipole transition is forbidden (*e.g.* spin-forbidden transition). In this chapter, we enhance the S-T direct transition of Ru complex by the magnetic field at toroidal dipole resonance leaking outside structures. We control the wavelength of toroidal dipole resonance from the tail of S-S absorption to the S-T transition energy of Ru complex and conduct photoluminescence excitation measurement of Ru complex on Si metasurfaces. We experimentally demonstrate photoluminescence is strongly enhanced (35-fold) at the S-T transition energy where photoluminescence of Ru complex on the silica substrate (reference) is very small. From calculation results, we summary the magnetic field enhancement at a toroidal dipole resonance contributes to this enhancement. In Chapter 5, we develop a functional metasurface composed of a thin Si nanodisk array and photosensitizing molecules as a photochemical reaction platform. For a model reaction, we examine the performance of this functional metasurface by detecting singlet oxygen ($^1O_2$) generated via Dexter energy transfer from the T_1 state of $RuPc(py)_2$ under the illumination of photons corresponding to the direct $S_0 \rightarrow T_1$ transition energy. We demonstrate enhancing photosensitizer activity under ~400 meV below the S-S transition.

In Chapter 6, we study a hexagonal array of low-aspect-ratio silicon nanodisks formed on a silicon thin film for a photodetection below Si bandgap as one of the applications utilizing a large confined electric field of a toroidal dipole resonance. Numerical simulations reveal that the nanodisk array possesses toroidal dipole modes that tightly confine incoming light in a silicon region below the nanodisks. The field confinement brings about narrow-band absorption when the extinction coefficient (κ) is very small, *e.g.,* $\kappa = 10^{-2} \sim 10^{-3}$. This suggests that defect-related

sub-band gap absorption of silicon can be enhanced by utilizing the modes. Transmittance spectra of fabricated devices reveal that narrow dips assigned to the toroidal dipole resonances appear in the sub-bandgap region. At the resonance wavelengths, the photocurrent is substantially enhanced; the enhancement factor reaches 30-fold at around 1300 nm which is below the band gap of Si. The observed narrow-band photodetection can be used as a current-detection-type refractive index sensor operating in the near infrared range.

Finally, we summarize all results and present future outlook in Chapter 7.

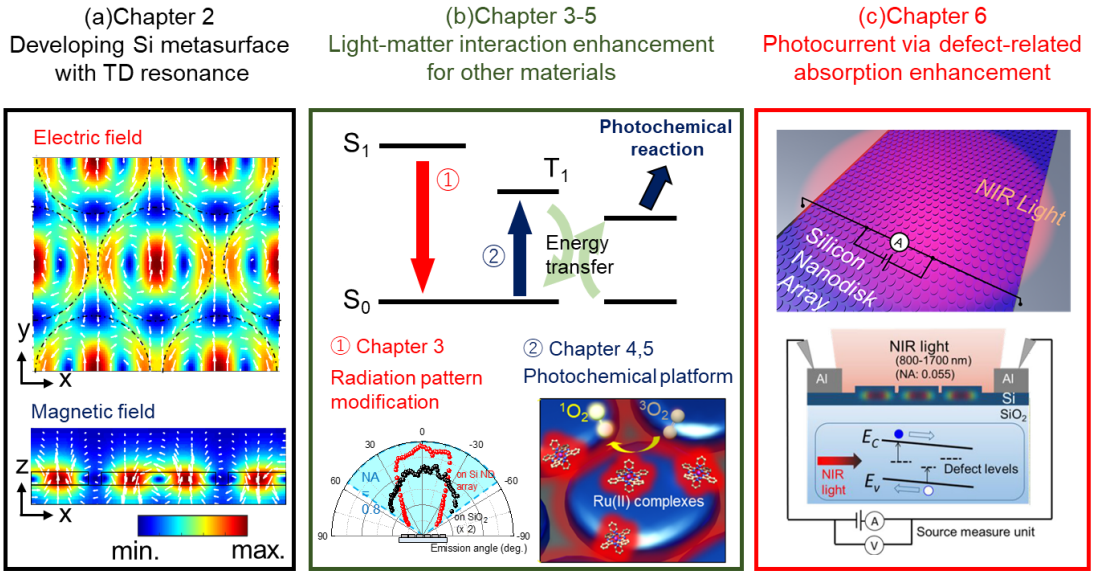

Figure 1-11 *Chapter over view: (a)developing toroidal dipole metasurfaces in Chapter 2, application for (b) light-matter interaction enhancement in Chapter 3 to Chapter 5, and (c)photocurrent enhancement in Chapter 6.*

Chapter 2

Toroidal Dipole Resonance in Si Nanodisk Hexagonal Array

Adapted from Hiroaki Hasebe, et. al., Adv. Optical Mater. 2020,8, 2001148

In this chapter, we show the optical responses of Si metasurfaces that are composed of very thin (height/diameter ~ 1/7) Si nanodisks that have a toroidal dipole mode. We first calculate the optical responses of an isolated thin Si nanodisk. From scattering and multipole decomposition analysis, we reveal that a high aspect ratio Si nanodisk induces a toroidal dipole mode with plane wave excitation and an anapole state emerges by the destructive interference between an electric dipole and a toroidal dipole mode. We then demonstrate that in a hexagonal array, constructive interaction of the TD modes of Si nanodisks near the anapole state results in an emergence of coupled TD modes. The TD response of the Si nanodisk hexagonal array is polarization insensitive due to the highly symmetric arrangement of the nanodisks. The electric field confined in the nanodisk array reaches ~4-fold of that of an isolated nanodisk. At the resonance condition, the coupled TD mode dramatically enhances the absorption compared to that of a flat Si film with the same thickness.

2.1 Numerical Simulations

2.1.1 Single Si Nanodisk

Prior to the analysis of the Si nanodisk array, we first study the optical responses of a single Si nanodisk by finite-difference time domain (FDTD) simulation. For the calculation, the refractive index and the extinction coefficient obtained by spectroscopic ellipsometry of a polycrystalline film were used (**Figure 2-12**). **Figure 2-1**(a) shows the scattering cross section of a Si nanodisk with 450 nm in diameter and 50 nm in height. The illumination light comes from the normal to the top face. Dips appear at 792 nm and 581 nm. We performed multipole

decomposition to analyze the origin of these dips. The moments of the Cartesian electric dipole (***P***), magnetic dipole (***M***), toroidal dipole (***T***), electric quadrupole ($Q_{\alpha\beta}$), and magnetic quadrupole ($M_{\alpha\beta}$) moments were calculated by using the following formula in the long-wavelength approximation, [23]

$$\boldsymbol{P} = \frac{1}{i\omega}\int \boldsymbol{J}(\boldsymbol{r})d^3r\,, \tag{17}$$

$$\boldsymbol{M} = \frac{1}{ic}\int \boldsymbol{r}\times\boldsymbol{J}(\boldsymbol{r})d^3r\,, \tag{18}$$

$$\boldsymbol{T} = \frac{1}{10c}\int \{(\boldsymbol{r}\cdot\boldsymbol{J}(\boldsymbol{r}))\boldsymbol{r} - 2[\boldsymbol{r}\cdot\boldsymbol{r}]\boldsymbol{J}(\boldsymbol{r})\}d^3r\,, \tag{19}$$

$$Q_{\alpha\beta} = \frac{1}{2i\omega}\int \left\{r_\alpha J_\beta(\boldsymbol{r}) + r_\beta J_\alpha(\boldsymbol{r}) - \frac{2}{3}[\boldsymbol{r}\cdot\boldsymbol{J}(\boldsymbol{r})]\delta_{\alpha\beta}\right\} d^3r\,, \tag{20}$$

$$M_{\alpha\beta} = \frac{1}{3c}\int \{[\boldsymbol{r}\times\boldsymbol{J}(\boldsymbol{r})]_{\boldsymbol{\alpha}} r_\beta + [\boldsymbol{r}\times\boldsymbol{J}(\boldsymbol{r})]_\beta r_\alpha\}d^3r\,, \tag{21}$$

where **r** is position vector, $\boldsymbol{r}(\mathrm{x},\mathrm{y},\mathrm{z})$, *c* is the light velocity and ω is the frequency. The indices, α and β indicate the Cartesian axes x, y, and, z. $\boldsymbol{J}(\boldsymbol{r})$ indicates the charge current in the structure and is expressed by

$$\boldsymbol{J}(\boldsymbol{r}) = -i\omega\varepsilon_0(n^2-1)\boldsymbol{E}(\boldsymbol{r}), \tag{22}$$

where $\boldsymbol{E}(\boldsymbol{r})$ is the electric field in the structure, *n* is the refractive index of the structure and ε_0 is the dielectric permittivity of free space. The scattered power of each dipole, I_{ED}, I_{MD}, I_{TD}, is obtained by the following formula,

$$I_{ED} = \frac{2\omega^4}{3c^3}|\boldsymbol{P}|^2 \tag{23}$$

$$I_{MD} = \frac{2\omega^4}{3c^3}|\boldsymbol{M}|^2 \tag{24}$$

$$I_{TD} = \frac{2\omega^6}{3c^5}|\boldsymbol{T}|^2 \tag{25}$$

$$I_{EQ} = \frac{\omega^6}{5c^5}\sum\left|Q_{\alpha\beta}\right|^2 \tag{26}$$

$$I_{MQ} = \frac{\omega^6}{20c^5}\sum\left|M_{\alpha\beta}\right|^2. \tag{27}$$

Figure 2-1 (b) shows the scattering powers from these modes. The same intensity of the ED and TD around 792 nm indicates that the scattering dip is due to an anapole state. The reasons why the scattering cross section does not reach 0 at the anapole state are the contribution of MQ mode and the phase difference between the ED (P_y) and TD (ikT_y) moments (Figure 2-1(c)). Figure 2-1(d, e) shows the electric and magnetic field distributions at 792 nm. The profiles have characteristic features of an anapole state. The maximum electric and magnetic field enhancements inside the nanodisk are 2.5 and 7.3, respectively. The second dip can be also assigned to an anapole state, *i.e.* a high-order anapole state along radial direction [76,137,138] (Figure 2-1(f)). Figure 2-1(g, h) shows the contour plots of scattering cross sections of Si nanodisks with different diameters (height fixed to 50 nm) and height (diameter fixed to 450 nm), respectively. The anapole condition can be tuned in the wide spectral range (515 nm to 810 nm) by changing the Si nanodisk diameter and height.

2.1.2 Si Nanodisk Hexagonal Array

We showed the presence of the TD mode in a Si nanodisk with a large diameter-to-height ratio. To realize further strong TD responses by maximizing the interaction between nanodisks in a two-dimensional surface, we consider a hexagonal array of Si nanodisks. The Si nanodisk array was formed on a SiO_2 substrate (n = 1.46). The diameter (D) and height (h) of a nanodisk are 450 and 50 nm, respectively. The pitch (P) of the array is 500 nm. The nanodisk array is illuminated by a plane wave polarized along y-axis from the normal to the surface. **Figure 2-2**(a) shows the transmittance (T) and reflectance (R) spectra. The sharp reflectance peak (transmittance dip) at 632 nm is a diffraction mode known as Rayleigh anomalies (RA). This diffraction mode can be

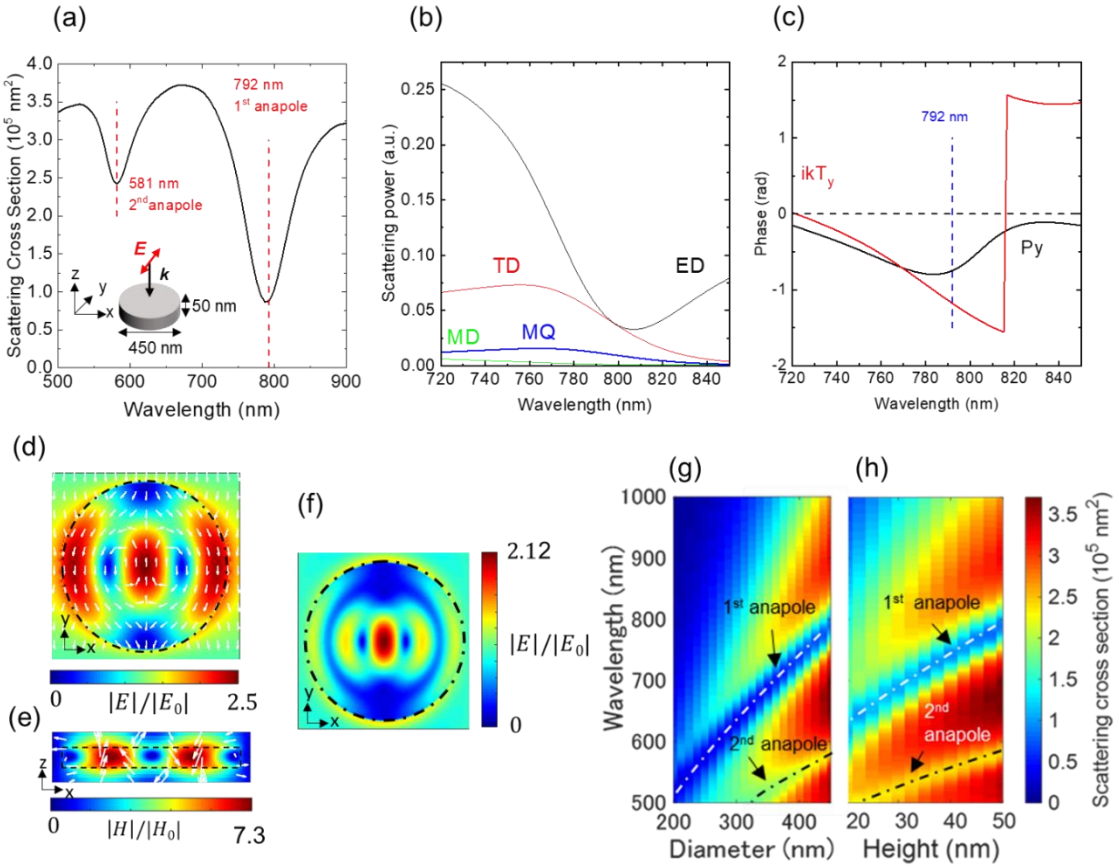

Figure 2-1 *(a-f) Calculation results of a single Si nanodisk with 450 nm in diameter and 50 nm in height, respectively. (a) Scattering cross section. (b) Scattering intensity spectra from each modes induced in the Si nanodisk. (c) Phase spectra of toroidal dipole mode (ikT$_y$, red curve) and electric dipole mode (P$_y$, black curve). (d) Electric (xy plane) and Magnetic field (ax plane) at 792 nm (1st anapole state) and (f) electric field at 581 nm (2nd anapole state). (g,f) Contour maps with (a) different diameters (h = 50 nm) and (b) different heights (D = 450 nm).*

calculated theoretically. In the case of a hexagonal array, the in-plane diffraction mode vector ($\overrightarrow{k_0} = \frac{2\pi n}{\lambda}$, n is a refractive index of the medium) can be described by following equation.

$$\pm\overrightarrow{k_0} = \overrightarrow{k_{i\parallel}} + \vec{G}(p,q)$$

$$= \begin{pmatrix} \frac{2\pi}{\lambda} cos\phi sin\theta \\ \frac{2\pi}{\lambda} sin\phi sin\theta \end{pmatrix} + \frac{2\pi}{\Lambda}\begin{pmatrix} p \\ \frac{-p+2q}{\sqrt{3}} \end{pmatrix}, \qquad (28)$$

where $\overrightarrow{k_{\iota\|}}$ is the wavevector of in-plane component of the incident light, $\vec{G}$ is the reciprocal vector, (p, q) is diffraction order, ϕ is the angle between k vector of incident light and k_x (azimuthal angle), θ is the incident angle, and Λ is the length of period. From Eq. (29), we can obtain

$$\lambda = \sqrt{3} \cdot \Lambda \,(n^2 - sin^2\,\theta)\left(\Omega(\phi) \cdot sin\theta + \sqrt{sin^2\,\theta \cdot (\Omega(\phi))^2 + 4\,(n^2 - sin^2\,\theta)(p^2 + q^2 - pq)}\,\right)^{-1}$$

$$\left(\Omega(\phi) = \sqrt{3}cos\phi \cdot p + (-p + 2q)sin\phi\right) \tag{29}$$

as RA wavelength. When the incident light comes from normal to the surface ($\phi, \theta = 0^o (k_{x,y} = 0)$), RA wavelength is 632 nm at $(p, q) = (\pm 1, 0), (0. \pm 1), (\pm 1, \pm 1)$ and n = 1.46 (silica substrate), which is in good agreement with the calculation result. Around 825 nm in Figure 2-2(a), we can also see a Fano-like asymmetric peak in transmittance and reflectance spectra. Figure 2-2(b) shows the absorptance spectrum obtained by subtracting the reflectance and transmittance spectra from unity (1-*R*-*T*). The absorptance of 50 nm thick Si flat film is also shown as a reference (broken curve). A strong absorption peak appears at 826 nm which is a cross point of T and R. Since the absorptance of a flat Si thin film at the wavelength is very small (2.4×10^{-3}), formation of the nanodisk array enhances the absorptance by a factor of 120, despite the volume reduction of 26.5%. Figure 2-2(c) shows the electric field distribution (*xy*-plane at the middle of the nanodisk height) at 826 nm when the nanodisk array is illuminated by *y* polarized light from normal to the substrate. Although the field distribution in individual nanodisks is similar to that of an isolated nanodisk in the anapole state (Figure 2-1(d)), in the array, the field extends to the gap regions suggesting the near-field coupling between nanodisks. The enhancement factor reaches about 4 times larger than that of an isolated Si nanodisk. The coupling can be verified in the magnetic field distribution in Figure 2-2(d) (*xz*-plane, along the gray dashed line in Figure 2-2(c)). In addition to the intra-nanodisk magnetic loop labeled m_1 (red arrow), inter-nanodisk magnetic loops labeled m_2 (green arrow) are clearly observed, indicating the constructive coupling

of the TD mode between neighboring nanodisks. Interestingly, over 20 fold enhanced magnetic field leaks outside the structure, which is utilize for magnetic-light-matter interaction enhancement. To understand the multipolar contributions to the spectra in Figure 2-2(a) and (b), we calculate the scattered power by ED, MD, TD, EQ, and MQ moments by the multipole decomposition of the induced current density in the nanodisk at the center in Figure 2-2(c). Figure 2-2(e) shows the results. The scattered power spectra are significantly different from those of an isolated nanodisk in Figure 2-1(b). In particular, the TD mode is dominant around 826 nm and is much sharper than that of the isolate nanodisk. Therefore, coupling between the Si nanodisks affects much more to the TD mode than to the ED and MD modes, and boosts the TD mode. To estimate the Q-factor of the Fano-like line shape in the transmittance spectrum, we fitted the spectra with the Fano formula given[139,140] by

$$T(\omega) = T_0 + \frac{A_0\left[q + \frac{2(\omega-\omega_0)}{\tau}\right]^2}{1 + \left[\frac{2(\omega-\omega_0)}{\tau}\right]^2}\ , \tag{30}$$

where ω_0 is the resonant ferequency, τ is the line width, T_0 is the teansmission offset, A_0 is the continuum discrete coupling constant, and q is the asymmetric parameter. The Q factor is then given as ω_0/τ. Figure 2-2(f) shows the result of the fitting of the transmittance spectrum of a Si ND hexagonal array with D = 450 nm, h = 50 nm, and P = 500 nm. The values of ω_0 and τ are 2.28×10^{15} Hz and 1.79×10^{13} Hz, respectively, and the Q-factor is 128.

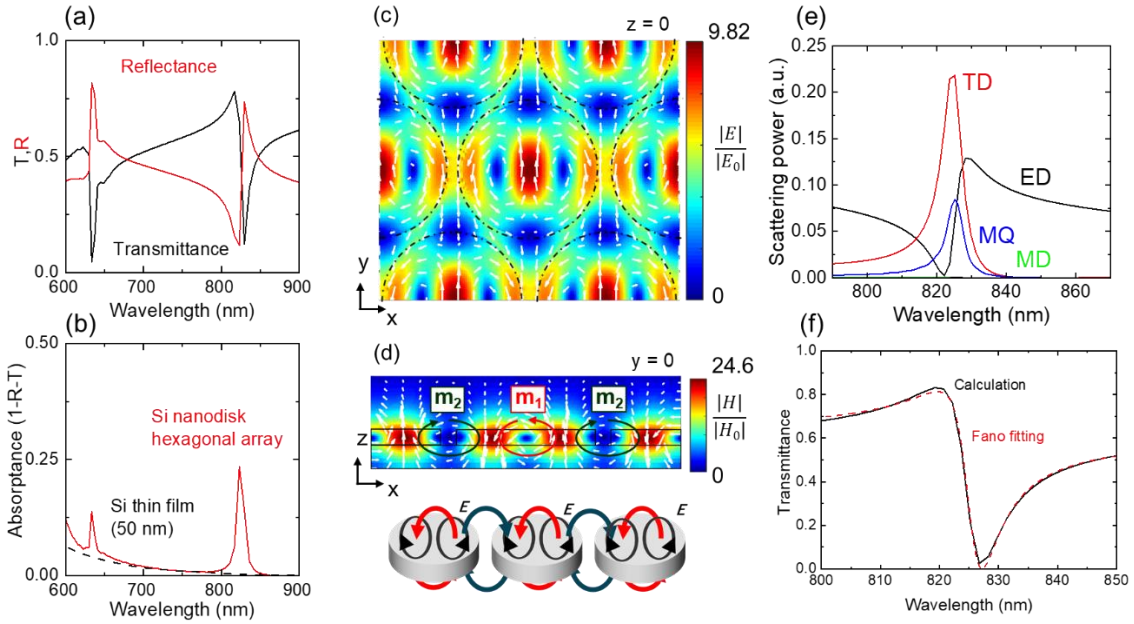

Figure 2-2 *Calculation results of a Si nanodisk array (P = 500 nm, D = 450 nm, h = 50 nm). (a) Transmittance (black curve) and reflectance (red curve) spectra. (b) Absorptance spectra of the nanodisk array (red curve) calculated by 1-R-T. Absorptance of flat Si film (thickness 50 nm) is also shown (black dashed curve). (c) Electric (xy plane) and (d) magnetic (zx plane) field distributions at 825 nm (toroidal dipole resonance). (e) Scattering power spectra from each mode induced in a Si nanodisk around toroidal dipole resonance. (f) Fano fitting spectra (red dashed curve) of toroidal dipole mode.*

One of the advantages of the present symmetric hexagonal array structure compared to array structures composed of more complicated components[141,142] is the insensitiveness of the optical responses to the polarization of incident light. In **Figure 2-3** we show the absorption spectrum and electric and magnetic field distributions when the polarization of incident light is 60° from the x-axis. The absorption spectrum in Figure 2-2(a) is also shown for the comparison. We can see that the absorption spectrum is independent of the polarization direction.

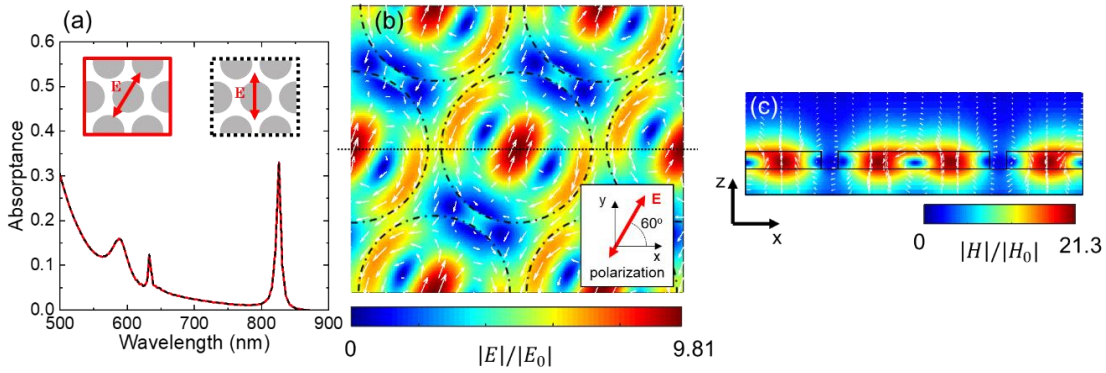

Figure 2-3*(a) Absorption spectra of a Si nanodisk array under illumination from the normal to the surface. The polarization direction is rotated by 30º from red to black. (b) Electric field distribution in the xy plane at 826 nm when the polarization direction of incident light is 60º from the x-axis (see the inset). (c) Magnetic field distribution in the xz-plane along the dotted line in (b).*

It is expected that the coupling strength depends strongly on the distance between nanodisks. The absorptance spectra with different periods are shown in **Figure 2-4**(a). The absorption decreases and becomes broader as the period is longer. In Figure 2-4(b,c,d), scattering power spectra of ED, MD and TD moments calculated for nanodisk arrays with different pitches (500, 550 and 600 nm) and the same nanodisk diameter and height (450 nm, 50 nm, respectively) are shown. At 600 nm, the intensity of the TD mode is only about 20% of that of the ED mode and is very broad. The TD mode becomes intense and much sharper at 550 nm, although the peak intensity is still smaller than that of the ED mode. At 500 nm, the relation is reversed and the TD mode dominates the spectrum. These results show that toroidal dipole mode dominantly contributes to the absorptance of the nanodisk array and the distance between nanodisks (period),which relates to the coupled strength of toroidal dipole modes, is an important parameter to obtain a sharp absorptance.

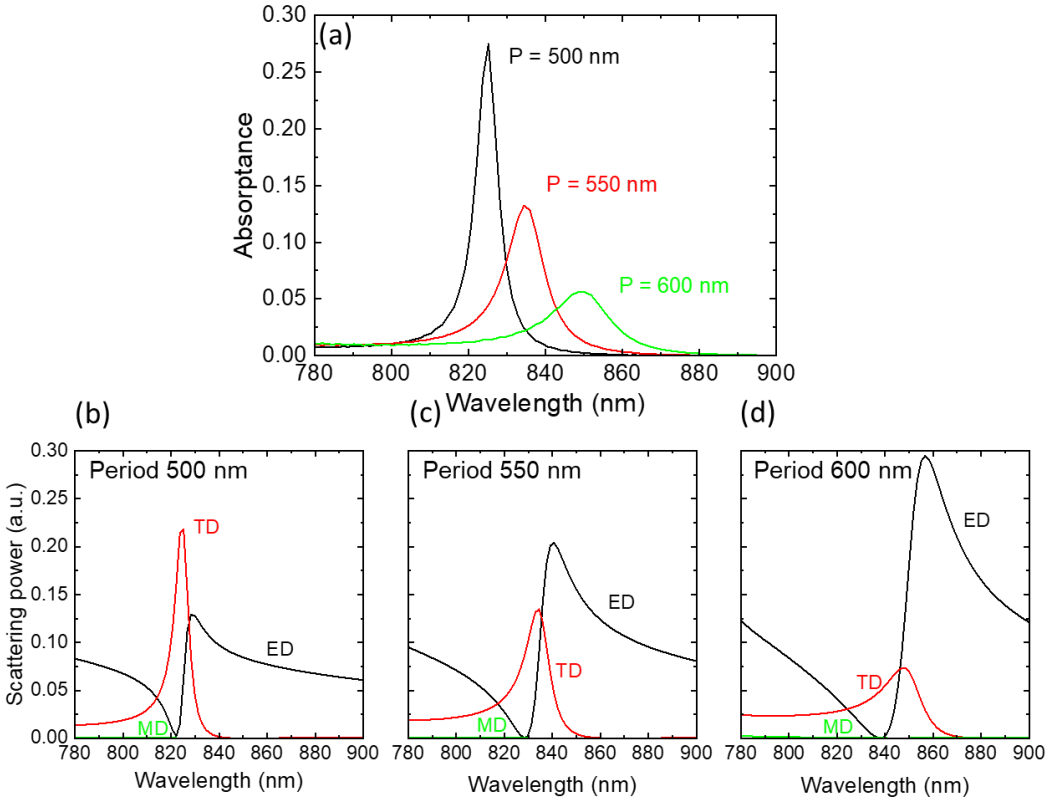

Figure 2-4 *(a) absorptance spectra with different periods (D = 450 nm, h = 50 nm), (b,c,d) the results of multipole decomposition of (b)P = 500 nm, (c) P = 550 nm, and (d) P = 600 nm,*

Figure 2-5 shows the transmittance, reflectance, and absorptance contour maps with different diameters (h = 50 nm) and different heights (D = 450 nm). The periods are fixed to 500 nm. There are two resonances, RA and TD resonance. RA appears around 632 nm and this wavelength does not depend on the nanodisk heights and diameters because it is determined by the array's period and the incident light angle (eq.(30)). On the other hand, TD resonance strongly depends on the height and diameter. This is because toroidal dipole mode is induced in individual nanodisks and its trend is same as a single nanodisk shown in Figure 2-1(g,h). The difference between changing diameter and height is that the TD resonance becomes broader as the diameter decreases, whereas the width of the resonance is kept sharp as the height is reduced. The reason

is the coupling strength of TD modes becomes small because the distance between nanosdisks is larger in case of changing diameter, which is described in Figure 2-4, and the distance does not change when the nanodisk height is changed.

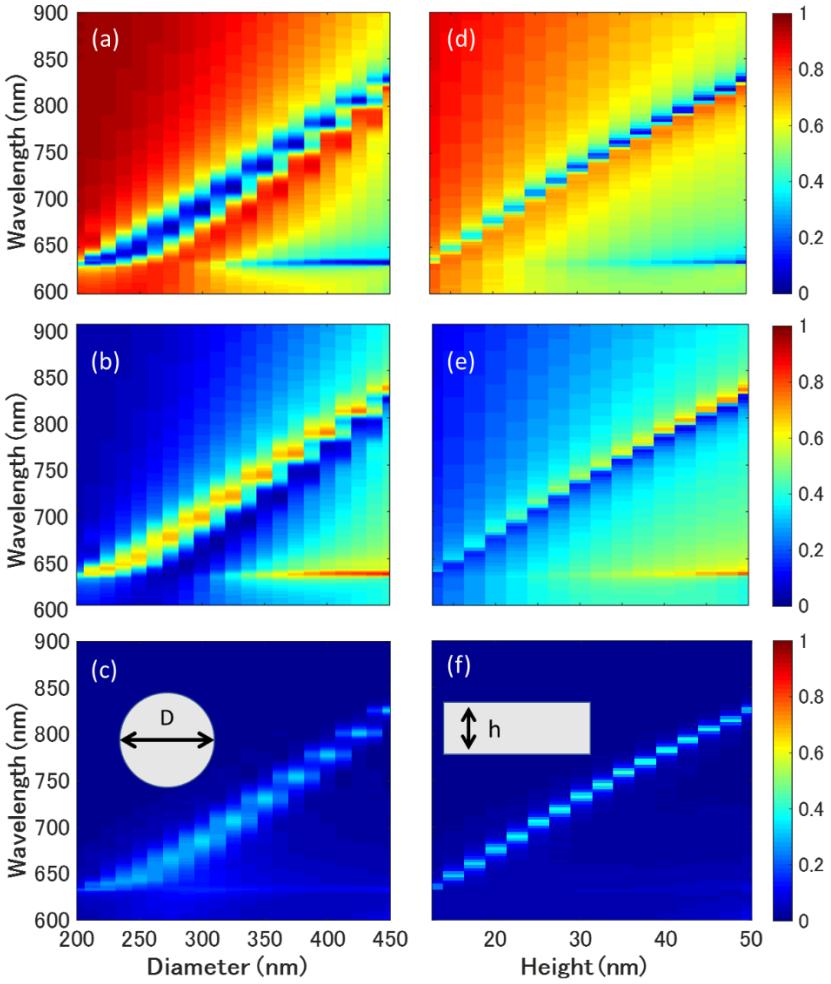

Figure 2-5 *Contour maps of (a,d) transmittance, (b) reflectance, and (c) absorptance with (a,b,c) different diameters (P = 500 nm, h = 50 nm) and (d,e,f) different heights (P = 500 nm, D = 450 nm).*

Figure 2-6 shows the incident angle dependence of transmittance spectra with TM and TE polarized light (P = 500 nm, D = 450 nm, h = 50 nm). We can see toroidal dipole resonances at 826 nm in both cases, but their dependencies are different. The toroidal dipole mode of TM

polarized light interacts with (-1,0) or (-1,-1) order RA and it shifts to a longer wavelength as the incident angle becomes steep, whereas that of TE polarized light interacts with (0,±1) order RA and it shifts to a shorter wavelength. This is because of the coupling direction of toroidal dipole mode. In the case of TM polarization, the toroidal dipole modes induced individual nanodisks couple along $\boldsymbol{a_2}$ direction (shown in bottom right sketch) as shown in Figure 2-3(b). This direction is the same as $n\boldsymbol{a_1} + r\boldsymbol{a_2}$ and $r(-\boldsymbol{a_1} + \boldsymbol{a_2}) - n\boldsymbol{a_1}$ (shown by the red and blue dash lines in the bottom right in Figure 2-6(a)), which is corresponding to the real planes of (-1,0) and (-1,-1) directions in reciprocal space. In the case of TE polarization, this mode couples along $\boldsymbol{a_1}$ direction as shown in Figure 2-2(c), and this direction is the same as $r\boldsymbol{a_1} \pm n\boldsymbol{a_2}$ (shown by the green dash lines in the bottom right in Figure 2-6(b)), which corresponds to the real planes of (-1,0) and (-1,-1) directions in reciprocal space. Although toroidal dipole mode interacts with RA, the dependence is less steep than RA modes because toroidal dipole mode is an eigenmode of a nanodisk.

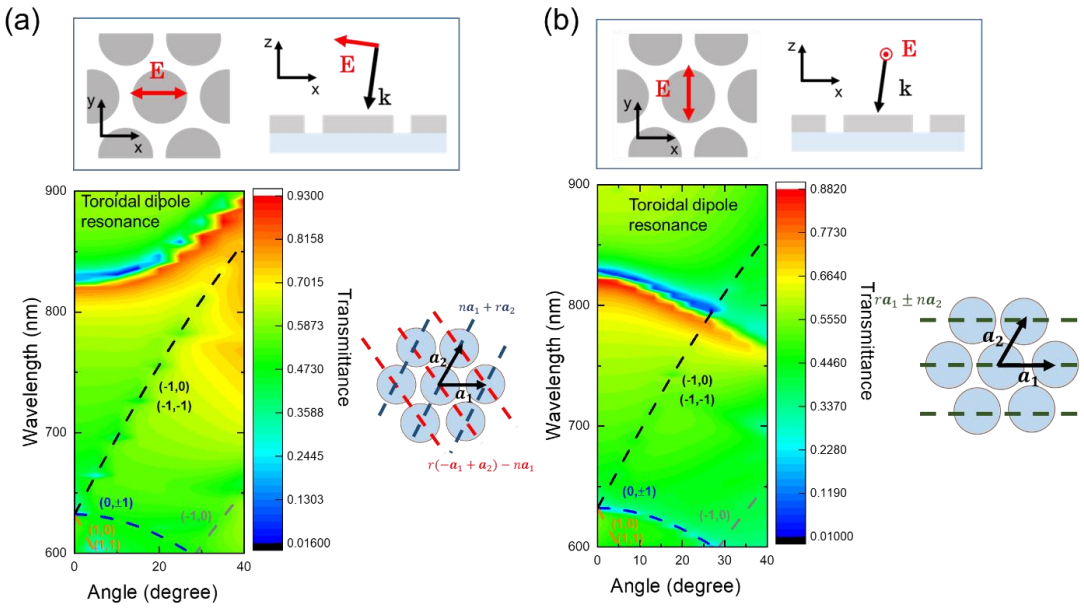

Figure 2-6 *Incident angle dependence of transmittance spectra with (a)TM and (b)TE polarized light (P = 500 nm, D = 450 nm, h = 50 nm). Dash curves indicate the RA wavelength with different diffractive orders.*

2.2 Fabrication of Si Nanodisk Hexagonal Array

We employ colloidal lithography to fabricate hexagonal arrays of Si nanodisk arrays over a large area. The procedure is schematically shown in **Figure 2-7**. A hexagonal array of polystyrene beads (PSBs) was used as an etching mask to produce a Si nanodisk array. The lower right image in Figure 2-7 is a picture of the final structure. A Si nanodisk array is produced in 1.2×2.7 cm^2 area. In this chapter, we summarize the detailed fabrication conditions and experimentally demonstrate a toroidal dipole resonance with transmittance, reflectance, and absorptance spectra.

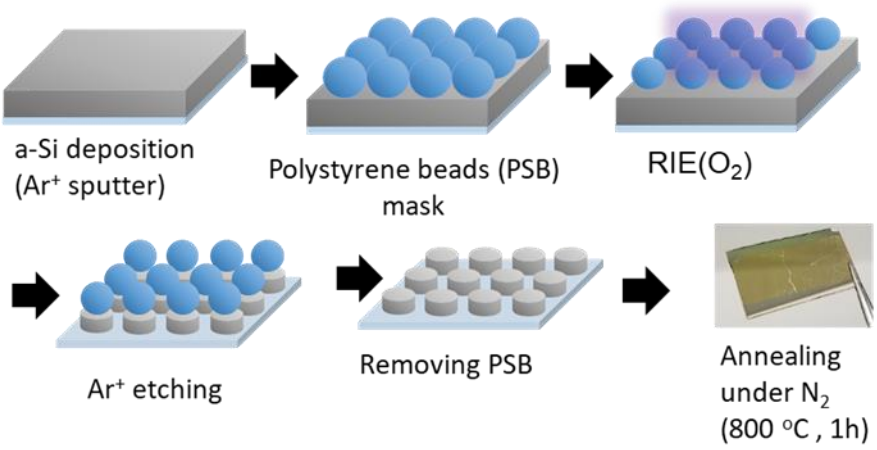

Figure 2-7 *Schematic image of a Si nanodisk fabrication.*

- *Amorphous Si deposition on a substrate.*

Amorphous Si films were deposited on a SiO_2 substrate with 750 μm in thickness by an rf-sputtering apparatus (SPF-210H, ANELVA). The substrate is cleaned with acetone and isopropanol with a sonicator before Si deposition. The Ar flow rate, the total pressure, and the sputtering power were 20 sccm, 20 mTorr, and 100 W, respectively. The Si film thicknesses (nanodisk heights) are controlled by deposition time. First, we estimated the Si film deposition rate from the ellipsometry (HORIBA; Auto SE) results of Si films on glass slides with different deposition times. **Figure 2-8**(a) shows the model for the ellipsometry. We used *a-Si_jel_tl.dsp* which is Tauc-Lorentz distribution equation for layer 1 and measured glass slide data for the

substrate. Figure 2-8(b) shows the Si nanodisk film thickness as a function of deposition time. We obtain 30.2 nm/min as Si deposition rate by linear fitting of this result. Using this rate, we fabricate Si nanodisk arrays with 20, 30, 40, and 50 nm in height (Figure 2-8(c-f)).

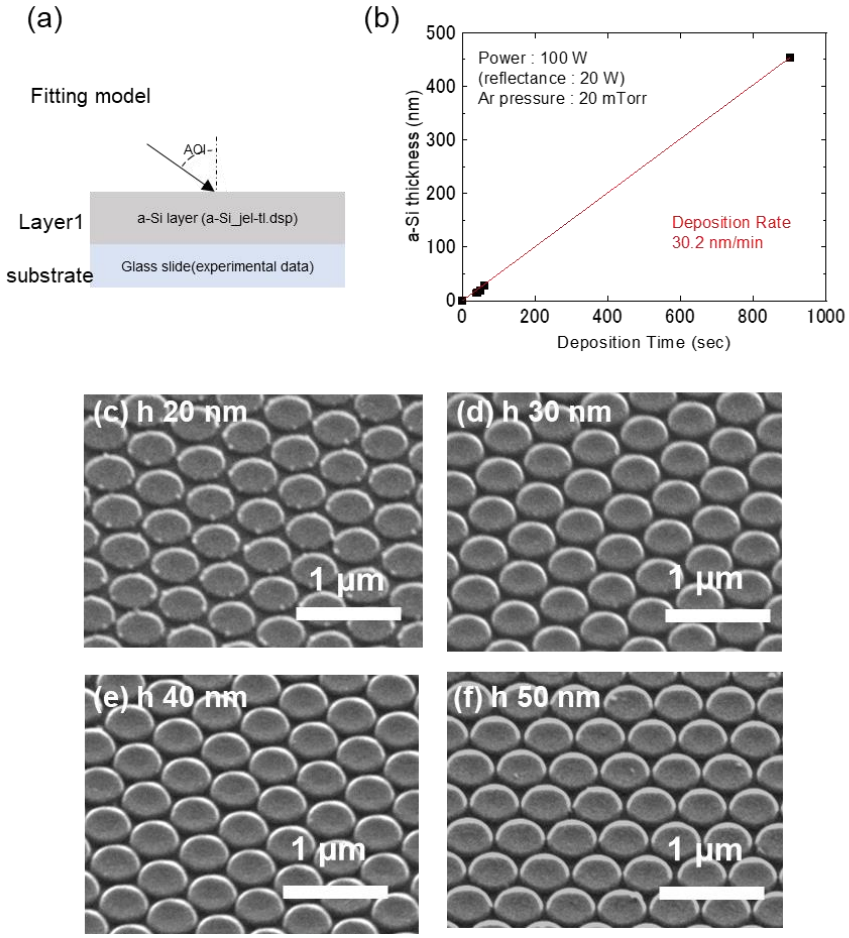

Figure 2-8 *(a) Ellipsometry model for thickness calculations. (b) The deposition rate of Si as a function of deposition time. Inset graph shows the data around 50 s. (c-f) SEM images of Si nanodisk arrays with (c)20, (d)30, (e)40, and (f)50 nm in height.*

- *Polystyrene self-assembled mask*

1. Spinning down 400 μl of polystyrene beads with 500 nm in diameter suspension （Polybead®Polystyrene） with 3000 rpm for 30 min (H-11NB; KOKUSAN).

2. Removing 300 µl of the supernatant and adding 100 µl of ethanol.

3. Dropping the polystyrene beads suspension at the air/water interface slowly by an opposite (curved) side of a clock glass which is hydrophilized by immersed in 5 M sodium hydroxide aqueous solution for 30 min at 50 °C.

4. Dropping 0.1% sodium dodecyl sulfate aq. at water surface around floating polystyrene to prevent the mask collapsing.

5. Leaving it for 4h to sink some aggregations. Then, we can obtain a self-assembled 2D crystal mask at the air/water interface (**Figure 2-9**(a))

6. Transferring the polystyrene mask on a substrate hydrophilized with UV-O_3 (UV-1; SAMCO) for 5 min at RT.(Figure 2-9(b))

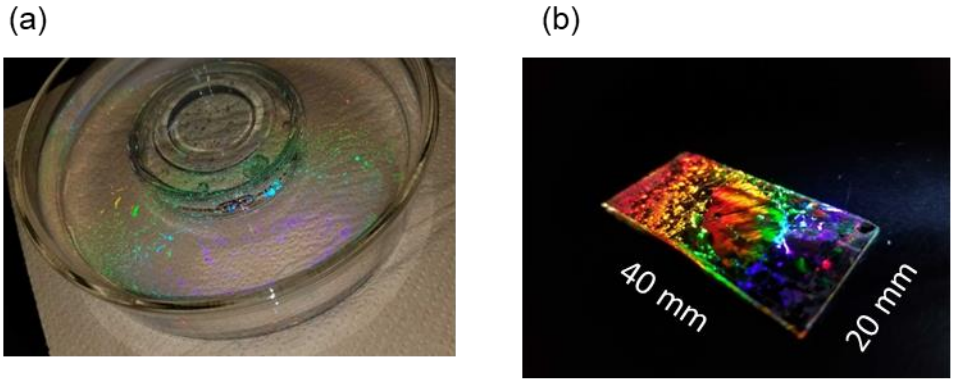

Figure 2-9 *Pictures of (a) self-assembled PSB (Diameter: 500 nm) 2D crystal mask at the air/water interface and (b) after transferring it on a substrate.*

- *Shrinking polystyrene diameter (Controlling nanodisk diameter)*

The diameter of PSBs was reduced by oxygen plasma RIE (ANELVA: L-201D) to control the mask size. The O_2 flow rate, the total pressure, and the power were 3.2~3.8 sccm, 10 Pa, and 50 W, respectively. The diameter of a nanodisk was controlled with etching time. We etched polystyrene masks for 10, 17, 24, and 30s to obtain different diameter nanodisk arrays. **Figure 2-10**(a-d) shows the SEM images of Si nanodisk arrays with different RIE times and (e) shows the nanodisk diameter as a function of etching times estimated from SEM images. The

relation between polystyrene (nanodisk) diameter and etching time can be described by *polynomial equation:* $y(nm) = 0.25\,t - 0.23\,t^2 + 497$.

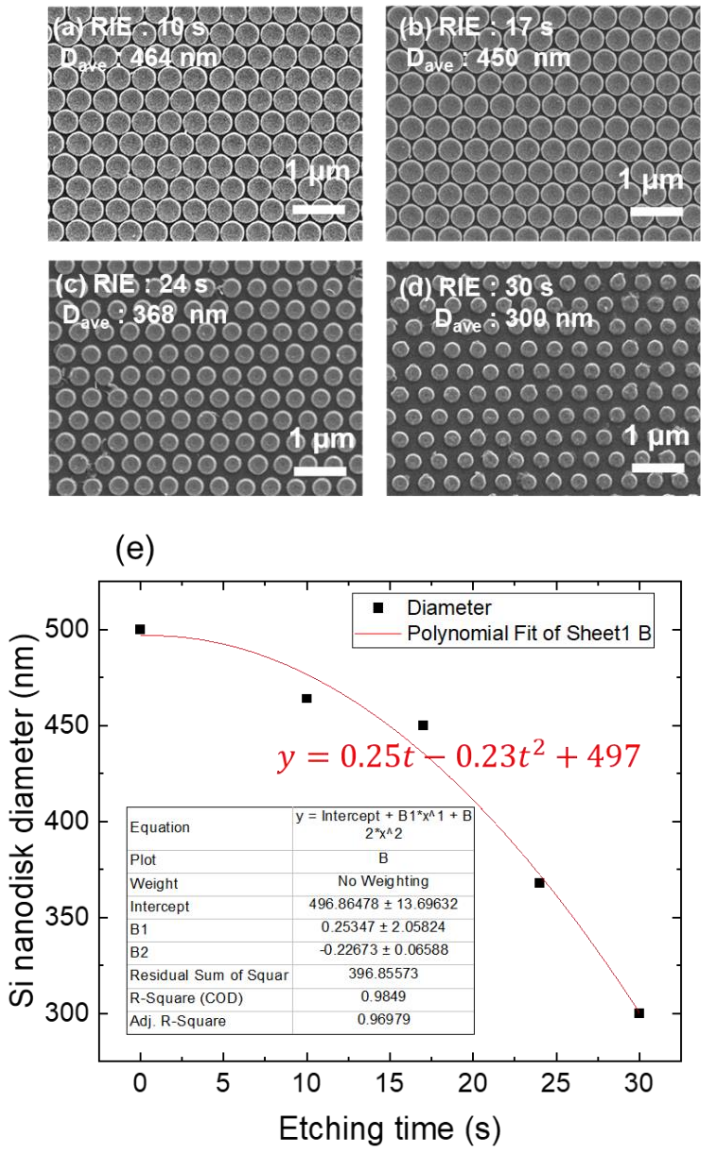

Figure 2-10 *(a-d) SEM images of Si nanodisk arrays with different RIE times (e)The nanodisk diameter as a function of RIE time.*

- *Etching Si film (forming nanodisk array)*

The PSB mask pattern was transferred to a Si film by Ar^+ etching (ANELVA : SPF-210H). The Ar flow rate, the total pressure, and the sputtering power were 20 sccm, 20 mTorr, and 100 W, respectively. **Figure 2-11** shows the nanodisk height with different Ar^+ etching times

measured by AFM. From this result, the etching rate is estimated as 18.9 nm/min. We changed the etching time corresponding to the Si film thickness. After this step, the polystyrene masks are resolved by N,N-dimethylformamide (FUJIFILM Wako) with a sonicator until polystyrene masks are totally dissolved.

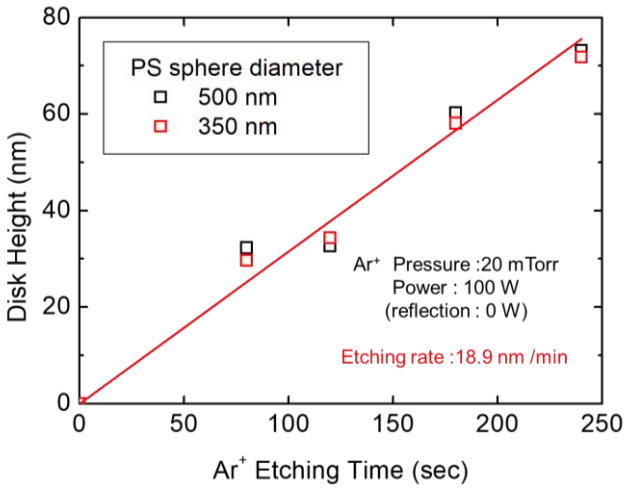

Figure 2-11 *Etching rate of Si*

- *Crystalizing Si*

After forming Si nanodisk arrays, they were annealed at 800 ºC in an N_2 atmosphere (flow 2.0 L/min) for an hour for the crystallization (SYK-460-MA; SANYO RIKAGAKUKIKAI SEISA KUSHO). To estimate the refractive index and extinction coefficient, we performed ellipsometry. **Figure 2-12**(a) shows the models of amorphous/poly (before/after annealing) crystalline Si. The amorphous Si model is almost the same as Figure 2-8(a) but we introduced an oxide layer (*SiO2 HJY.ref*) on the top. To construct polycrystalline Si layer, we put amorphous and single crystalline Si (*c-Si_Jy.clc)* mixed layer. We used the distribution equation of amorphous Si of mixing obtained by the left model. Figure 2-12(b,c) the refractive index and extinction coefficient of amorphous and polycrystalline Si. The refractive index does not change greatly before and after annealing, whereas the extinction coefficient is reduced after annealing because the defect decreases due to crystalizing. The crystallinity of this poly Si is about 65%.

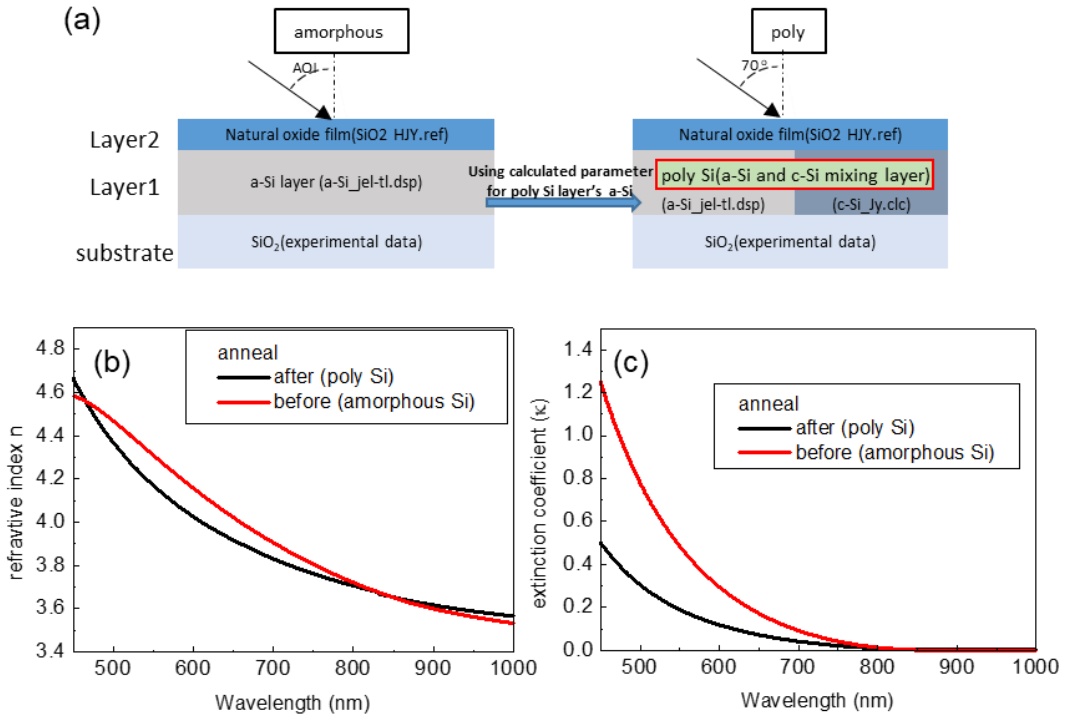

Figure 2-12 *(a) Ellipsometry models for optical constants of (left) amorphous Si (a-Si) and (right) poly Si. (b) Refractive index and (c) extinction coefficients of a-Si (red curve) and poly Si (black).*

2.3 Transmittance, Reflectance, and Absorptance Spectra

We first measured the diffuse transmittance (T) and the diffuse reflectance (R) spectra of the metasurface shown in Figure 2-8 and Figure 2-10 by using an integrating sphere (Figure **2-13**(a,b)). The size of incident light is about 6 mm × 10 mm. Although there are 8 degrees as the incident light angle for a diffuse reflectance measurement, the toroidal dipole resonance wavelength is almost the same as the normal incident as shown in Figure 2-6. Figure 2-13(c,e) shows the transmittance and reflectance spectra of hexagonal arrays of Si nanodisks with a height of 50 nm. The diameter of nanodisks is changed from 464 to 300 nm. We can see Fano shape resonances appear and shift to shorter wavelength as the diameter and the height decreases, respectively. We calculate absorption spectra (A) from the A=1– T– R relation and these spectra are shown in Figure 2-13(g). We can see absorptance peaks caused by toroidal dipole resonance

that shifts from 840 to 670 nm with decreasing diameter. Figure 2-13(i) shows the corresponding calculated absorptance spectra. Although the peak is broadened in the measured absorptance spectra, we can see the fairly good agreement of the peak wavelength between the measured and calculated spectra in the whole dimeter range. The good agreement indicates that the observed absorption peak is due to the coupled toroidal dipole modes discussed in Figure 2-2. The broadening of the peak in the measured spectra probably arises from disorders in nanodisk arrays because we measured the spectra of a wide area (~0.6 cm^2). In Figure 2-13(i), the absorption spectrum of 50 nm thick Si film is also shown (broken curve). Compared to that, the absorption of Si nanodisk arrays is largely enhanced at the resonance wavelengths. For example, in the Si nanodisk array with D = 464 nm and h = 50 nm, the absorptance is about 0.1 at 858 nm, which is 33-fold larger than that of a flat Si thin film with the same thickness. It should be stressed here that the observed enhancement factors are not those from a specific hot spot, but the averaged values in the 0.6 cm^2 detection area. Figure 2-13(d, f, h, j) show the measured transmittance, reflectance, absorptance, and calculated absorptance spectra, respectively, for hexagonal arrays of Si nanodisks with a diameter of 450 nm. The height of nanodisks is changed from 50 to 20 nm. The TD resonance wavelength is also controlled by the nanodisk height, and we can see good agreement of the resonance wavelengths between measured and calculated spectra.

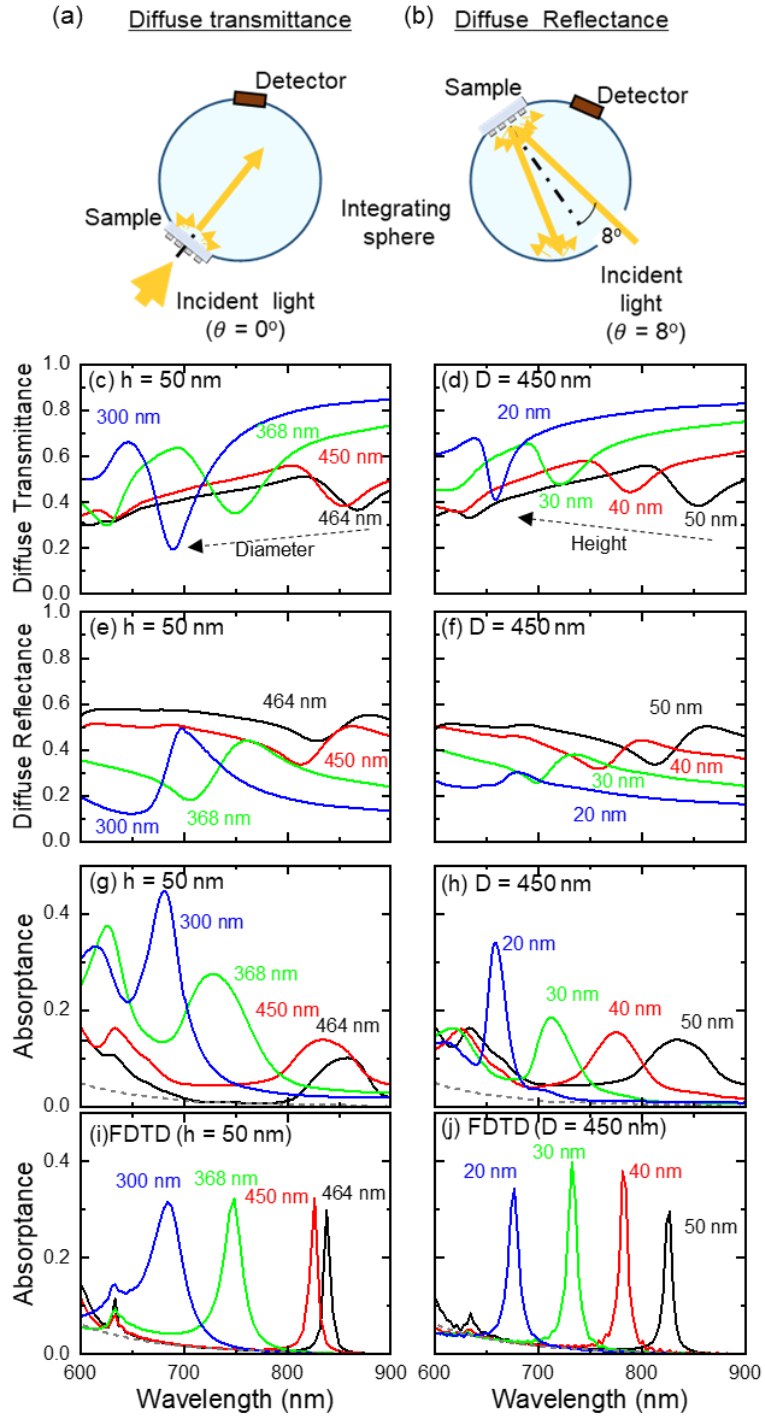

Figure 2-13 *(a,b)Measurement set up of the diffuse transmittance and the diffuse reflectance spectra. Measured (c,d) diffused transmittance, (e,f) diffused reflectance, and (g.h) absorptance spectra calculated from (c,e) and (d,f) with different diameters (c,d,f) and different heights (c,e,g), respectively. (h,i) Calculated absorptance spectra with (h) different diameters and (i) different heights. Broken gray curves in (f-i) is absorptance spectra of flat Si film.*

2.4 Conclusion

We demonstrated by numerical simulations that hexagonal arrays of Si nanodisks can support intra- and inter-nanodisk TD modes when the nanodisks are in close proximity. The key concept to realize the strong TD resonances in a nanodisk array is the constructive coupling of TD modes in a nanodisk near the anapole state condition. This coupling TD resonance can achieve strong electric field confinement and over 20% absorption at the resonance wavelength even though the total Si film thickness is under 50 nm, which leads to miniaturizing a photodetection device. Additionally, the enhanced magnetic field by coupled TD resonance leaks outside the structure, which can be utilized for magnetic-light-matter interaction enhancement. The resonance wavelength can be easily tuned by the nanodisk heights and diameters. Additionally, we fabricated Si metasurfaces that have a toroidal dipole resonance with a colloidal lithography method and measured their optical properties. Tuning both of the heights and diameters of nanodisks by changing the time of Si film deposition and polystyrene RIE, we controlled the toroidal dipole resonance wavelength from 850 nm to 650 nm. Although the resonances measured experimentally are broader than calculations mainly due to inevitable lattice defect, we achieved 33-fold absorption at near infrared range compared to the flat Si film with the same thickness. This indicates the fabricated metasurfaces supported toroidal dipole resonances.

PART I: Light-Matter Interaction Enhancement by Toroidal Dipole Resonance

Chapter 3

Purcell Enhancement and Emission Directional Control

In this chapter, we study the coupling of dipole emitters with the toroidal dipole resonance of a Si metasurface. We form a Si quantum dot monolayer that has broad photoluminescence (PL) on a Si metasurface and measure its PL spectrum. We demonstrate the PL spectrum on the Si metasurface is enhanced at a toroidal dipole resonance wavelength compared to that on a silica substrate. Then, we conduct lifetime and angle resolved photoluminescence measurements to evaluate Purcell effect and a collection efficiency enhancement. We reveal that the PL enhancement almost stems from the collection efficiency enhancement, which is in good agreement with the calculation results.

3.1 Experimental Methods

- Sample fabrication

A monolayer of Si QDs was placed on a Si nanodisk array by drop-coating a colloidal solution of Si QDs(3.5 nm in diameter). Formation of a monolayer was confirmed by spectroscopic ellipsometry[143]. The Si QDs have a very broad emission band[144], which enables us to monitor the property of a Si nanodisk array in a wide wavelength range. **Figure 3-1**(a) shows the SEM image of the nanodisk array coated by Si QDs. There is no agglomeration of Si QDs, which indicates the uniform Si QD layer is formed on Si nanodisk array. Figure 3-1(b) and (c) show the measured and calculated transmittance spectra before and after the QD monolayer

deposition. In the simulation, a 3.5 nm layer with the refractive index of 1.7 is placed on a Si nanodisk array. In both measured and calculated spectra, deposition of a Si QDs monolayer results in slight red-shift (~4 nm) of the resonance wavelengths, confirming the successful formation of the structure shown in Figure 3-1(a).

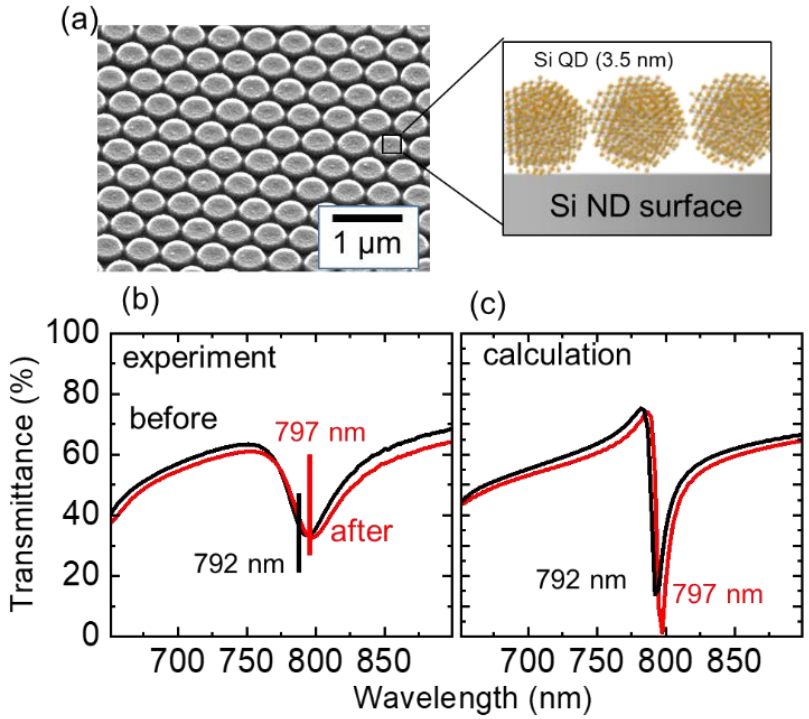

Figure 3-1 *(a) SEM and schematic image of a Si nanodisk array (P = 500 nm, D = 450 nm, h = 42 nm) with Si QDs layer. (b)Measured and (c) calculated transmittance spectra of the Si nanodisk array*

- Photoluminescence and time resolved PL spectra

The simple measurement setup is shown in **Figure 3-2**. The PL was excited from the top surface with 50° and the emission was detected from the bottom surface through the substrate. The N.A. of the collection optics was 0.167. The excitation wavelength was 405 nm(COHERENT : CUBE). The photoluminescence signals are detected by a single spectrometer (Acton :Spectrapro 300i) equipped with a liquid-N_2-cooled charge coupled device (CCD) (Roper

Scientific). In time-resolved PL spectra measurement, we use 2 kHz pulse excitation light and detect PL spectra by ICCD(Roper Scientific：PI-Max1024HB) with 1 μs time resolution.

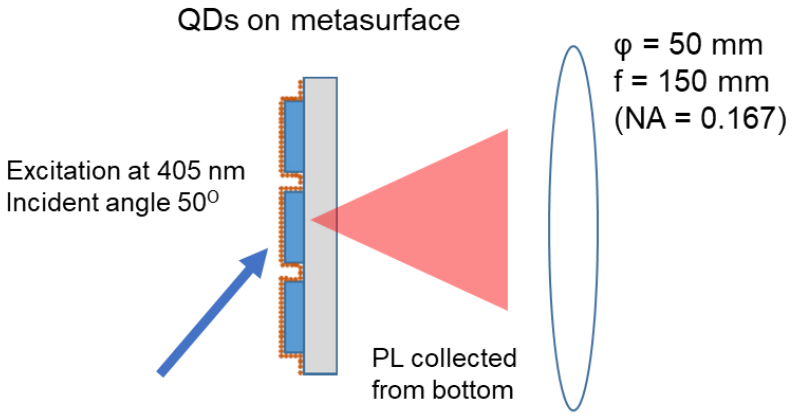

Figure 3-2 *Optical measurement setup for PL and lifetime measurements.*

- Angle-resolved photoluminescence spectroscopy

The radiation pattern was measured by Fourier space spectroscopy using a custom-built inverted optical microscope. The measurement setup is shown in **Figure 3-3**. A Si nanodisk array with a Si QD monolayer on the surface was placed facedown onto the stage and was excited by 405 nm light from a laser diode *via* an air objective lens (×50, NA = 0.8). The laser spot was expanded to ~50 μm in diameter at the focal plane of the objective to excite Si QDs uniformly. The PL emitted from the sample was collected by the same objective. The back focal plane (BFP) of the objective, which corresponds to the Fourier space (k-space), was relayed and imaged onto an entrance slit of a monochromator (iHR320, Horiba Jobin Yvon). From the full back-aperture image viewed as in-plane wavevectors (k_x/k_0, k_y/k_0), the line image at $k_x/k_0 = 0$ was selected using the entrance slit of the monochromator (100 μm) like a bottom image[145]. Note that k_x/k_0 and k_y/k_0 are identical in the present Si nanodisk arrays. The selected line image was spectrally resolved by a monochromator and detected by a liquid-N_2 cooled CCD (Symphony, Horiba Jobin Yvon) to obtain the spectral image in the $-0.8 < k_y/k_0 < 0.8$ range, i.e., the polar angle range from -53° to 53°. However, the obtained spectral image is 2 variable functions of wavelength (λ) and $sin\theta$

($f(\lambda, sin\theta)$). To obtain the function of wavelength and angle (θ), we have to correct the obtained spectral image by the below equation.

$$f(\lambda, sin\theta)dsin\theta = f(\lambda, \theta)d\theta \quad (31)$$

$$\therefore f(\lambda, \theta) = f(\lambda, sin\theta)cos\theta \quad (32)$$

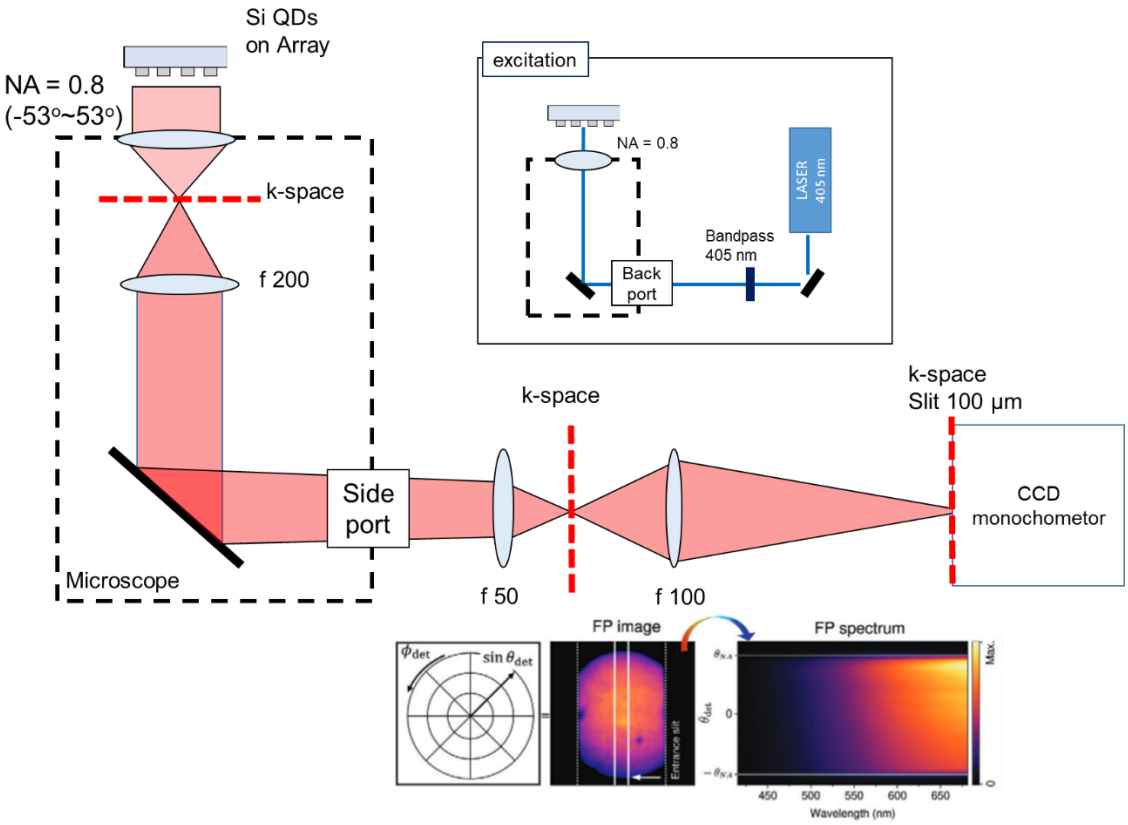

Figure 3-3 *Optical measurement setup for angle resolved PL measurement. The bottom spectral image is referred from ref*[145].

3.2 Results and Discussion

First, we calculate radiative and non-radiative decay rate and collection efficiency enhancements of an electric dipole emitter placed on 4 nm above the metasurface. **Figure 3-4**(a) shows the radiative rate enhancement ($\frac{\gamma_r^{meta}}{\gamma_r^{SiO_2}}$). The radiative decay rate is about 2.5-fold enhanced at toroidal dipole resonance (at 790 nm) due to Purcell effect. However, the nonradiative decay

rate enhancement ($\frac{\gamma_{nr}^{meta}}{\gamma_r^{SiO_2}}$) (Figure 3-4(b)) increases monotonously below 850 nm due to the increase of the extinction coefficient of Si and is relatively larger (7.5 at 790 nm). Figure 3-4(c) shows the collection efficiency enhancement ($\frac{\eta_{ex}^{meta}}{\eta_{ex}^{SiO_2}}$) with 0.168 N.A.. The collection efficiency enhancement reaches 25-fold at 790 nm, which is the largest among three enhancement factors. The emission patterns of an *x*-oriented dipole placed on SiO_2 and on a Si nanodisk array in the *xz* and *yz*-planes are also shown in Figure 3-4(c). The radiation patterns are strongly modified on the Si nanodisk array; the dipole exhibits an out-of-plane directional emission.

To discuss the photoluminescence modified on the metasurface, we calculated PL enhancement ($I_{PL}^{meta}/I_{PL}^{SiO_2}$) from these calculation results. The enhancement is obtained by[146]

$$\frac{I_{PL}^{meta}}{I_{PL}^{SiO_2}} = \frac{\gamma_{ex}^{meta}}{\gamma_{ex}^{SiO_2}} \cdot \frac{Q^{meta}}{Q^{SiO_2}} \cdot \frac{\eta^{meta}}{\eta^{SiO_2}}, \tag{33}$$

where γ_{ex} is excitation rate, Q is a quantum efficiency of Si QDs, and η is collection efficiency. The superscripts "meta" and "SiO_2" indicate QDs on a Si nanodisk array and on SiO_2, respectively. From Fermi's Golden role, the excitation rate enhancement is obtained by

$$\frac{\gamma_{ex}^{meta}}{\gamma_{ex}^{SiO_2}} = \frac{|\boldsymbol{E}|^2}{|\boldsymbol{E_0}|^2} \tag{34}$$

which is the electric field intensity enhancement ($|E/E_0|^2$ at 405 nm) at the dipole position. The calculated value is 0.18, meaning the decrease of the excitation rate on the Si nanodisk array due to the lossy nature of Si in the blue region. Then, the intensity ratio is expressed as

$$\frac{I_{PL}^{meta}}{I_{PL}^{SiO_2}} = \frac{\gamma_{ex}^{meta}}{\gamma_{ex}^{SiO_2}} \frac{Q^{meta}}{Q^{SiO_2}} \frac{\eta^{meta}}{\eta^{SiO_2}} = \frac{|\boldsymbol{E}|^2}{|\boldsymbol{E_0}|^2} \frac{\frac{\gamma_r^{meta}}{\gamma_r^{SiO_2}}}{(\gamma_r^{meta} + \gamma_{nr}^{meta})/\gamma_r^{SiO_2} + (1 - Q^{SiO_2})/Q^{SiO_2}} \frac{\eta^{meta}}{\eta^{SiO_2}}, \tag{35}$$

where γ_r and γ_{nr} are radiative and nonradiative decay rates, respectively. The quantum efficiency of Si QDs (Q^{SiO_2}) is 0.1[147]. Figure 3-4(d) shows the PL intensity ratio obtained by Eq.(36) using the data of Figure 3-4(a-c). Although the ratio reaches 6 at toroidal dipole resonance (790 nm),

the spectral shape is almost same as the collection efficiency enhancement spectrum. This is due to the fact that the excited TD moments are oriented parallel to the *xy*-plane, and the out-of-plane (*i.e., z*-direction) radiation becomes dominant.

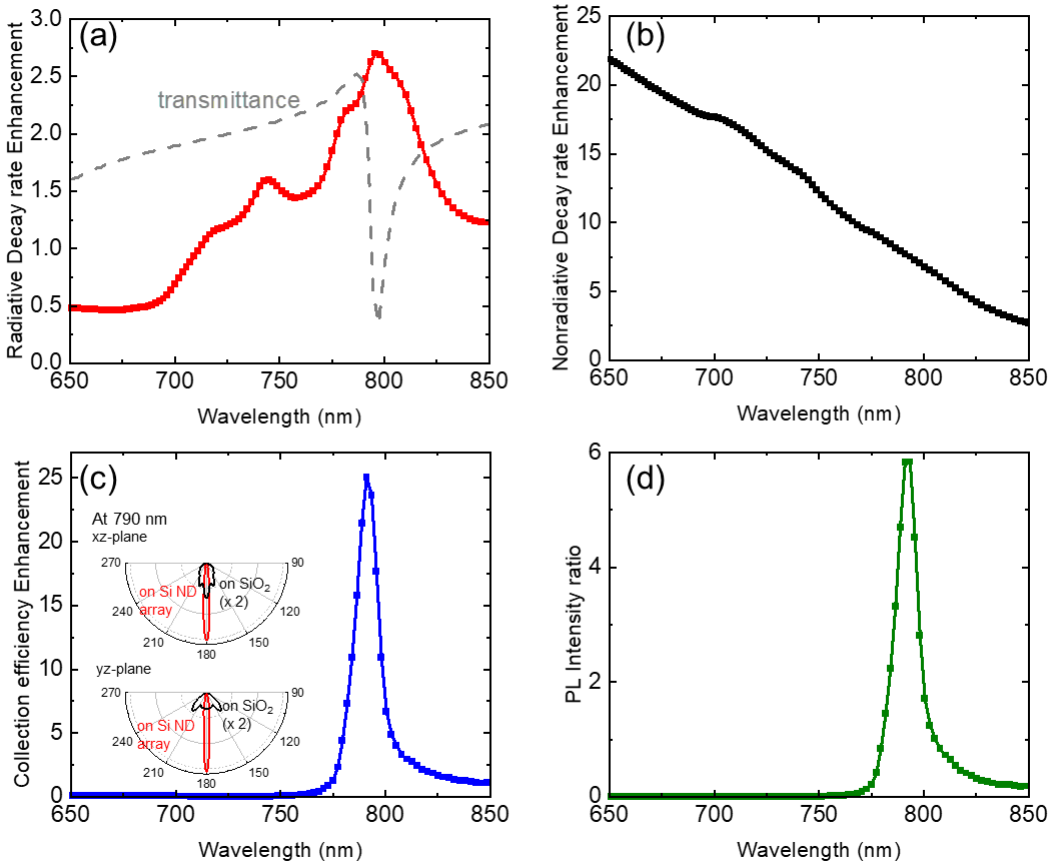

Figure 3-4 *Calculated (a) radiative decay enhancement (red) and transmittance spectrum (gray dashed curve), (b) nonradiative decay rate enhancement, (c) collection efficient enhancement (the radiation patterns at 790 nm are also shown), and (d) PL intensity ration.*

Figure 3-5(a) compares the photoluminescence (PL) spectra of a QD monolayer on a Si nanodisk array (I_{PL}^{meta}) and on SiO_2 ($I_{PL}^{SiO_2}$). PL excited from the nanodisk side and emitted to the substrate side is detected. The excitation wavelength is 405 nm, which is far from the resonance wavelength of the Si nanodisk array. The PL spectrum is strongly modified on the nanodisk array; the broad featureless spectrum on SiO_2 is converted to that with a peak at 790 nm. In Figure 3-5(b), the ratio of the two spectra ($\frac{I_{PL}^{meta}}{I_{PL}^{SiO_2}}$) are shown together with the transmittance spectrum. The peak

of the PL ratio agrees fairly well with the transmittance dip of the coupled TD modes. This indicates that the strong modification of the PL spectral shape is caused by the coupling of the QD dipolar emitter with the TD modes of the Si nanodisk array.

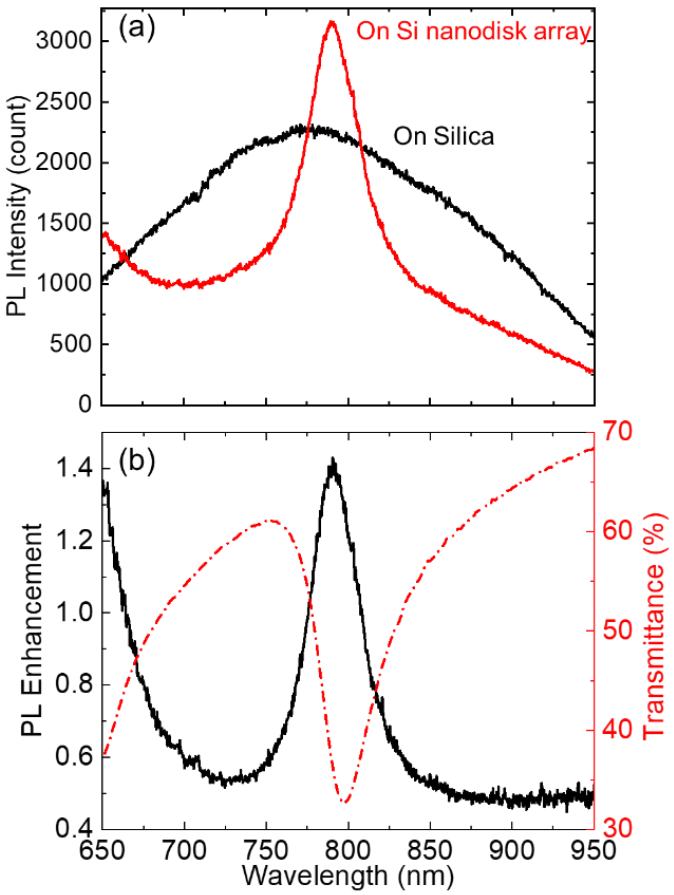

Figure 3-5 *(a)Photoluminescence spectra of Si QDs on a silica substrate (black curve) and on the Si nanodisk array (red curve). (b) PL enhancement (black) and transmittance spectrum of the Si nanodisk array (red dashed curve).*

We measured PL lifetime at different wavelengths. **Figure 3-6**(a-d) shows decay curves at 650 nm, 750 nm, 790 nm, and 850 nm. The decay rates on the nanodisk array are faster than that of silica substrate at all wavelengths. We estimate the decay rates with fitting these results by a stretched exponential function, written by[148,149]

$$I(t) = exp\left\{-\left(\frac{t}{\tau}\right)^{\beta}\right\}, \tag{36}$$

where τ is a lifetime and β is stretched parameter, respectively. Then, the average lifetime is defined as

$$\tau_{ave} = \frac{\tau}{\beta}\Gamma_E\left(\frac{1}{\beta}\right), \tag{37}$$

where Γ_E is the Euler gamma function. Using τ_{ave}, the decay rate is defined by

$$\gamma = \frac{1}{\tau_{ave}}. \tag{38}$$

When fitting and calculating decay rate, we integrate the PL intensity per 20 nm ($\pm$ 10 nm). Figure 3-6 (e) shows the photoluminescence spectra on the nanodisk array and a silica substrate and decay rate enhancement ($\gamma^{meta}/\gamma^{SiO_2}$). Although the photoluminescence on the nanodisk array is modified at 790 nm due to a toroidal dipole resonance, the decay rate enhancement is featureless and gradually decreases to longer wavelength. These results indicate that the

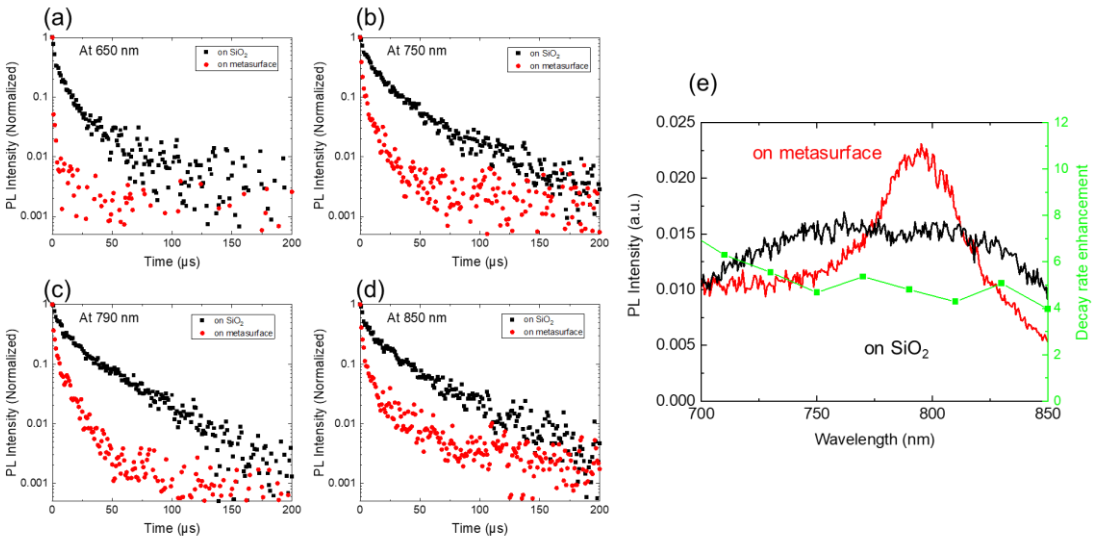

Figure 3-6 *(a-d) PL lifetime at (a)650 nm, (b)750 nm, (c)790 nm, and (d)850 nm on the nanodisk array (red circle) and a silica substrate (black circle). (e) Photoluminescence spectra of Si QDs on a silica substrate (black curve) and on the Si nanodisk array (red curve), and decay rate enhancement (green squires)*

nonradiative decay rate enhancement contributes to shorten life time and this photoluminescence enhancement is not caused by quantum efficiency (radiative decay rate) enhancement.

Figure 3-7(a) shows the angle resolved PL spectra on the Si nanodisk array. The dashed lines indicate RA wavelengths calculated by eq.(30) in chapter 2 and photoluminescence from Si QDs couples with these modes. And, at 790 nm, which is the toroidal dipole resonance wavelength, the photoluminescence is stronger inner $(\pm 1,0)$ order RAs. On the other hand, photoluminescence on a silica substrate has isotropic feature (Figure 3-7(b)). Figure 3-7(c) shows the radiation patterns of a QD monolayer on a flat SiO_2 substrate and the Si nanodisk array at 790 nm. On a flat SiO_2 substrate (black dots), the radiation pattern is almost isotropic, while on the Si nanodisk array (red dots), the out-of-plane emission is strongly enhanced. This is consistent with the calculated results (Figure 3-4), although the out-of-plane directionality is smaller due to uniform distribution of emitting dipoles on the whole surface of the nanodisks, existence of dipoles oriented to z-direction, structural imperfection, etc.

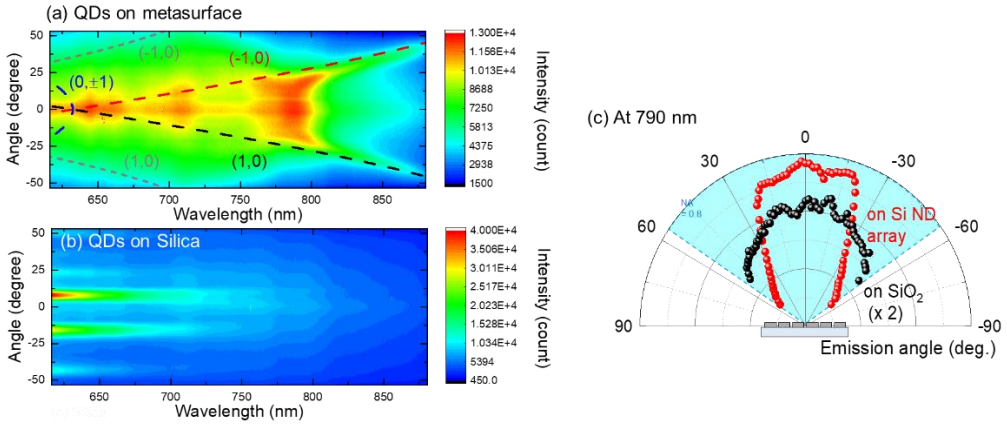

Figure 3-7 *(a,b) Angle resolved PL spectra on (a) the Si nanodisk array and (b) silica substrate. The dashed lines indicate RAs. (c) Radiation profiles on the Si nanodisk array (red dots) and on a silica substrate (black dots) at 790 nm.*

3.3 Conclusion

In this chapter, we studied the coupling effect between dipole emitters and a toroidal dipole resonance of a silicon hexagonal array. In the calculation results, although the radiative decay rate was 2.5-fold enhanced at toroidal dipole resonance, the non-radiative decay rate was about 7.5 times enhanced due to the absorption losses of poly Si. The nonradiative enhancement can be suppressed if we use single crystalline Si or emitters that have photoluminescence at longer wavelengths. Additionally, we revealed the collection efficiency is greatly enhanced (25 times) at the toroidal dipole resonance, which dominantly contributes to the photoluminescence enhancement. Then, we measured the PL lifetime and pattern on the Si metasurface. We demonstrated that the radiation pattern provided out-of-plane emission which enhanced the collection efficiency.

Chapter 4

Singlet-Triplet Direct Transition Enhancement of Molecules by Magnetic Field Enhancement

Adapted from Hiroshi Sugimoto, Hiroaki Hasebe, et. al., Small, 2021,17, 2104458

Photoexcitation of molecules is a fundamental process in light absorbers and emitters and in various photochemical reactions including photocatalytic reactions, photosensitizations and photosyntheses[150,151]. In particular, photoexcitation of a long-lived triplet excited state (T_1) plays crucial roles in some photosensitizing activities[152,153] and triplet-triplet-annihilation type upconversion processes(TTA-UP).[154,155] In typical molecules, the ground state is spin singlet (S_0), and thus excitation to the triplet state requires intersystem crossing (ISC) from a singlet excited state (S_1).

Since the energy loss during ISC limits the energy efficiency of a total process, several strategies such as the relaxation of the selection rule by introducing heavy atoms in a molecule[156] are proposed. Another strategy is direct magnetic dipole $S_0 \rightarrow T_1$ transition by enhanced magnetic field[157]. According to the Fermi's golden rule, the transition rate from an initial ($|i\rangle$) to a final state ($|f\rangle$) is proportional to $\left|\langle f|H'|i\rangle\right|^2$, where H' is the light matter interaction Hamiltonian. The Hamiltonian is expanded by multipoles as

$$H' = -\boldsymbol{p}\cdot\boldsymbol{E} - \boldsymbol{m}\cdot\boldsymbol{B} - [q\nabla]\cdot\boldsymbol{E} - \cdots, \tag{39}$$

where $\boldsymbol{p}$ and $\boldsymbol{m}$ are electric and magnetic dipole transition moments, respectively, and $\boldsymbol{E}$ and $\boldsymbol{B}$ are electric and magnetic fields at a molecule position, respectively, and q is electric quadrupole tensor[157]. The electric dipole transition term ($-\boldsymbol{p}\cdot\boldsymbol{E}$) is orders of magnitude larger than the following terms and thus usually dominates the transition process. However, when the electric dipole transition is forbidden, the optical transition is controlled by the higher order terms such

as the magnetic dipole transition ($-\boldsymbol{m}\cdot\boldsymbol{B}$) and electric quadrupole transition ($-[q\nabla]\cdot\boldsymbol{E}$) terms.[158,159] Since spin-flip $S_0 \rightarrow T_1$ transition is allowed in the magnetic dipole transition, enhancement of the magnetic field at the transition frequency leads to efficient direct $S_0 \rightarrow T_1$ transition.

To enhance magnetic field in the optical frequency, nanoantennas composed of high refractive index dielectrics, such as silicon (Si), gallium phosphide (GaP), titanium dioxide (TiO_2), etc., are promising because they exhibit magnetic Mie resonances as well as the electric ones in the optical frequency. The enhanced magnetic field accompanied by the magnetic-type Mie resonances enhances the magnetic dipole emission rate of molecules and ions via the magnetic Purcell effect[160,161]. However, enhancing magnetic dipole transition excitation rate is still challenge because the enhanced magnetic field is confined inside the structure, which means molecules cannot access the field.

In this chapter, we demonstrate the magnetic dipole $S_0 \rightarrow T_1$ transition of Ru complex purely enhanced by an electromagnetic field of a metasurface. Inspired from the magnetic field distribution of a toroidal dipole resonance, we design metasurfaces leaking the enhanced magnetic field outside the structures efficiently. First, we calculate the magnetic field enhancement outside the structures induced by resonances and show that a toroidal dipole resonance possesses the ability to realize an accessible enhanced magnetic field. Then, we form Ru complex included PMMA film on Si metasurfaces and conduct photoluminescence excitation measurement of Ru complex to reveal the contribution of the electromagnetic field enhancement to $S_0 \rightarrow T_1$ excitation experimentally. We demonstrate 35-fold enhancement of the phosphorescence of the molecule by tuning the TD resonance of the metasurface to the $S_0 \rightarrow T_1$ transition wavelength. Comparing to calculation results, we show enhanced magnetic field accompanied by the TD mode of the nanodisk array enhances the direct $S_0 \rightarrow T_1$ transition of $RuPc(py)_2$.

4.1 Experimental Methods

- Optical properties of Pyridine-coordinated Ru(II) phthalocyanine ($RuPc(py)_2$)

Figure 4-1(a) shows the structure of pyridine-coordinated Ru(II) phthalocyanine ($RuPc(py)_2$) employed in this work to study the $S_0 \rightarrow T_1$ transition enhancement. Figure 4-1(b) shows the absorbance and photoluminescence (PL) spectra of $RuPc(py)_2$. The absorption peak around 630 nm corresponds to the Q-band of the phthalocyanine ($S_0 \rightarrow S_1$ transition). The Q-band is broader than that of typical metalated phthalocyanines, suggesting the MLCT ($d_\pi(Ru) \rightarrow \pi^*$(phthalocyanine)) contribution into the band[162,163]. The molecule exhibits the PL around 870 nm, which is assigned to the phosphorescence ($T_1 \rightarrow S_0$ transition). Figure 4-1(c) shows a simplified energy level diagram of $RuPc(py)_2$ obtained from optical measurements and time-dependent density functional theory (TD-DFT) calculations. The very weak and broad absorption band ranging from 700 to 820 nm in TD-DFT calculations indicates that the direct $S_0 \rightarrow T_1$ transition (absorption) occurs in the 700-820 nm range.

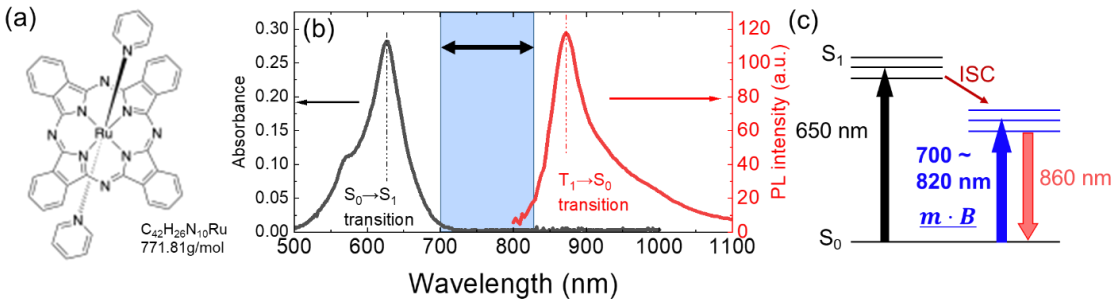

Figure 4-1 *(a) Structure of $RuPc(py)_2$. (b) absorbance (black curve) and phosphorescence (red curve) spectra of $RuPc(py)_2$ (c) Band scheme of $RuPc(py)_2$. The blue region in (b) indicates the energy of $S_0 \rightarrow T_1$ transition of $RuPc(py)_2$.*

Figure 4-2(a) shows a SEM image (tilt angle of 25°) of a Si nanodisk array fabricated by nanosphere lithography.[164] On top of that, a $RuPc(py)_2$ doped polymethyl methacrylate (PMMA) layer (30 nm in thickness, n = ~1.48) is deposited by spin coating (Figure 4-2(b)). We prepare

three different height nanodisk arrays (h = 27, 29, and 41.5 nm). A reference sample is produced by spin coating the same solution on a flat SiO_2 substrate. Figure 4-2(c) shows the measured transmittance spectra (solid curves) for the sample with different h. Clear transmittance dips due to the TD resonance are observed. The resonance wavelength is very sensitive to h and it shifts from 730 to 805 nm when h is changed from 27 to 41.5 nm. Simulated spectra are also shown as broken curves. Good agreements can be seen between experiments and calculations.

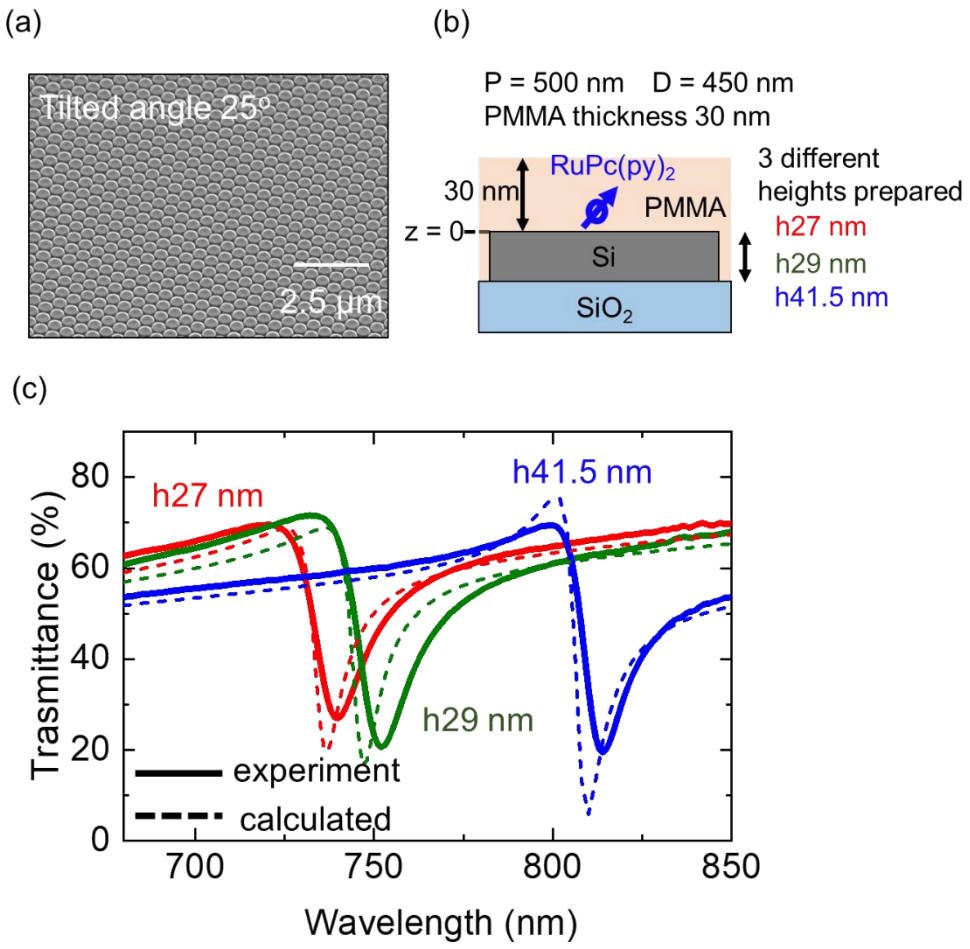

Figure 4-2 *(a)SEM image of a Si nanodisk array. (b) Schematic image of a Si nanodisk array with $RuPc(py)_2$ included PMMA layer. (c)Calculated (broken curve) and measured (solid curve) transmittance spectra of Si nanodisk arrays with 27 nm (red), 29 nm (green), and 41.5 nm (blue) in height.*

- Experimental methods of Photoluminescence excitation (PLE) spectra

Figure 4-3(a) shows the set up for a PLE measurement. PLE spectra of $RuPc(py)_2$ on a Si metasurface were obtained by using a single spectrometer equipped with a liquid-N_2-cooled charge coupled device (CCD) (Roper Scientific) as a detector though 2 longpass filters (LP750 and LP785). The PL signal is collected from the structure side with 30° by an optical lens (N.A. 0.3). A cw tunable Ti-sapphire laser (Spectra Physics, 3900S) is used as an excitation source. The excitation wavelength was changed from 700 to 820 nm. The excitation power was 35-40 mW, where the relation between PL intensity and excitation power is almost linear (slope: 0.93, Figure 4-3(b)), which indicates that the excitation process is one photon absorption with this power range. The PL intensity at 860 nm is normalized by the excitation power to obtain PLE spectra.

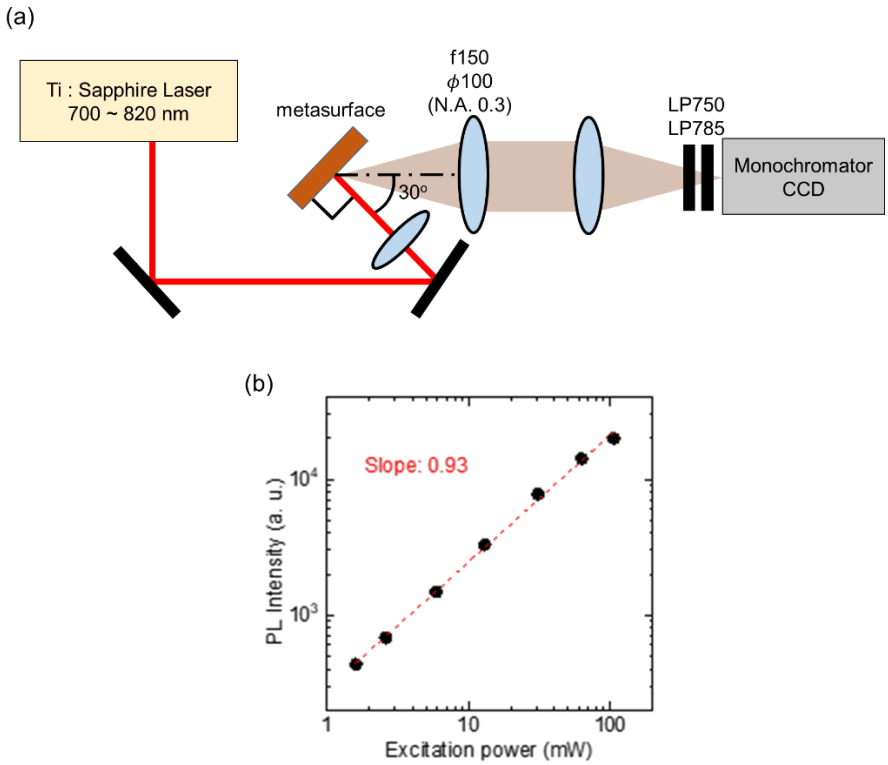

Figure 4-3 *(a)Experimental setup of PLE measurement. (b) Excitation power dependence of the PL intensity of $RuPc(py)_2$ at 860 nm for a metasurface with h = 41.5 nm. Red dashed line shows a result of linear fitting.*

- Estimating PL enhancement factor (EF) with FDTD simulation

In the linear region of PL excitation like the case in this work, the PL EF is expressed as $EF_{total} = \frac{\sigma_{ex}^{MS}(\lambda_{ex})}{\sigma_{ex}^{ref}(\lambda_{ex})}\frac{Q^{MS}(\lambda_{em})}{Q^{ref}(\lambda_{em})}\frac{\eta^{MS}(\lambda_{em})}{\eta^{ref}(\lambda_{em})}$,[146] where σ_{ex} is an excitation rate of $RuPc(py)_2$ at the excitation wavelength (700-820 nm), and Q is a quantum efficiency, and η is an emission collection efficiency. The superscripts "MS" and "ref" indicate $RuPc(py)_2$ doped PMMA on a Si metasurface and on a silica substrate, respectively. If the excitation is due to the $S_0 \rightarrow S_1$ electric dipole transition, the excitation enhancement ($\frac{\sigma_{ex}^{MS}(\lambda_{ex})}{\sigma_{ex}^{ref}(\lambda_{ex})}$) is proportional to the intensity of the incident electric field($|E(\lambda_{ex})|^2/|E_0(\lambda_{ex})|^2$), while, if the excitation is made via the spin-flip $S_0 \rightarrow T_1$ transition, it is proportional to the magnetic field intensity($|H(\lambda_{ex})|^2/|H_0(\lambda_{ex})|^2$). Considering the molecules dispersed in PMMA homogeneously, we calculate field intensities averaged over z = 0 to 30 nm (**Figure 4-4**(a)), written as

$$\frac{\sigma_{ex}^{MS}(\lambda_{ex})}{\sigma_{ex}^{ref}(\lambda_{ex})} = \frac{\int_{V_{PMMA}} |E_{enh}(\lambda_{ex})|^2 \; or \; |H_{enh}(\lambda_{ex})|^2}{V_{PMMA}}, \tag{40}$$

where $E_{enh}(\lambda_{ex}) = |\boldsymbol{E}_{MS}(\lambda_{ex})|/|\boldsymbol{E}_{silica}(\lambda_{ex})|$ and $|H_{enh}(\lambda_{ex})| = |\boldsymbol{H}_{MS}(\lambda_{ex})|/|\boldsymbol{H}_{silica}(\lambda_{ex})|$.

The contribution of the radiative rate (γ) and the collection efficiency (η) on the modification of phosphorescence is obtained by calculating the far-field radiated power integrated over angles defined by N.A. of the collection optics in the experiment. From these values, the emission enhancement factor ($\frac{Q^{MS}(\lambda_{em})}{Q^{ref}(\lambda_{em})}\frac{\eta^{MS}(\lambda_{em})}{\eta^{ref}(\lambda_{em})}$) can be calculated if the initial quantum yield of an emitter (Q^0) is known. In this work, the measured quantum efficiency of $RuPc(py)_2$ is ~0.3% and thus $\frac{Q^{MS}(\lambda_{em})}{Q^{ref}(\lambda_{em})}$ is almost equal to $\frac{\gamma^{MS}(\lambda_{em})}{\gamma^{ref}(\lambda_{em})}$.[165] An *x*- and a *z*-oriented dipole was placed at the center of the PMMA layer (at z = 15 nm in Figure 4-2(b)) on a Si nanodisk array. The fields at the PMMA side were captured by a large 2D monitor (*xy*-plane) covering the entire simulation region

(Figure 4-4(b)). Similar simulation was performed for a dipole placed at the center of a 30 nm thick PMMA layer on a flat SiO_2 substrate as a reference.

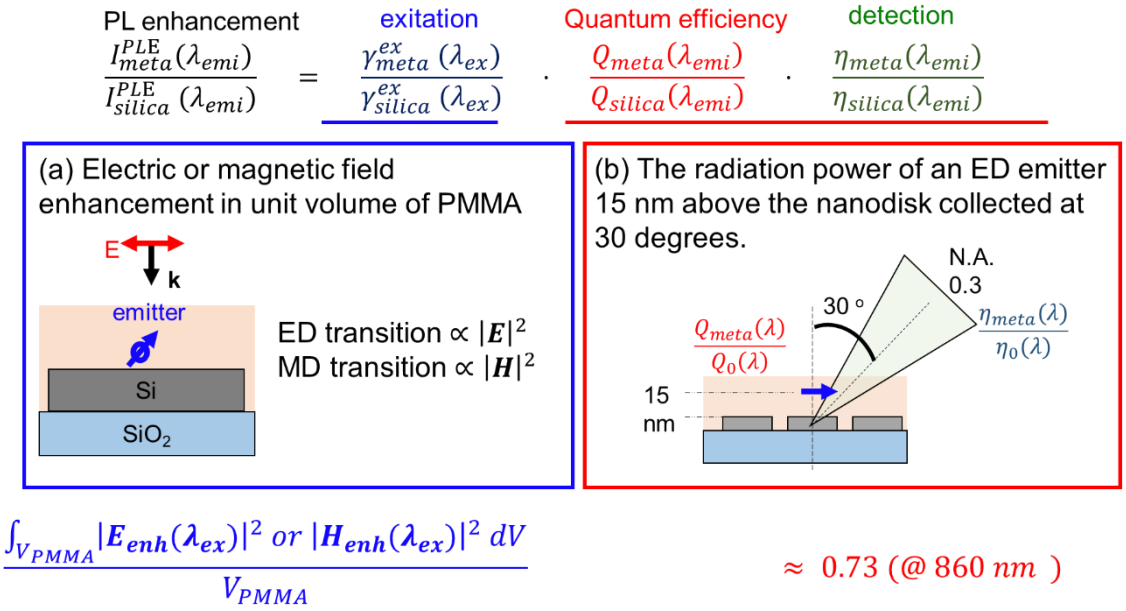

Figure 4-4 *Schematic illustrations of a structures for the calculation of PL enhancement factors*

4.2 Results and Discussion

- Magnetic field enhancement: Toroidal dipole resonance vs other modes

First, we discuss which mode we can get the highest magnetic field outside of structure. **Figure 4-5**(a-c) shows the calculated transmittance, reflectance, and absorptance spectrum of a Si nanodisk array with *P = 500 nm, D =450 nm,* and *h* = 150 nm. The background refractive index is set to 1.43, which is the refractive index of dimethylformamide (DMF) solution used for the photochemical reaction experiments (Chapter 5). We can see three distinctive resonances in the wavelength range. The result of multipole decomposition for the *h* = 150 nm spectrum and the field distributions at the resonance wavelengths are shown in Figure 4-5(d-g). In addition to Eq.(18-28), we perform the decomposition related to toroidal quadrupole (TQ) mode. This moment is described by[26]

$$T_{\alpha\beta} = \frac{1}{28c}\int \left[4r_\alpha r_\beta(\boldsymbol{r}\cdot\boldsymbol{J}(\boldsymbol{r})) - 5r^2(r_\alpha J_\beta + r_\beta J_\alpha) + 2r^2(\boldsymbol{r}\cdot\boldsymbol{J}(\boldsymbol{r}))\delta_{\alpha,\beta}\right]d^3r. \quad (41)$$

Then, the scattering power is

$$I_{TQ} = \frac{\omega^8}{45c^7}\Sigma|T_{\alpha\beta}|^2. \quad (42)$$

From the field distributions and multipole decomposition, the longest wavelength narrow dip is assigned to the TD mode. Other dips are assigned to the magnetic dipole (MD) mode and the TQ mode.

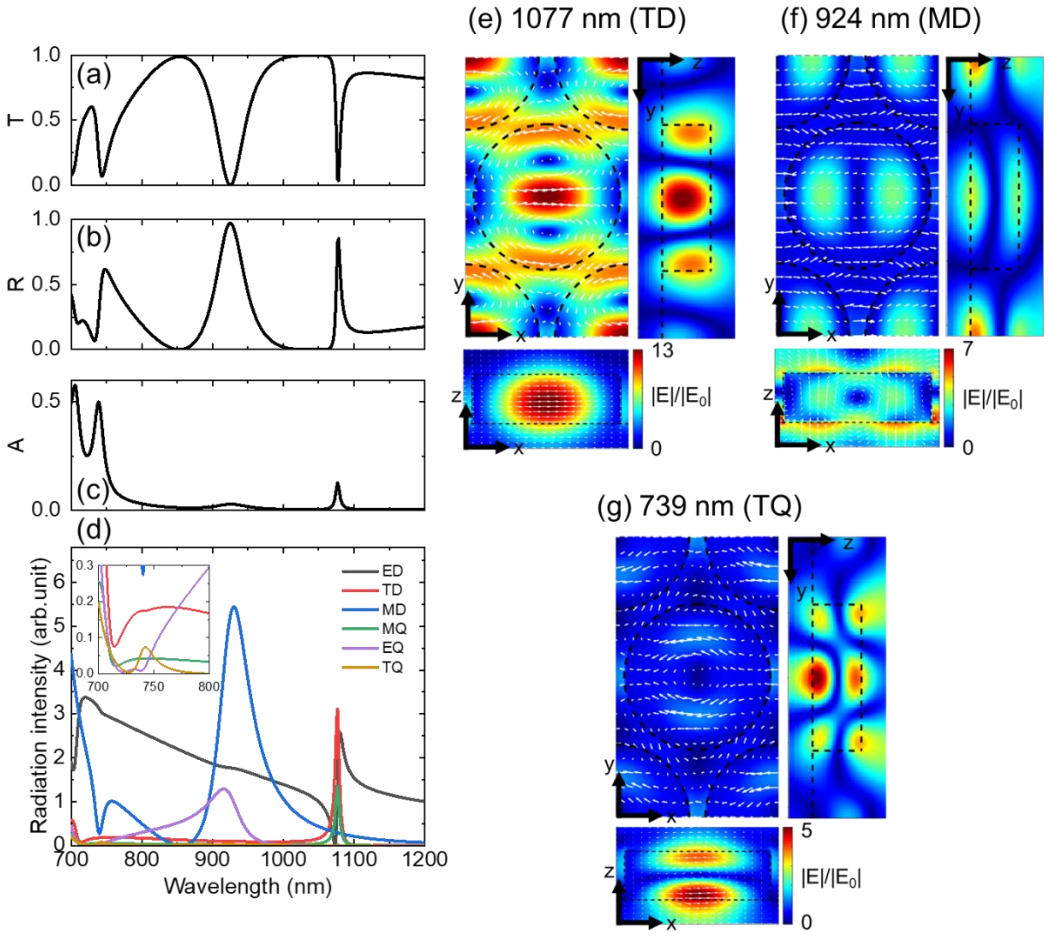

Figure 4-5*(a) Transmittance, (b)Reflectance, (c) Absorptance, and (d) Radiation intensity spectra of a Si nanodisk array with 500 nm in period, 450 nm in diameter, and 150 nm in height. (e-g) The field distributions (|E|/|E₀|) at (e) toroidal dipole (1077 nm), (f) magnetic dipole (924 nm), and (g) toroidal quadrupole (734 nm) resonances. The background refractive index is 1.43.*

To control the resonance wavelength and maximize the magnetic field intensity at the surface, the disk height (h) is changed, while the period (P) and diameter (D) are fixed to 500 nm and 450 nm, respectively. **Figure 4-6**(a) shows the contour plot of transmittance spectra. These resonance wavelengths can be controlled from 700 to 1200 nm, which covers $S_0 \rightarrow T_1$ transition energy of Ru(II) complexes. Figure 4-6(b) shows the enhancement factor of the magnetic field intensity at 1 nm above the surface of a Si nanodisk array averaged over the whole surface as functions of h and wavelength. On the right panel, the enhancement factor at 835 nm is shown. This wavelength corresponds to $S_0 \rightarrow T_1$ direct transition of $RuPc(py)_2$. The enhancement factor reaches >100-fold at the TD resonance in a wide h range (44-160 nm), and is over 120-fold at h ~ 50 nm. Figure 4-6(c) shows the magnetic field enhancement factor of a nanodisk array and a silica substrate as a function of the distance from the surface. Over 100-fold enhancement of the magnetic field intensity is sustained even at 12 nm away from the surface, which can be exploited for $S_0 \rightarrow T_1$ direct transition of molecules attached on the surface. Compared to the TD mode, the enhancement factors of the TQ resonance (~60) and the MD resonance (~5) at 1 nm from the surface are smaller due to the stronger confinement of the field.[9]

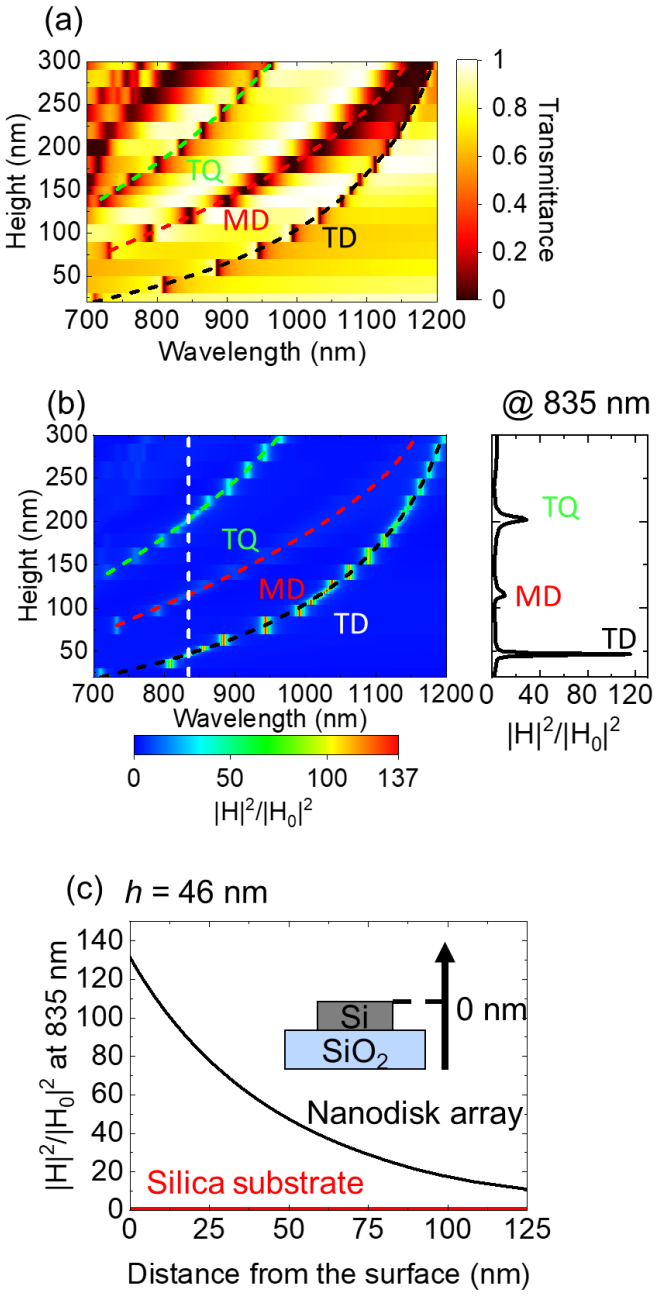

Figure 4-6 *(a) Contour map of transmittance spectra of Si nanodisk array (P = 500 nm, D = 450 nm) with different heights (20~300 nm).(b)(Left panel) Contour map of magnetic field enhancement ($|H|^2/|H_0|^2$) as functions of wavelengths and height, and (Right panel) $|H|^2/|H_0|^2$ at 835 nm as a function of height (shown by the white dashed line in the contour map) 1 nm above the surface. (c) Magnetic field enhancement factors of a nanodisk array with 46 nm in height (black) and a silica substrate (red) as a function of the distance from the surface. The background refractive index is 1.43.*

- Magnetic field enhancement induced in PMMA layer at a toroidal dipole resonance

Figure 4-7(a) shows a schematic of a dielectric metasurface composed of a hexagonal array of thin silicon (Si) nanodisks. The surface is covered with a 30 nm thick polymethyl methacrylate (PMMA) thin film. In actual samples, $RuPc(py)_2$ are doped in the PMMA layer as phosphorescent probes. Figure 4-7(b) shows the calculated transmittance (T) and reflectance (R) spectra of a nanodisk array placed on a SiO_2 substrate The D and h are 450 nm and 41.5 nm, respectively. The period of the array (P) is 500 nm. We can see a resonance at 806 nm which is a toroidal dipole resonance. Figure 4-7(c) shows the absorptance (A) defined by A=1-T-R. We can see strong enhancement of the absorption at 806 nm. The absorption peak appears at shorter wavelength side of the transmittance dip. The Q factor of the absorption peak is 124 and absorption in off-resonant wavelengths (e.g. 850-950 nm) is negligibly small. This is due to low-loss nature of the Si metasurface, which is an advantage compared to plasmonic counterparts for studying the light emission of an attached molecule. The resonance wavelength can be controlled by varying D and h.[164] In this work, we change h to adjust the resonance wavelength to $S_0 \rightarrow T_1$ transition of $RuPc(py)_2$. In this study, we consider the magnetic dipole transition term in Eq.(40). Absorption due to the magnetic dipole transition is proportional to the magnetic field intensity. Figure 4-7(d,f) shows distributions (xy-plane) of the magnetic field intensity normalized by that of incident light ($|H|^2/|H_0|^2$) in a nanodisk (z = -h/2 = -20.75 nm) and above a nanodisk, *i.e.*, in a PMMA layer (z = 15 nm), at 806 nm. The electric field distributions are also shown in Figure 4-7(d,f) The magnetic field distributions at different cross sections as well as the electric field distributions are shown in Figure 4-7(h,i). The field distribution in Figure 4-7(d,e) exhibits a characteristic feature of the TD resonance.[164] The $|H|^2/|H_0|^2$ reaches ~500 in a nanodisk (z = -h/2) and ~300 in a PMMA layer (z = 15 nm). Therefore, by exploiting the TD resonance, large enhancement of the magnetic dipole $S_0 \rightarrow T_1$ transition is expected for molecules embedded in PMMA.

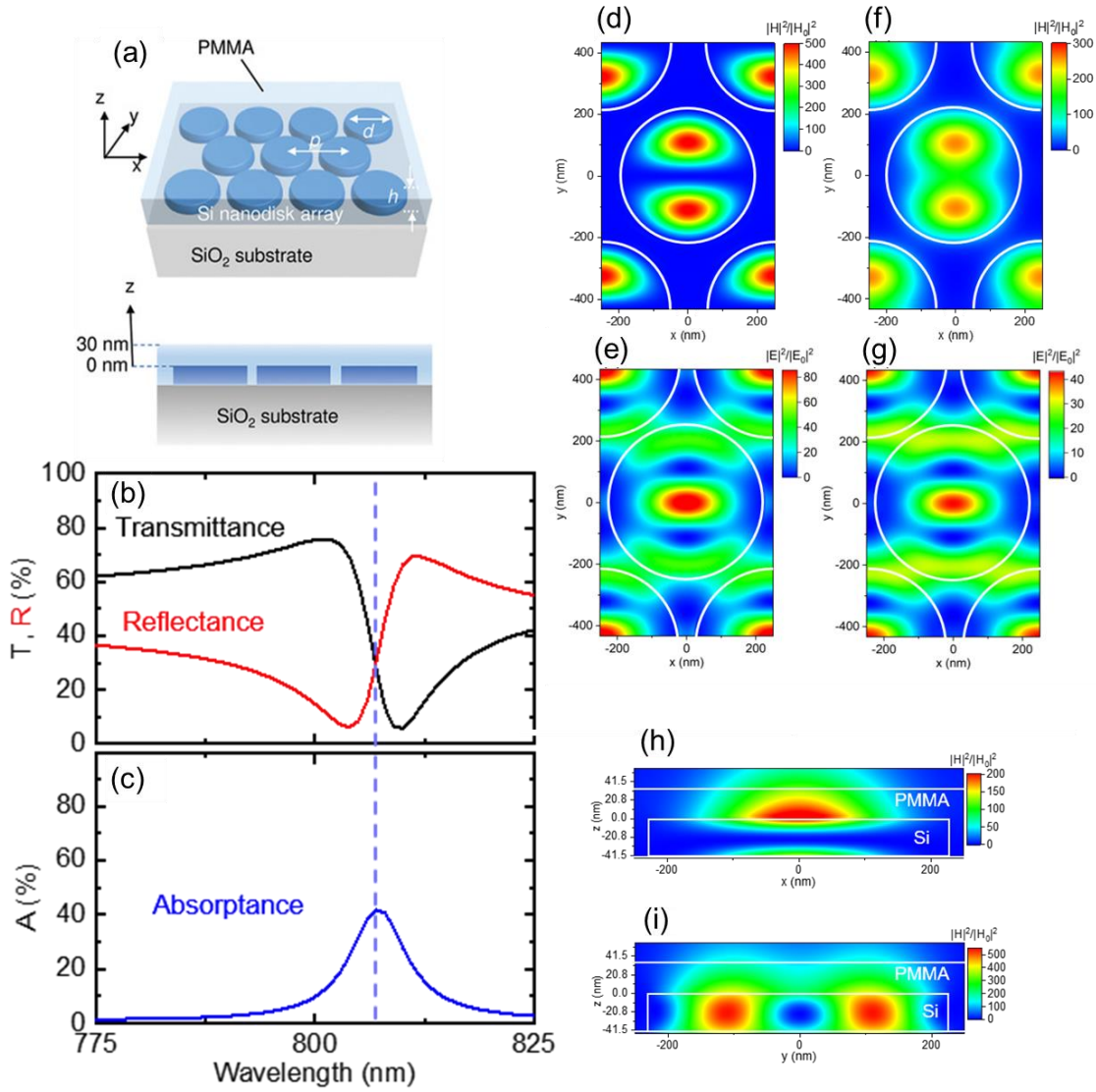

Figure 4-7 *(a) Schematic image of a Si nanodisk array with PMMA. (b)Transmittance, reflectance, and (c) absorptance spectra of the Si nanodisk array with P = 500 nm, D = 450 nm, h = 41.5 nm. Distributions of (d,f) magnetic and (e,g) electric field intensity in an xy plane at (d,e) the middle of nanodisks (z = -20.75 nm) and (f,g) above nanodisks (z = 15 nm). (h,i) Distributions of magnetic field intensity in (h) xz and (i) yz planes.*

Figure 4-8(a) shows the enhancement factors of the electric ($|E(\lambda_{ex})|^2/|E_0(\lambda_{ex})|^2$) and magnetic ($|H(\lambda_{ex})|^2/|H_0(\lambda_{ex})|^2$) field intensities averaged over z = 0 to 30 nm obtained by Eq.(41)

as a function of wavelength. Both the electric and magnetic fields are enhanced at the TD resonances; the enhancement factor of the magnetic field is approximately twice or larger than that of the electric field for all the samples. Especially, the magnetic field intensity reaches 60-fold enhancement at 806 nm with h = 41.5 nm Si nanodisk array, which is expected to promote direct $S_0 \rightarrow T_1$ transition greatly. Figure 4-8(b) shows $\frac{\gamma^{MS}(\lambda_{em})}{\gamma^{ref}(\lambda_{em})}\frac{\eta^{MS}(\lambda_{em})}{\eta^{ref}(\lambda_{em})}$ (Figure 4-4(b)) of Si nanodisk arrays with h = 27, 29, and 41.5 nm. Although the some perturbations in spectra occur due to the structure of nanodisk arrays, the value of $\frac{\gamma^{MS}(\lambda_{em})}{\gamma^{ref}(\lambda_{em})}\frac{\eta^{MS}(\lambda_{em})}{\eta^{ref}(\lambda_{em})}$ are almost the same for three metasurface samples at the phosphorescence detection wavelength for the PLE measurements (860 nm); they are 0.73, 0.72 and 0.72 for metasurfaces with h = 27, 29 and 41.5 nm, respectively.

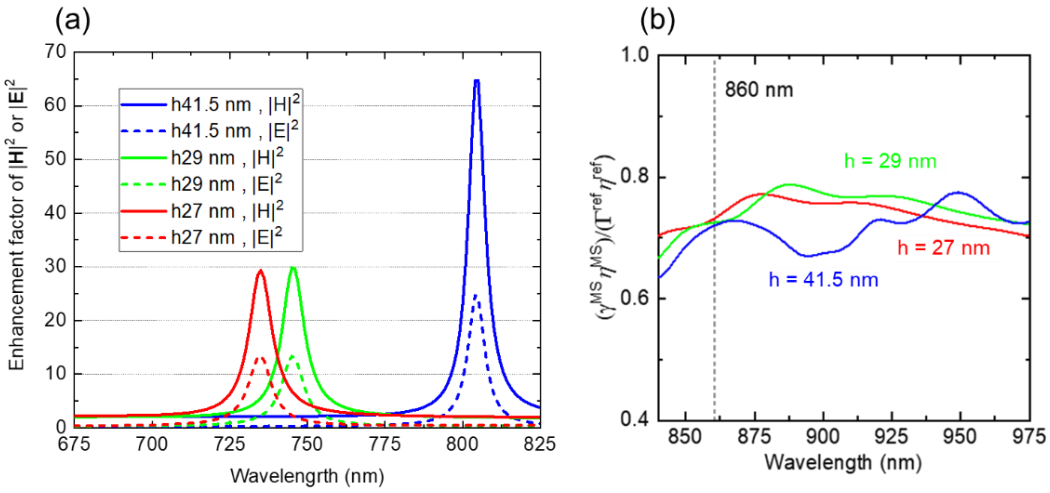

Figure 4-8*(a) Calculated enhancement spectra of incident electric field $|E|^2/|E_0|^2$ (dashed curves) and magnetic field $|H|^2/|H_0|^2$ (solid curves) for three metasurface samples. (b)* $\frac{\gamma^{MS}(\lambda_{em})}{\gamma^{ref}(\lambda_{em})}\frac{\eta^{MS}(\lambda_{em})}{\eta^{ref}(\lambda_{em})}$ *spectra of metasurfaces with h = 27 (red), 29 (green) and 41.5 nm (blue).*

- PLE measurement results with different height SI nanodisk array

Figure 4-9(a) shows the PL spectra of $RuPc(py)_2$ on the silicon nanodisk array with 41.5 nm in height and silica substrate excited at 805 nm which is the toroidal dipole resonance wavelength of the nanodisk array. The fluctuation of the phosphorescence band in the longer wavelength range is due to modulation of the emission process by the metasurface shown in Figure 4-8(b). The PL intensity is greatly enhanced on the Si nanodisk array(~35-fold). Because the molecule have no detectable absorption around 805 nm (see Figure 4-1(b)), the excitation is most likely via the spin-forbidden $S_0 \rightarrow T_1$ magnetic dipole transition. Figure 4-9(b) shows the PLE spectra detected at 860 nm for three samples with different *h* together with that of a reference sample (black dashed curve), *i.e*., a $RuPc(py)_2$ doped PMMA film on a silica substrate. The PL excitation is made in the linear regime (Figure 4-3(b)), *i.e*., the phosphorescence intensity is proportional to the excitation power, where a PLE spectrum represents an absorption spectrum. The PLE spectrum of the reference sample is featureless and the intensity becomes small as the wavelength deviates from that of the allowed $S_0 \rightarrow S_1$ transition of $RuPc(py)_2$ (~650 nm) (Figure 4-1(b)). In stark contrast to this, $RuPc(py)_2$ on the metasurfaces shows distinct PLE peaks. The peak wavelengths are very close to those of transmittance dips, although they are consistently slightly shorter than them (Figure 4-9(c)). This is consistent with the relation between calculated absorption and transmittance spectra in Figure 4-7. Therefore, the observed excitation enhancement of $RuPc(py)_2$ is due to the enhanced absorption induced by TD resonance of the metasurface.

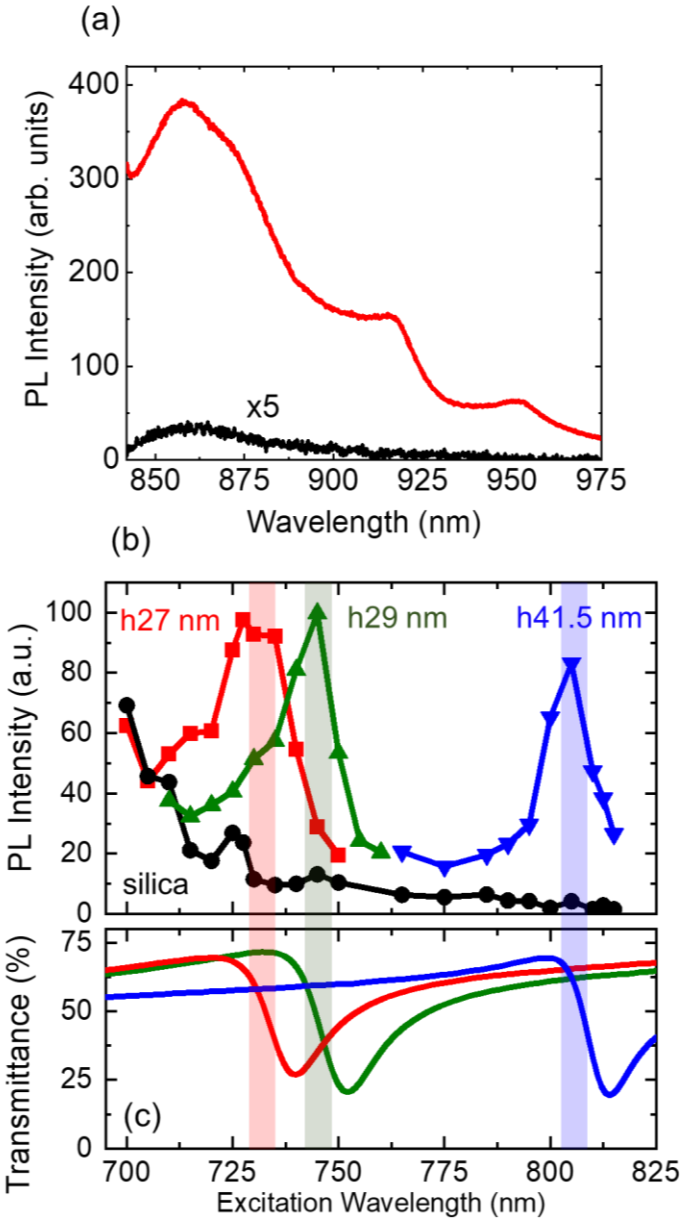

Figure 4-9 *(a) PL spectra of $RuPc(py)_2$ molecules placed on Si metasurface with h = 41.5 nm (red curve) and the reference sample (black curve). The excitation wavelength is 805 nm. (b)PLE spectra of $RuPc(py)_2$ on Si nanodisk array with 27 nm (red), 29 nm (green), and 41.5 nm (blue) in height and silica substrate (black). (c) Transmittance spectra of Si nanodisk arrays.*

We now consider the observed phosphorescence enhancement quantitatively. **Figure 4-10**(a) shows the phosphorescence enhancement factor (EF_{exp}) obtained by dividing PLE spectra of three metasurface samples by that of the reference sample. The peak EF_{exp} are 6.5 (730 nm), 10 (745 nm) and 35 (805 nm) for metasurfaces with h = 27, 29 and 41.5 nm, respectively. Figure 4-10(b) shows calculated enhancement factor obtained by multiplying the field enhancement spectra and $\frac{\gamma^{\mathrm{MS}}(\lambda_{em})}{\gamma^{\mathrm{ref}}(\lambda_{em})}\frac{\eta^{\mathrm{MS}}(\lambda_{em})}{\eta^{ref}(\lambda_{em})}$ at 860 nm shown in Figure 4-8, which gives us the total EFs of the $T_1 \rightarrow S_0$ phosphorescence for the excitation via the $S_0 \rightarrow S_1$ electric dipole (EF_{total_E}) and $S_0 \rightarrow T_1$ magnetic dipole (EF_{total_H}) transitions. Since the values of $\frac{\gamma^{\mathrm{MS}}(\lambda_{em})}{\gamma^{\mathrm{ref}}(\lambda_{em})}\frac{\eta^{\mathrm{MS}}(\lambda_{em})}{\eta^{ref}(\lambda_{em})}$ at 860 nm is almost the same (0.72-0.73) for all the samples, the overall feature of Figure 4-10(b) is very similar to that of Figure 4-8(a). The comparison between the calculated and experimental EFs provides a deep insight about the mechanism of the phosphorescence enhancement. First, we assume that the observed phosphorescence is excited solely via the $S_0 \rightarrow S_1$ electric dipole transition. In that case, the calculated total enhancement factors ($EF_{\mathrm{total\_E}}$) are ~9 for the metasurfaces with h = 27 and 29 nm and ~17 for that with h = 41.5 nm. For the metasurfaces with h = 27 and 29 nm, these values of $EF_{\mathrm{total\_E}}$ agree well with the measured EF_{PL} (6.5 and 10-folds, respectively). On the other hand, for the metasurface with h = 41.5 nm, it is much smaller than the measured EF_{PL} (35-fold). Therefore, the observed large EF_{PL} of the metasurface with h = 41.5 nm under 805 nm excitation cannot be explained by the enhancement of the $S_0 \rightarrow S_1$ electric dipole transition by the electric field enhancement. The most probable explanation of the observed large EF_{PL} is that excitation around 805 nm is predominantly due to the $S_0 \rightarrow T_1$ magnetic dipole transition and it is enhanced by the enhanced magnetic field of the metasurface. In fact, EF_{PL} of 35-fold is not far from the calculated $EF_{\mathrm{total\_H}}$ (46-fold). Although partial contribution of the $S_0 \rightarrow S_1$ electric dipole transition cannot be fully excluded, our results clearly show that enhanced magnetic field of a dielectric metasurface contributes to the enhancement of spin-flip $S_0 \rightarrow T_1$ transition of a molecule.

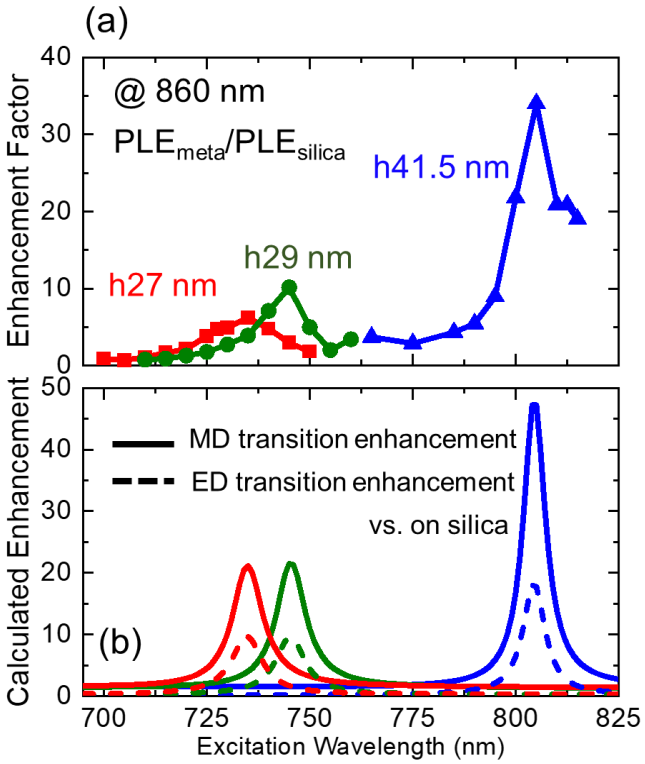

Figure 4-10 *(a) Measured PL enhancement and (b) Calculated total enhancement factor when excited via the $S_0 \rightarrow S_1$ electric dipole transition (dashed curves) and via the $S_0 \rightarrow T_1$ magnetic dipole transition (solid curves) for three metasurface samples.*

4.3 Conclusion

We achieved large enhancement of direct $S_0 \rightarrow T_1$ transition (absorption) of a molecule by the enhanced magnetic field induced by a Si metasurface with a coupled TD resonance. The absorption enhancement was monitored by the excitation spectra of phosphorescence of $RuPc(py)_2$ placed on the metasurface. We showed TD resonance can realize higher magnetic field than magnetic dipole and toroidal quadrupole modes. In experiments, we demonstrated the phosphorescence intensity was enhanced at maximum 35-fold when the excitation wavelength was in the $S_0 \rightarrow T_1$ transition range. These results indicate that photon energy necessary to excite the T_1 state can be reduced by more than 400 meV compared to the process involving the ISC.

Quantitative analyses in combination with numerical simulations revealed that the large absorption enhancement cannot be explained by the enhancement of the $S_0 \rightarrow S_1$ transition by the electric field enhancement, and is predominantly due to the enhancement of the $S_0 \rightarrow T_1$ magnetic dipole transition by the enhanced magnetic field.

Chapter 5

Enhancement of Singlet Oxygen Generation Efficiency

Adapted from Hiroaki Hasebe et. al., Small, 2023, 2302519

In Chapter 4, we achieved $S_0 \rightarrow T_1$ magnetic dipole transition enhancement by the magnetic field induced by a toroidal dipole resonance. In this chapter, we develop a functional metasurface composed of a thin Si nanodisk array and photosensitizing molecules to utilize it for a photochemical platform. In this system, the Ru complexes directly attach to a Si metasurface not to obstruct the energy transfer from Ru complexes to other molecules (**Figure 5-1**(a)). First, we confirm $S_0 \rightarrow T_1$ magnetic dipole transition enhancement occurs on this metasurface by PLE measurement. Then, we examine the performance of this functional metasurface by detecting singlet oxygen ($^1O_2$) generated via Dexter energy transfer from the T_1 state of $RuPc(py)_2$ under illumination of photons corresponding to the direct $S_0 \rightarrow T_1$ transition energy (Figure 5-1(b))[163]. We demonstrate that the Si nanodisk array functionalized with Ru(II) complexes works as a photosensitizing metasurface that accelerates photosensitized singlet oxygen generation reaction under the excitation of the direct $S_0 \rightarrow T_1$ transition of Ru(II) complexes.

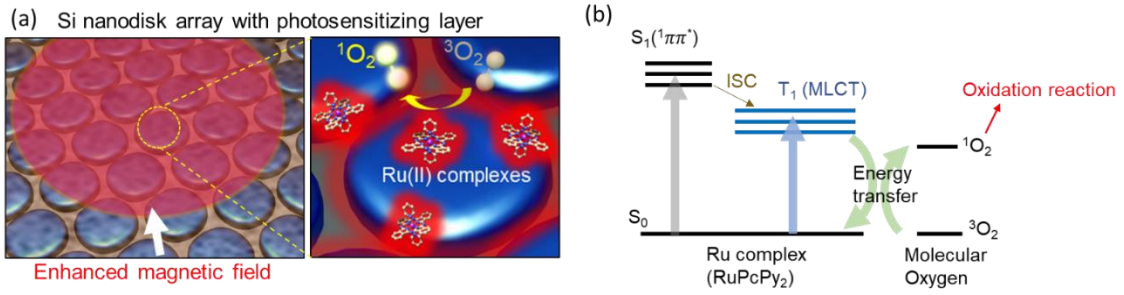

Figure 5-1 *(a) Schematic of a Si nanodisk array functionalized with photosensitizer ($RuPc(py)_2$). (b) Energy diagram of photosensitized $^1O_2$ generation process.*

5.1 Experimental Methods

To functionalize photosensitizer with a Si nanodisk array, we use carboxyl(COOH)-terminated RuPc(py)$_2$ (**Figure 5-2**(a)). The optical properties are almost same as RuPc(py)$_2$, shown in Figure 4-1. The absorbance peak related to S-S transition appears around 650 nm and the phosphorescence peak is around 870 nm. (Figure 5-2(b,c))

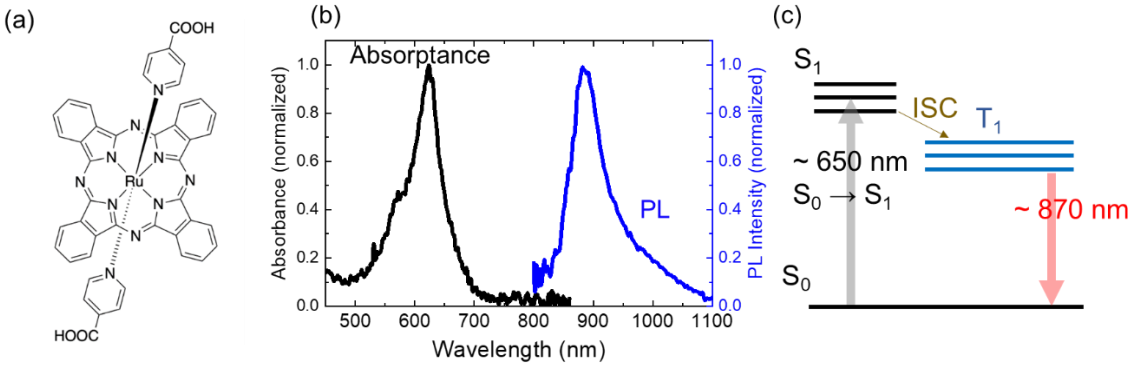

Figure 5-2 *(a)Structure, (b)absorbance (black) and phosphorescent (blue), and (c) the energy scheme of carboxyl(COOH)-terminated RuPc(py)$_2$*

We use a silicon nanodisk array fabricated by colloidal lithography method shown in **Figure 5-3**(a). The period, diameter, and height are 500 nm, 450 nm, and 46 nm, respectively. This nanodisk array has a toroidal dipole response around 820 nm with bare condition (Figure 5-3(b)).

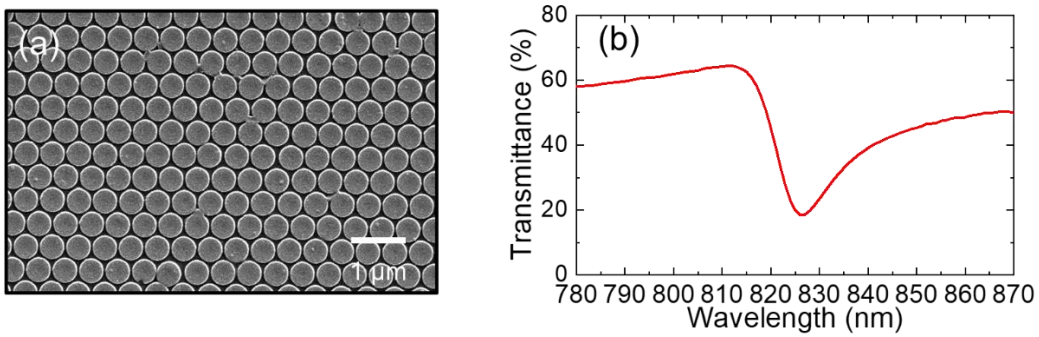

Figure 5-3 *(a)SEM image and (b) transmittance spectrum of a Si nanodisk array*

- *Functionalization of the Si nanodisk array with $RuPc(py)_2$*

Figure 5-4(a) shows the procedure of functionalizing Si nanodisks with $RuPc(py)_2$. A Si nanodisk array was treated with a UV ozone cleaner (110 °C, 20 min, SAMCO: UV-1) to create Si-OH on the surface and then functionalized with 3-aminopropyltriethoxysilane (APTES, >98.0%, Tokyo Chemical Industry Co., LTD) by immersing a Si nanodisk array in APTES solution (methanol : APTES = 3 ml : 200 µl) over night (~20 h) at 40 °C to obtain NH_2-termination on the surface. The Si nanodisk array was rinsed with methanol and dried at 110°C for 20 min to promote dehydration condensation of APTES with Si-OH. Carboxyl terminated $RuPc(py)_2$ were conjugated by peptide bonding using 4-(4,6-dimethoxy-1,3,5-triazin-2-yl)-4-methylmorpholium chloride (DMT-MM) (>95%, Tokyo Chemical Industry Co., LTD) as a condensing agent in phosphate-buffered saline (PBS) buffer (pH 7.4). 1.7 mL of methanol containing $RuPc(py)_2$ (0.05 mg/ml) was mixed with 500 µl of methanol containing 10 mM DMT-MM. The Si nanodisk array was immersed in the mixture solution for 3 h with stirring, and rinsed in methanol with sonication for 1 min. An additional peptide bonding was formed between carboxyl terminated $RuPc(py)_2$ on a Si nanodisk array and 1-4 cyclohexanediamine (cis- and trans mixture, >97.0%, Tokyo Chemical Industry Co., LTD) with DMT-MM coupling followed by rinsing in methanol with sonication for 1 min. The process was repeated 4 times to obtain a $RuPc(py)_2$ multilayer on the nanodisk array.

Figure 5-4(b) shows the absorbance at 632 nm for different number of $RuPc(py)_2$ chemisorption processes. The absorbance is ~0.01 after the 1st process, and then increases ~0.002 in each additional process. If we assume that a monolayer of $RuPc(py)_2$ is formed in the first process, nearly a bilayer is formed after the 4th process.

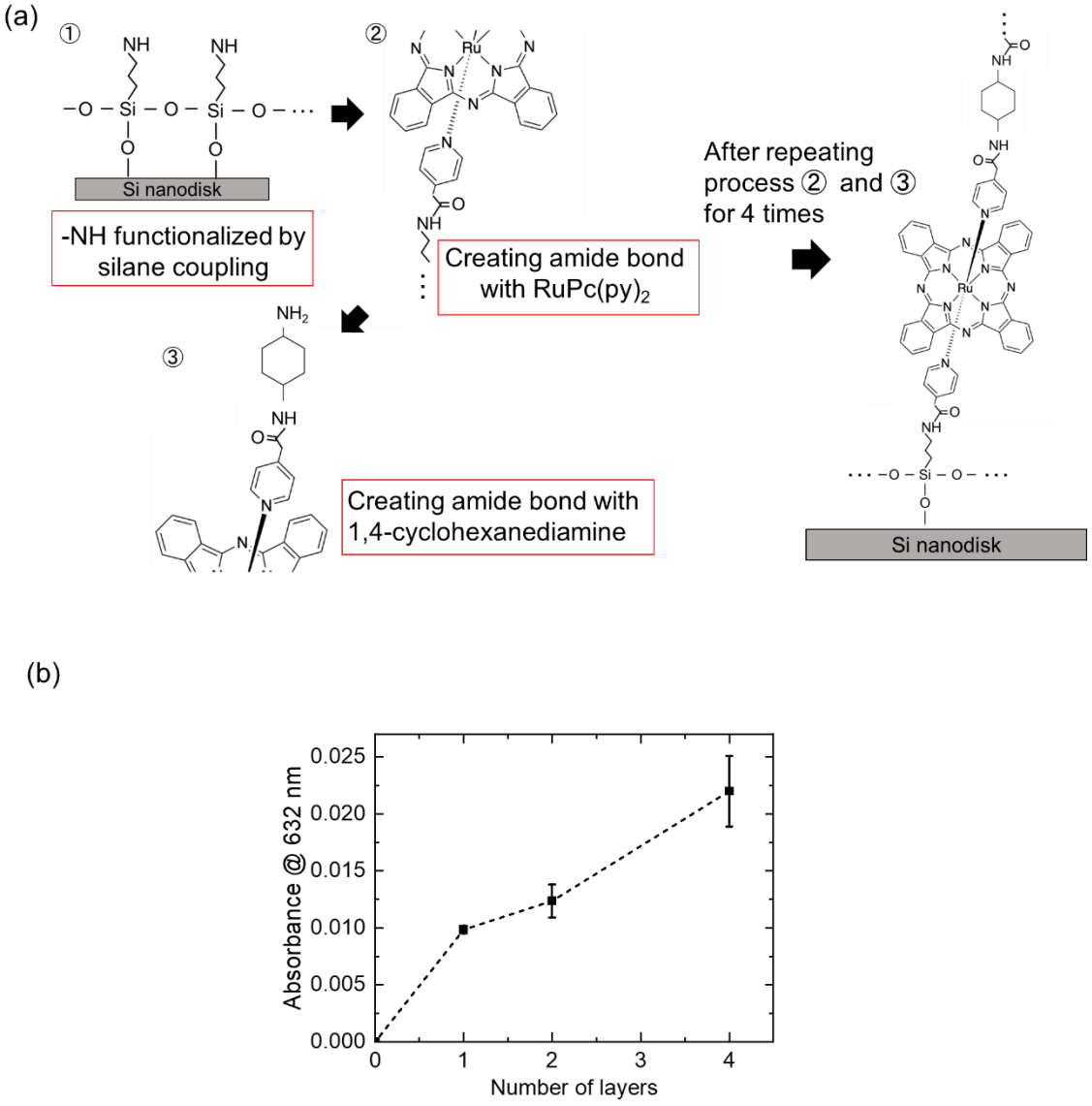

Figure 5-4 *(a) Functionalization process of COOH terminated RuPc(py)$_2$ on a Si nanodisk array. (b) The absorbance value at 632 nm of RuPc(py)$_2$ on a silica substrate as a function of number of the process.*

- *Measurement of $^1O_2$ generation rate from DPBF degradation*

1,3-Diphenylisobenzofuran (DPBF) (0.01 mM) (97.0%, Sigma-Aldrich) was dissolved in DMF. A Si nanodisk array functionalized with a RuPc(py)$_2$ multilayer was leant against the wall of a quartz cuvette (1 cm×1 cm×4.5 cm) filled with 1.5 mL DPBF solution, and illuminated from the normal to the surface for 90 min. The light source was a cw-Ti-sapphire laser (3900S,

Spectra Physics). The wavelength was changed from 790 to 860 nm, and the power was fixed to 110 mW. The solution was continuously stirred during light illumination. After light illumination, the transmittance spectrum of the DPBF solution was measured by a double-beam spectrophotometer (Shimadzu, UV-3101PC), and the change of the absorbance before and after light illumination was recorded.

5.2 Results and Discussion

Before conducting photochemical $^1O_2$ generation experiments, we study the capability of the metasurface for $S_0 \rightarrow T_1$ direct excitation of Ru complexes by PL and PL and PLE spectroscopy. For the enhancement of the direct excitation, the TD resonance of the metasurface should be in the 785-850 nm range. The PLE measurement is conducted by the same setup described in section 4.1. To prevent PL quenching by photooxidation, the surface is covered with a ~20 nm thick PMMA film. **Figure 5-5** shows photoluminescence spectra of $RuPc(py)_2$ on the nanodisk array with different excitation wavelength. That on silica substrate is also shown by the red dash curve. The PL is cut off under 900 nm with long-pass filter. The PL enhancement is enhanced the Si nanodisk array. The perturbation of PL on the Si nanodisk array is caused by the modified quantum efficiency and detection efficiency discussed in 4.2. We chose PL intensity at 950 nm to obtain PLE spectra.

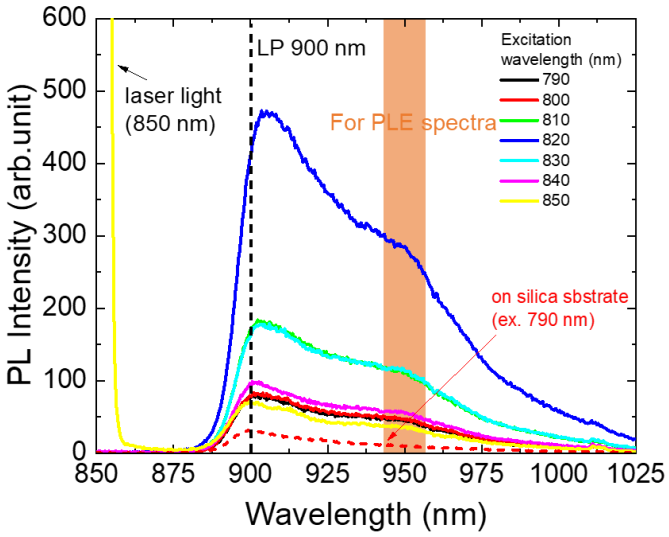

Figure 5-5 *Photoluminescence spectra of $RuPc(py)_2$ on the silicon nanodisk array (solid curve) and silica substrate (broken curve) with different excitation wavelength.*

Figure 5-6(a) shows the measured and calculated transmittance spectra of a Si nanodisk array on which a $RuPc(py)_2$ multilayer is formed (P = 500 nm, D = 450 nm, h = 46 nm). A Fano-like spectrum due to the TD resonance is seen around 820 nm. The experimental spectrum is well fitted by the Fano formula[139,140]. The resonance wavelength and the line width obtained by the fitting are 823 nm and 13 nm (Q = 63), respectively. The experimental spectrum is broader than the calculated one due probably to partial disorders in the array structure. Figure 5-6(b) shows the PL intensity at 950 nm as a function of excitation wavelength. The PLE spectrum of the reference is featureless because the measured wavelength range is out of the absorption band of $RuPc(py)_2$ (~630 nm). On the other hand, the PLE spectrum of $RuPc(py)_2$ on the Si nanodisk array has a peak at the TD resonance wavelength. Figure 5-6(c) shows the PL enhancement factor obtained by dividing the PLE spectra of $RuPc(py)_2$ on a Si nanodisk array by that of the reference. At the resonance wavelength, the PL intensity is 41-fold enhanced with respect to the reference. We also calculate PL enhancement factor. The method has already been described in 4.1. In this case, we calculate excitation enhancement factors of electric dipole transition and magnetic dipole

transition as the average field enhancement 1 nm above the surface (z = 1 nm), written by $\frac{\int_{S_{unit\ cell}} |E_{enh}(\lambda_{ex})|^2 \ or\ |H_{enh}(\lambda_{ex})|^2 dS}{S_{unit\ cell}}$, and put *x*-oriented dipole 1 nm above the nanodisk surface for $\frac{\gamma^{\mathrm{MS}}(\lambda_{em})}{\gamma^{\mathrm{ref}}(\lambda_{em})}\frac{\eta^{\mathrm{MS}}(\lambda_{em})}{\eta^{ref}(\lambda_{em})}$, which is 0.57 at 950 nm, considering to the molecular position. In Figure 5-6(c), the PL enhancement factor calculated by assuming the electric dipole ($|E(\lambda_{ex})|^2/\left|E_{ref}(\lambda_{ex})\right|^2$) (black) and magnetic dipole ($|H(\lambda_{ex})|^2/\left|H_{ref}(\lambda_{ex})\right|^2$) (red) transitions for the excitation process are shown. Note that the increase of the surface area by the formation of a Si nanodisk array (30% ($4.14\pi \times 10^4\ nm^2$ per unit cell) larger than that of silica substrate) is considered to compare the calculated enhancement factor with the measured one. The calculated enhancement factor spectra have a peak at the wavelength close to the experimental one. The peak value assuming the electric dipole transition is 22, while that assuming the magnetic dipole transition is 61. This value is very close to the experimentally enhancement factor (41-fold) considering some simplified assumptions in the calculation. Therefore, the enhanced direct $S_0 \rightarrow T_1$ transition of $RuPc(py)_2$ is due to the enhancement of the magnetic field by the TD resonance of a Si nanodisk array.

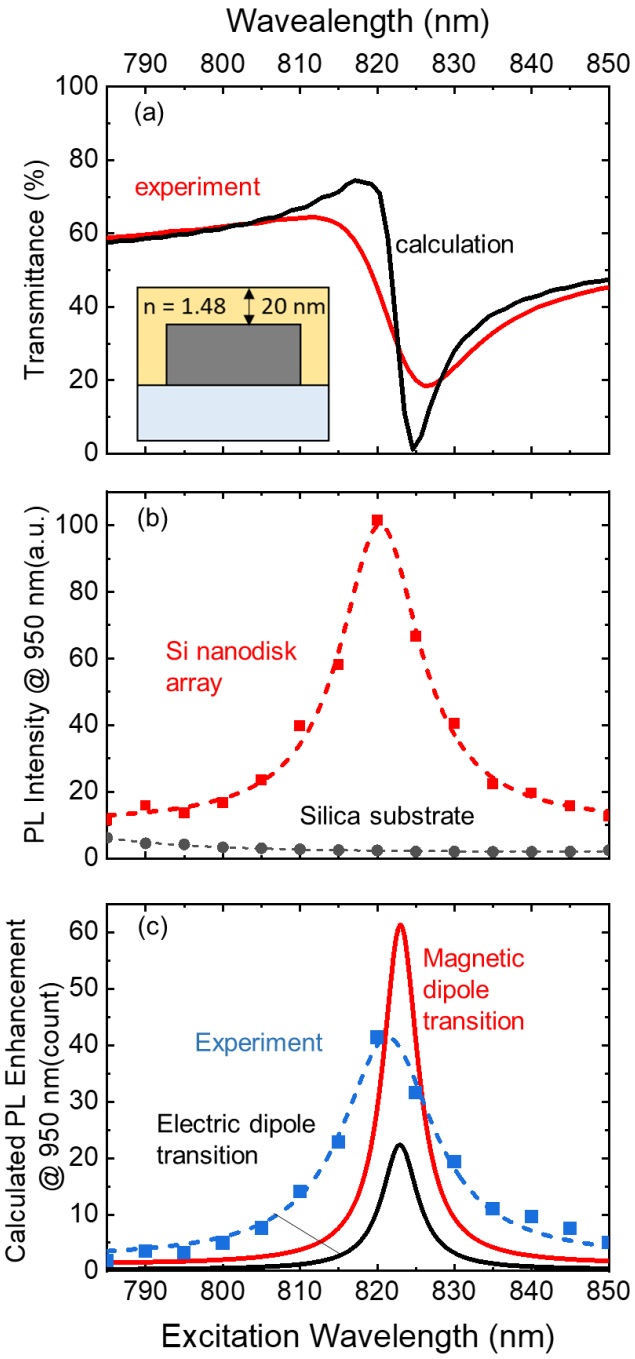

Figure 5-6 *(a) Calculated (black) and measurement (red) transmittance spectra of a silicon nanodisk array (P = 500 nm, D = 450 nm, h = 46 nm). (b) PLE spectra of RuPc(py)$_2$ on the Si nanodisk array (red) and a silica substrate (black). (c) Experimental (blue squire, dash line is Lorentz fitted curve) and calculated (solid curve) PL enhancement factor. The black curve assumes the electric dipole transition, while the red curve assume the magnetic field transition.*

Figure 5-7(a) shows the DPBF absorbance spectra of $RuPc(py)_2$ on a silica substrate excited 825 nm as a reference. The blank result (non-substrate and non-irradiation) is also shown in Figure 5-7(b). From these spectra, we trace the absorbance at 415 nm to obtain the degradation rates. Figure 5-7(c) shows the normalized absorbance as the function of light irradiation time. These degradation rates are almost same. This indicates the singlet oxygen generation rate of $RuPc(py)_2$ is very small in $S_0 \rightarrow T_1$ transition energy range.

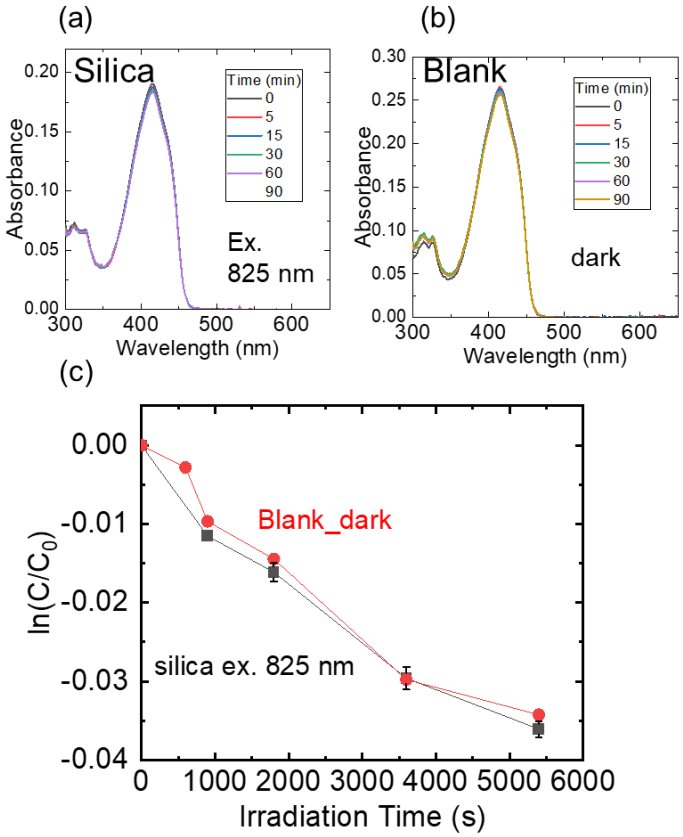

Figure 5-7 *(a,b) Absorbance spectra of DPBF molecules with (a) a $RuPc(py)_2$ functionalized silica substrate exited by 825 nm and (b) blank. (c) Normalized absorbance of DPBF(@ 415 nm) as a function of irradiation time.*

Finally, we demonstrate that the Si nanodisk array with a $RuPc(py)_2$ multilayer works as a photosensitizing metasurface for $^1O_2$ generation via $S_0 \rightarrow T_1$ direct excitation of the

photosensitizer. **Figure 5-8**(a-f) shows the absorbance spectra of DPBF with different excitation wavelength and Figure 5-8(g) shows the logarithm of the absorbance value of DPBF at 415 nm (C) with respect to the initial value (C_0) as a function of light irradiation time. The result obtained for a $RuPc(py)_2$ multilayer formed on a silica substrate and irradiated by 825 nm light is also shown as a reference. We can see that the degradation rate is much larger on a Si nanodisk array than the reference, and it depends on the irradiation wavelength.

Under the assumption that the reaction between DPBF and $^1O_2$ is pseudo-first-order[166], the DPBF degradation rate (k), which is directly related to the $^1O_2$ generation rate, is obtained from $kt = -\ln(C/C_0)$. Figure 5-8(h) shows the experimentally obtained degradation rate as a function of irradiation wavelength, together with the transmittance spectrum of the nanodisk array in DMF. The degradation rate is enhanced at the TD resonance wavelength of the Si nanodisk array. This indicates that the photosensitization activity of $RuPc(py)_2$ is enhanced by the TD resonance of the Si nanodisk array. Compared to the off-resonance wavelength (850 nm), the degradation rate is enhanced by a factor of 2. Considering the fact that the degradation of DPBF at the off-resonance wavelength is mainly due to the self-degradation observed even in dark (gray squares in Figure 5-8(g)), the enhancement factor by light irradiation at the resonance wavelength is much higher although it is difficult to quantitatively estimate the value.

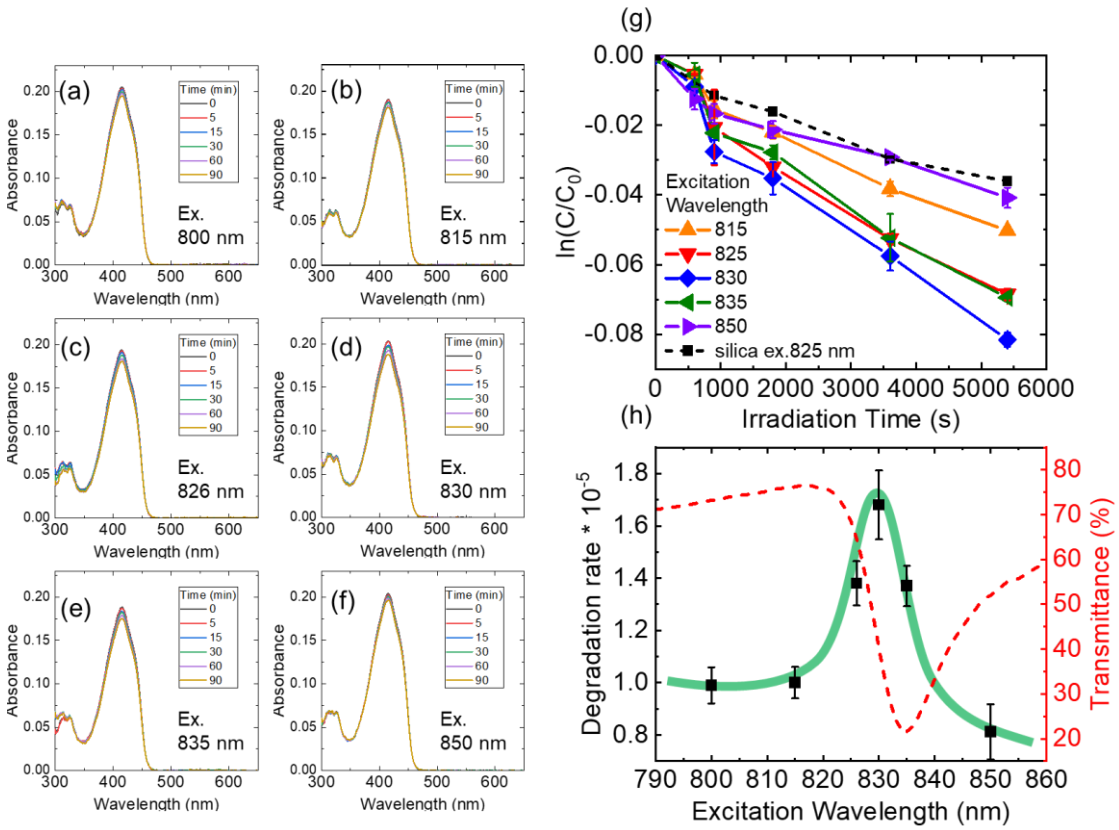

Figure 5-8 *(a-f) Absorbance spectra of DPBF molecules with RuPc(py)$_2$ functionalized Si nanodisk array exited by various wavelengths(800-850 nm) (b) Normalized absorbance of DPBF(@ 415 nm) as a function of irradiation time. (c) DPBF degradation rates as a function of excitation wavelength +(black squires) and a transmittance spectra of the Si nanodisk array in DMF.*

5.3 Conclusion

We developed a new composite metasurface composed of a Si nanodisk array and photosensitizer molecules. In the optimized nanodisk array structure, the rate of the direct $S_0 \rightarrow T_1$ excitation is 41-fold enhanced when the excitation wavelength is at the resonance wavelength of the TD mode of a Si nanodisk array. Finally, we experimentally demonstrated the enhancement of the photochemical reaction by monitoring the degradation of DPBF with the reaction of $^1O_2$ generated via energy transfer from the T_1 state under illumination at resonant and non-resonant

wavelengths of the TD mode. The present result suggests that a composite structure composed of an optical metasurface and photosensitizer molecules can be a new platform to promote a variety of photochemical reactions.

PART II : Optelectronic Device Application Utilizing Toroidal Dipole Resonance

Chapter 6

Toroidal dipole-induced photocurrent enhancement below the band gap

Adapted from Hiroaki Hasebe, et. al., ACS photonics 2022,9,10,3302-3309

Near infrared (NIR) light often defined in the wavelength range of 800 – 2500 nm is transparent in many materials and has been widely used in optical telecommunication[167–170], face recognition[171,172], autonomous driving, gas sensing[173], bio imaging[174–176], etc. Conventional silicon (Si) photodetectors have sensitivity up to ~1100 nm, and longer wavelength ranges are covered by narrow band gap semiconductors such as InGaAs, InP, and Ge. Photodetectors of these narrow band gap semiconductors have been monolithically integrated on a Si device either by a transfer process or direct crystal growth on Si. The integration extends the operation range of Si-based photodetection devices to 1700 nm or to even longer wavelengths.

Recently, new technologies to extend the detection range of Si-based photodetection devices below the band gap have been emerging. The most extensively studied one is utilizing internal photoemission at a Schottky junction between Si and a noble metal nanoantenna[70,177–179]. Incoming light is absorbed by the excitation of localized surface plasmon resonances (LSPRs) in a noble metal nanoantenna. Decaying of surface plasmons to hot electrons having energies larger than the Schottky barrier height, and injection of the hot electrons to Si generates photocurrent. Since the resonance wavelength of LSPRs can be controlled in a wide range by the aspect ratio of a nanoantenna[180], the devices can detect photons up to 1600 nm without using narrow band gap

semiconductors[177]. Similar devices using noble metal nanogratings and surface plasmon polaritons are also developed.[70,178,179] A problem of the Schottky junction approach is the limited choice of noble metal. A metal nanoantenna has to have the LSPR in the NIR range and has to make a good Schottky contact with Si. Practically, Au is a sole choice to satisfy these criteria. However, Au is not a preferable material for a conventional CMOS process.

Another approach to extend the detection range of Si-based devices is utilizing defect-mediated light absorption[71,181–185]. Introduction of defects in crystalline Si forms defect-related states in the band gap that can be used for light absorption in the sub-band gap wavelength range. However, since absorption by defect-related states is very small, it should be enhanced by optical resonances of a photonic structure to achieve reasonable sensitivity of light detection. Several different approaches are proposed to enhance light absorption of Si and similar high-refractive index dielectric materials[111]. For example, narrow-band enhancement of photocurrent is observed below the band gap by utilizing Mie resonances (whispering gallery modes) of a few μm-size Si sphere as a nanoantenna.[71] According to the coupled mode theory, the absorptance of a single mode resonator is limited to 50% (critical coupling)[186,187]. Theoretically, near-unity absorption can be achieved if two modes such as electric dipole (ED) and magnetic dipole (MD) modes degenerate[104,111,187]. In arrays of amorphous Si nanoparticles, the absorptance as large as 0.83 is achieved by properly controlling the overlap of the ED and MD Mie resonances[112]. Degenerate critical coupling is also studied in the case of electric and magnetic quadrupole modes in a Si nanodisk array[110]. Another interesting approach for absorption enhancement is utilizing an anapole state, which is realized by destructive interference between Cartesian ED and toroidal dipole (TD) modes[36,188]. In the anapole state, suppression of far field radiation results in field confinement in a nanostructure, which induces strong enhancement of light absorption[35,164], nonlinear optical responses[76,189,190], Raman scattering[191], photothermal effect[73], stimulated emission (lasing)[20], photocatalytic effects[72], and photoelectrode performance[21].

In this chapter, we exploit TD mode for the photocurrent enhancement in a Si metasurface in the sub-band gap wavelength range. In Chapter 2, we showed that a hexagonal array of low-aspect-ratio Si nanodisks exhibits sharp absorption peaks due to coupling of toroidal dipole of individual nanodisks. Because of the narrow-band absorption enhancement in a transparent range of Si, the metasurface is potentially useful for wavelength-selective photodetection in the sub-band gap wavelength range.

In order to utilize the narrow-band absorption enhancement for the photocurrent enhancement, we produce a low-aspect-ratio Si nanodisk hexagonal array on a thin Si film that acts as a conductive layer. We first demonstrate by numerical simulations that nanodisks strongly confine the electric field of incident light in a Si thin film beneath them, and that the field confinement results in the narrow-band absorption enhancement. Simulations assuming different values of extinction coefficient reveal that, because of the non-radiating nature of the anapole states, the absorptance has the maximum at a very low extinction coefficient range, *e.g.,* ~10^{-3}. This suggests notable photocurrent enhancement in the sub-band gap wavelength range. We experimentally demonstrate that formation of a Si nanodisk hexagonal array on a Si thin film enhances the photocurrent at most 30-fold at the wavelength of the absorption enhancement peaks, and that the peak wavelengths can be controlled by the Si thin film thickness. We also show that the produced device is potentially useful as a current-detection-type refractive index sensor because of the narrow photocurrent peaks.

6.1 Numerical Simulations

6.1.1 Structures and Parameters

We first calculate optical responses of Si nanodisk hexagonal arrays schematically shown in **Figure 6-1** by finite-difference time domain (FDTD) simulation. The substrate is silica and a hexagonal array of Si nanodisks is formed on a flat Si thin film that acts as a conductive layer for

the detection of photocurrent. The diameter (D) and height (h) of nanodisks are 700 and 50 nm, respectively, and the pitch (P) is 750 nm. The thickness of a Si film (t) is changed. First, we use fixed values for the refractive index (n = 3.5) and the extinction coefficient ($\kappa = 10^{-3}$) since the dispersion of the refractive index of Si is very small in the wavelength range.

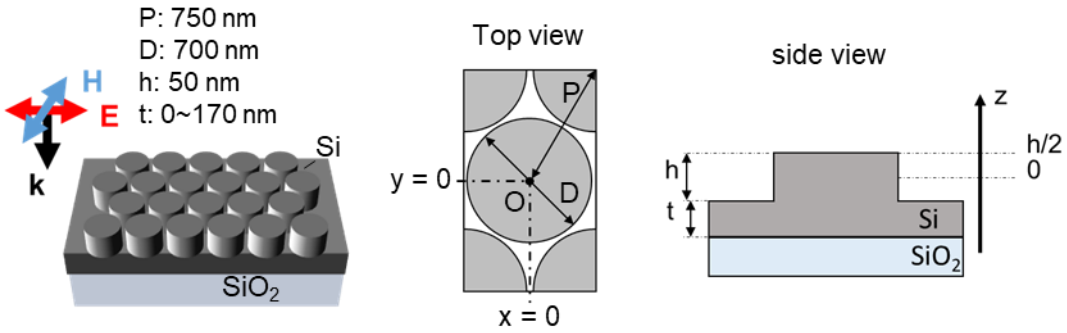

Figure 6-1 *Schematic image of Si nanodisk arrays for a photocurrent enhancement. The period (P), diameter (D), and height (h) are fixed to 750 nm, 700 nm, and 50 nm, respectively. The thickness of Si film beneath nanodisks is vary from 0 to 170 nm.*

6.1.2 Mode Assignment

First, we fix the thickness of a Si film to 110 nm. We calculate the transmittance (T) and the reflectance (R) under normal incidence and obtain the absorptance (A =1-T-R) in the wavelength range from 1000 nm to 1800 nm. **Figure 6-2**(a) shows the calculated transmittance and absorptance spectra. The reflectance spectrum is shown in Figure 6-2(b). In the transmittance spectrum, three sharp dips are seen around 1602, 1137, and 1050 nm. At the 1602 and 1050 nm dips, strong absorption peaks appear, despite the very small extinction coefficient ($\kappa = 10^{-3}$). On the other hand, at the 1137 nm transmittance dip, the absorption peak is very small. This suggests that the origin of the 1137 nm transmittance dip is different from others.

Figure 6-2(c-e) shows the electric field distributions ($|\boldsymbol{E}|/|\boldsymbol{E_0}|$) and Figure 6-2(f-h) shows the magnetic field distributions ($|\boldsymbol{H}|/|\boldsymbol{H_0}|$), where $|\boldsymbol{E_0}|$ and $|\boldsymbol{H_0}|$ are the electric and magnetic field intensity of incident light, at z = 0 (xy-plane), x = 0 (yz-plane), and y = 0 (zx-plane) at 1602,

1137 and 1050 nm, respectively. Si regions are surrounded by thick broken lines. At 1602 nm (Figure 6-2(c,f)), we can see symmetric current loops characteristic of the TD mode. The strong absorption at the wavelength is thus due to the sub-radiant TD resonance[164]. We refer the peak from a conventional nomenclature to the TE_{110} mode, where the subscripts denote the number of nodes across azimuth, radial, and *z* directions. At this resonance, the electric field is strongly confined in the Si region below a Si nanodisk, despite the small disk height compared to the Si film thickness (h/t =0.46). This strong confinement of the electric field in the Si region brings about the strong light absorption. The maximum enhancement factor of the electric field reaches 10.3. The absorption peak at 1050 nm is assigned to the radial higher-order TD mode.[76,137] From the field distribution in Figure 6-2(e), we refer the high-order TD mode to the TE_{120} mode. The field is more tightly confined than the TE_{110} mode, and the enhancement factor reaches 17.3.

The origin of the transmittance dip at 1137 nm is different from the others. This is a Rayleigh anomaly arising from the formation of the periodic structure.[96,98] The electric field is enhanced mainly in the region between Si nanodisks (Figure 6-2(d)). As a result, the absorption enhancement is marginal, despite the deep transmittance dip (Figure 6-2(a)). The mode is assigned to the TM_{110} mode from the magnetic field distribution (Figure 6-2(g)).

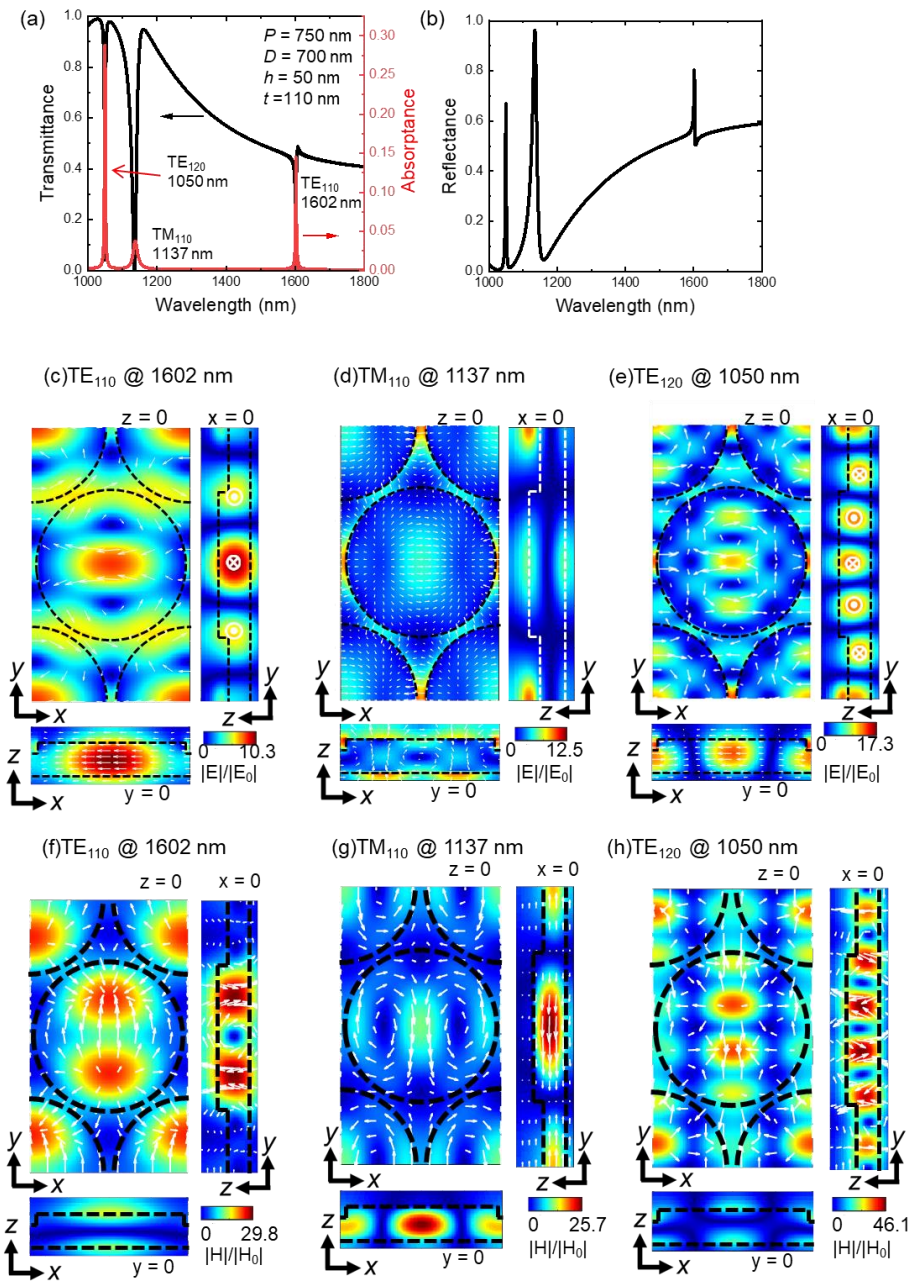

Figure 6-2 *(a) Transmittance, absorptance and (b)reflectance spectra of the metasurface with P = 750 nm, D = 700nm, h = 50 nm, and t = 110 nm. (c-e) Electric field and (f-h) magnetic field distributions of (c,f)TE_{110} (@ 1602 nm), (d,g)TM_{110} (@ 1137 nm), and (e,h)TE_{120} (@ 1050 nm) modes.*

The resonance wavelengths of these modes can be controlled by the structural parameters of nanodisks, *i.e.*, *P*, *D* and *h* [164], and by the thickness of a Si film (*t*). In particular, it is very sensitive to a Si film thickness. **Figure 6-3** shows the contour plot of the absorptance spectra of Si nanodisk arrays formed on different thickness Si films. The structure of the nanodisk array is the same as that shown in Figure 6-1. We can see that the resonance modes show significant red-shift with increasing the Si film thickness. The sensitiveness of the resonance wavelength on the Si film thickness arises from the fact that the electric field is predominantly distributed in the region of a Si film below the nanodisks due to the very small nanodisk height.

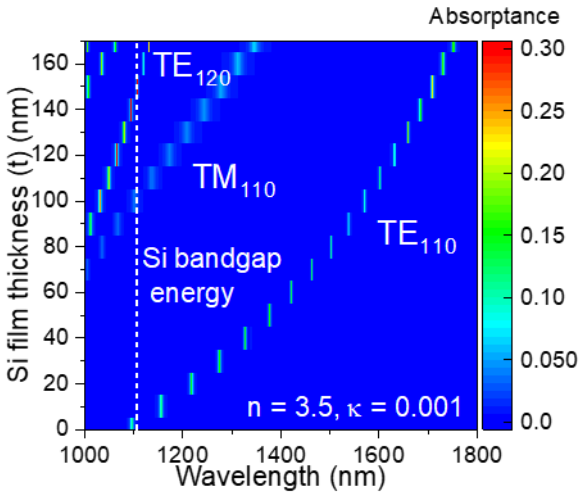

Figure 6-3 *Absorptance colormap with different t. P, D, and h are fixed (P = 750 nm, D = 700 nm, h = 50 nm).*

6.1.3 Absorption with Different Extinction Coefficient

We use poly-Si films produced by annealing sputter-deposited amorphous Si for the preparation of nanodisk arrays. The poly-Si films are defective and there is defect-related weak absorption below the band gap. Typically, the extinction coefficient of intrinsic poly-Si in the NIR range is ~10^{-2}. [184,185,192] Although it is better to use the extinction coefficient value determined by ellipsometry for numerical simulations, it is too low for the accurate measurement for thin films. Therefore, we simulate absorptance spectra by changing the extinction coefficient in a wide

range (10^{-1} – 10^{-4}). **Figure 6-4**(a) shows the results. The peak wavelengths are not affected because of the fixed n, while the intensity and the width of the modes change depending on κ. To obtain the absorptance values and FWHMs which stem from each mode, we subtracted the background by the following procedure and extracted the peak absorptance values and the FWHMs. As schematically shown in the inset of **Figure 6-5**(a), we consider the background absorptance comes from the effective medium layer whose thickness is same as the height of nanodisks. The average permittivity of an effective medium layer ($\varepsilon_{r,eff}$) is expressed by the Bruggeman effective medium approximation,

$$f_{disk}\frac{\varepsilon_{r,disk}-\varepsilon_{r,eff}}{\varepsilon_{r,disk}+2\varepsilon_{r,eff}}+(1-f_{disk})\frac{\varepsilon_{r,Air}-\varepsilon_{r,eff}}{\varepsilon_{r,Air}+2\varepsilon_{r,eff}}=0\,, \tag{43}$$

where f_{disk} is the volume fraction of nanodisks and $\varepsilon_{r,Air}$ and $\varepsilon_{r,disk}$ are the permittivity of air (n =1) and Si (n =3.5), respectively. The red curve in Figure 6-5(a) is the calculated background spectrum. Figure 6-5(b) is the absorption spectrum after subtracting the background. By fitting the peaks in Figure 6-5(b) by Lorentz functions, the peak absorptance values and the FWHM are extracted.

Figure 6-4(b,c) shows the peak absorptance and the full-width half maximum (FWHM) of each mode as a function of κ, respectively. Interestingly, the absorptance does not increase monotonously with κ, but has the maximum at a certain κ. The extinction coefficient at the maximum absorptance for the TM_{110} mode is relatively large ($\kappa = 3.0 \times 10^{-2}$), while those of the TE_{110} and TE_{120} modes are very small, *i.e.*, 1.5×10^{-3} and 4.0×10^{-3}, respectively. These behaviors can be explained by the coupled mode theory, in which the maximum absorptance is achieved when the material loss is equal to the radiation loss[187]. The radiation loss of the TM_{110} mode is relatively large as can be seen in the large FWHM at the low extinction coefficient range (*e.g.*, $\kappa = 1.0 \times 10^{-4}$) in Figure 6-4(c). The large radiation loss results in the absorptance maximum at relatively large κ ($=3.0 \times 10^{-2}$). On the other hand, the radiation loss of the TE_{110} and TE_{120} modes is very small as can be seen in the extremely small FWHMs at the low extinction

coefficient range in Figure 6-4(c). This brings the absorptance maximum to the very small extinction coefficient range (κ = 1.5 × 10^{-3} and 4.0 × 10^{-3}, respectively). We quantitatively estimate the extinction coefficient at the maximum absorptance by the coupled mode theory. According to the temporal coupled mode theory, absorption by a resonance mode is maximized when $Q_r = Q_{nr}$, where $Q_r(Q_{nr})$ is the total radiative (nonradiative) quality factor[104,193]. Therefore, if Q_r is known, the optimum extinction coefficient to maximize the absorptance can be estimated. **Figure 6-6**(a) shows calculated transmittance spectrum of a loss-less (κ = 0) nanodisk array (P =750 nm, D =700 nm, h =50 nm, t =110 nm, n =3.5, κ =0). The peaks can be fitted by the classical Fano formula[139,140]

$$T(\omega) = T_0 + \frac{A_0\left[q+\frac{2(\omega-\omega_0)}{\tau}\right]^2}{1+\left[\frac{2(\omega-\omega_0)}{\tau}\right]^2}, \quad (44)$$

where, ω_0 is the resonant frequency, τ is the resonance line width, T_0 is the transmission offset, A_0 is the continuum discrete coupling constant, and q is the asymmetric parameter. Q_r is given by ω_0/τ. The values of Q_r for TE_{110}, TM_{110}, and TE_{120} modes are shown in Figure 6-6(a). Q_{nr} is defined as $Q_{nr} = \frac{n}{2\kappa F}$, where F is the ratio of the electric field energy in the absorptive material volume (V_{abs}) and in the cavity volume (V) [193]. Since $V_{abs} \approx V$ in a Si nanodisk hexagonal array, $Q_{nr} \approx \frac{n}{2\kappa}$ (black curve in Figure 6-6(b)). The intersection between Q_r and Q_{nr} gives optimum values of κ for maximum absorptance. They are κ = 1.65 × 10^{-3}, 2.32 × 10^{-2} and 3.74 × 10^{-3} for TE_{110}, TM_{110}, and TE_{120} modes, respectively. These values are in good agreement with the data in Figure 6-4(b). These results indicate that very narrow absorption bands can be realized in the almost transparent wavelength range of Si by utilizing the TD resonances (TE_{110} and TE_{120} modes).

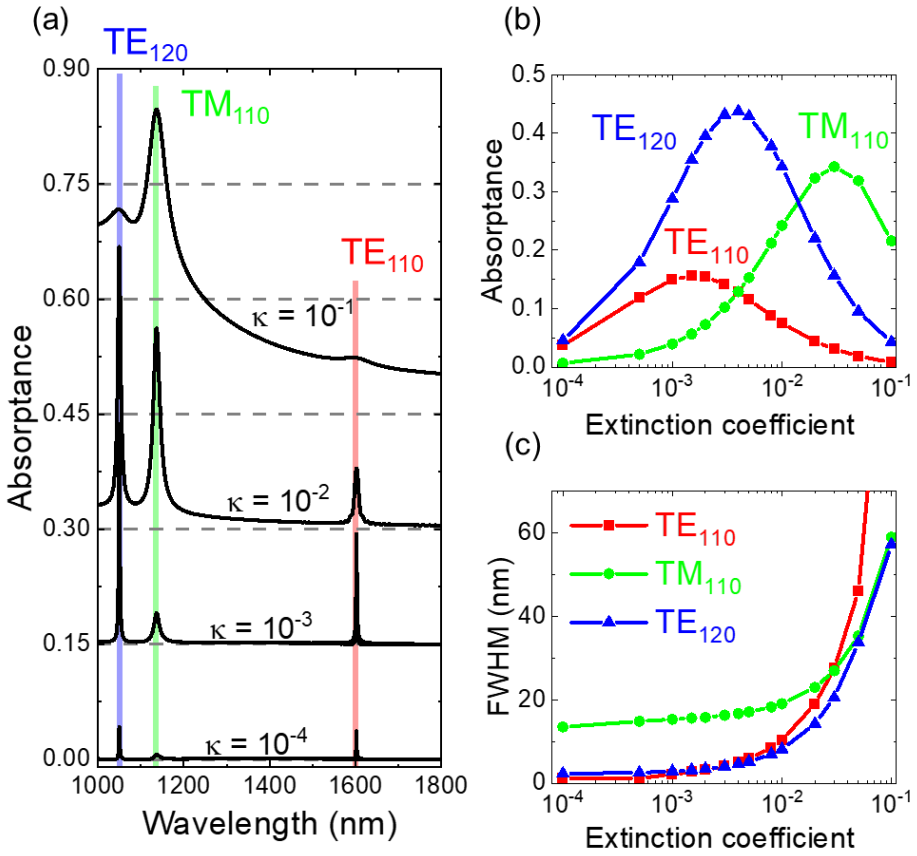

Figure 6-4 *(a) Absorptance spectra with different extinction coefficient ($\kappa = 10^{-4}$~10^{-1}). (b) Absorptance peak value and (c)FWHM of each modes as a function of extinction coefficient obtained after subtracting the broad background absorption.*

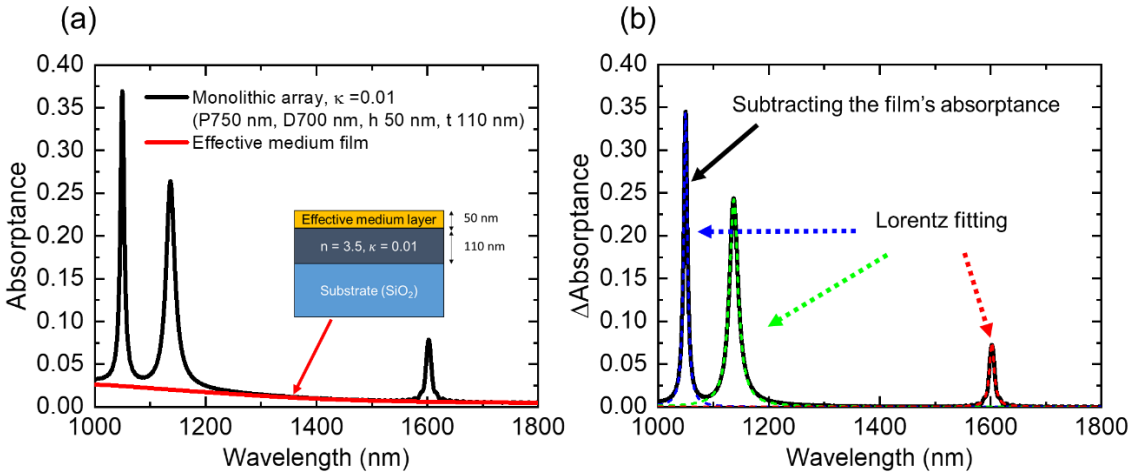

Figure 6-5 *(a) Calculated absorptance spectrum of a Si nanodisk hexagonal array (P =750 nm, D=700 nm, h =50 nm, t =110 nm, n =3.5,κ =10^{-2} : black curve) and the background spectrum obtained by the effective medium approximation (red curve). (b) Absorptance spectrum after subtracting the background (black curve), and results of the fitting by the Lorentz functions (color dashed curves).*

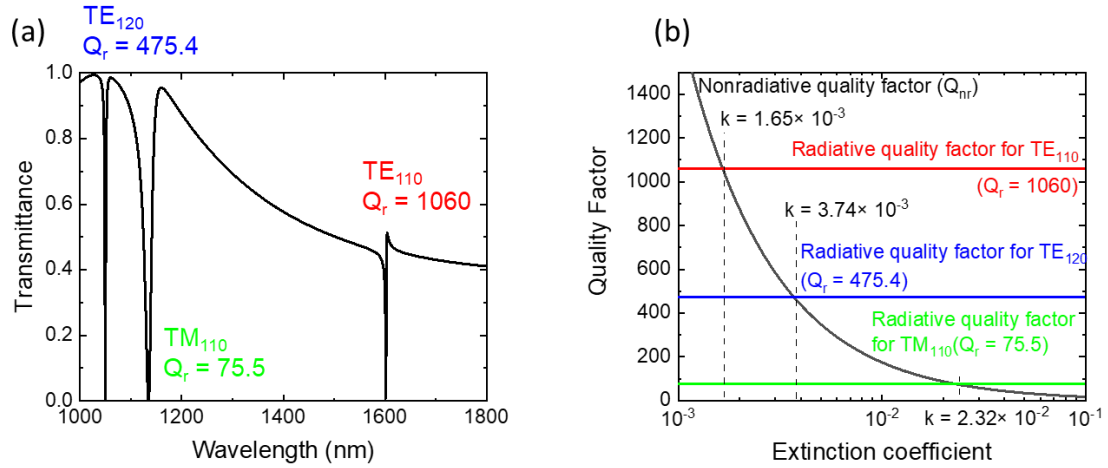

Figure 6-6 *(a) Calculated transmittance spectrum of a Si nanodisk hexagonal array (P = 750 nm, D =700 nm, h =50 nm, t =110 nm, n =3.5,κ =0). (b) Radiative (Q_r) and nonradiative (Q_{nr}) quality factors as a function of extinction coefficient.*

The relation between the peak absorptance and the extinction coefficient depends strongly on the structural parameter of the nanodisk array. As an example, we show the data when the Si film thickness (t) is 170 nm in **Figure 6-7**; other parameters are the same as those in Figure 6-4. In that case, the absorptance peak of the TE_{120} mode shifts to very small extinction coefficient range (κ_{max} : ~2.0 × 10^{-4}), while that of the TE_{110} mode is not strongly affected (κ_{max}: ~2.0 × 10^{-3}). The maximum absorptance of the TE_{110} mode increases from 0.15 in Figure 6-4(b) (t =110 nm) to 0.33, while the FWHM at the absorptance maxima is kept small. Therefore, the developed structure can be tuned to make the absorptance the largest for a desired extinction coefficient.

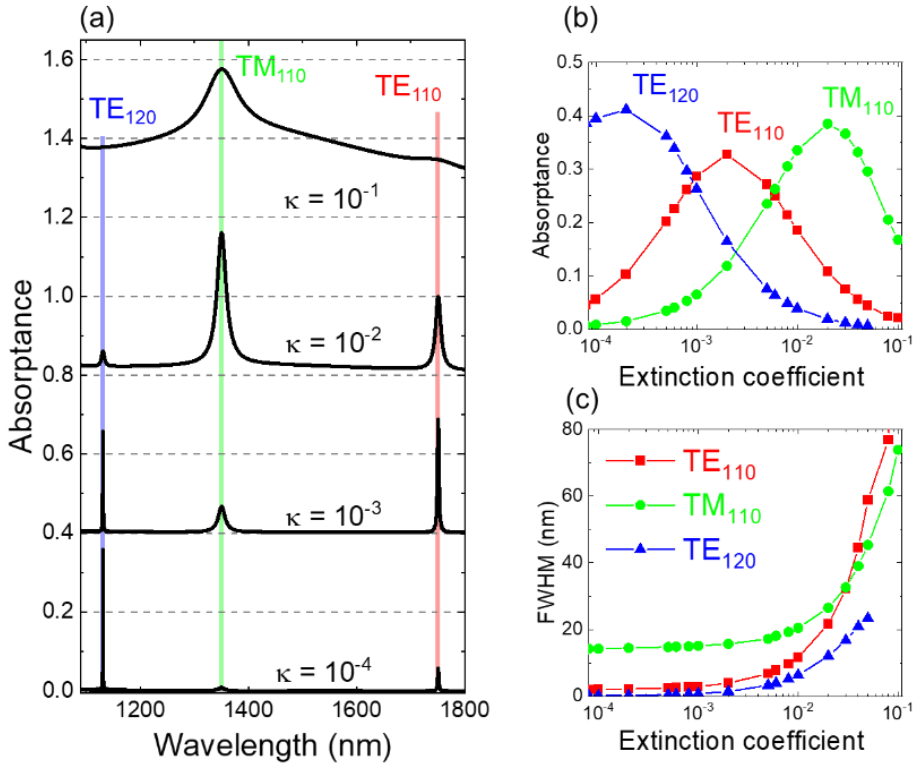

Figure 6-7*(a) Calculated absorptance spectra of Si nanodisk hexagonal arrays (P =750 nm, D =700 nm, h =50 nm and t =170 nm). The extinction coefficient is changed from 10-1 to 10-4, while the refractive index is fixed to 3.5. (b) Absorptance value at the maximum of absorptance peaks as a function of extinction coefficient. (c) FWHM of absorptance peaks as a function of extinction coefficient.*

6.2 Experimental Methods

In this work, we use PS sphere with 750 nm in diameter and stop Si etching in the middle to make a Si film beneath Si nanodisk arrays. **Figure 6-8** (a,b) shows a AFM topo graph and the height profile along the black line in (a), and Figure 6-8(c) shows a SEM image of a Si nanodisk array. The period, diameter and height are 710 nm, 550 nm, and 30 nm, respectively. We fixed these parameters and change only the thickness of a Si film (t =20, 50, 70, 100 and 150 nm). On a nanodisk array, aluminum (Al) stripe electrodes are formed for the photocurrent measurement. The distance between the electrodes is 200 μm. The schematic illustration of photocurrent measurements is shown in Figure 6-8(d). A nanodisk array was illuminated from the normal through an objective lens (N.A. =0.055). The light source was a supercontinuum laser (NKT Photonics, SuperK EVO) monochronized by an acousto-optic tunable filter (NKT Photonics, SuperK SELECT NIR 1 for 800 to 1100 nm and SUPERK SELECT IR for 1100 to 1700 nm). Current was measured with a source measurement unit (Keithley 236) under the applied bias of 100 V. Photocurrent measurements were carried out in vacuum.

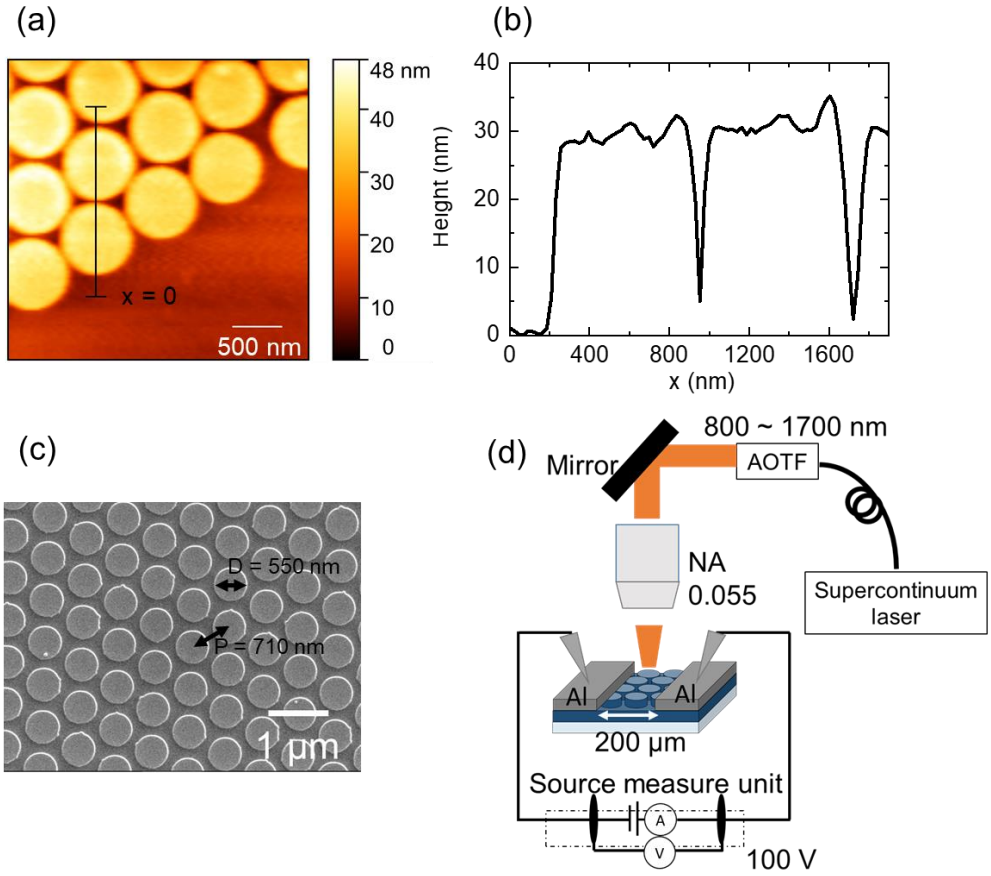

Figure 6-8 *(a) AFM topo graph. (b) The height profile of fabricated nanodisk array along the line in (a). (c)SEM image. (d)Set up for photocurrent measurement.*

6.3 Results and Discussion

Figure 6-9(a) shows the experimental and calculated transmittance spectra of the Si nanodisk array with P = 710 nm, D = 550 nm, h = 30 nm, t = 150 nm n = 3.1, and κ=10^{-2}. The resonance positions of the experimental result are in good agreement to calculated ones. We can see transmittance dips predicted by the simulations (TE_{110}, TM_{110}, and TE_{120} modes), although the width is larger than the simulations. The broadening is mainly due to partial disorder of the periodic structure, which is difficult to avoid in the nanosphere lithography process. The important fact is that, although broadened, clear transmittance dips appear in the sub-band gap wavelength range. Figure 6-9(b) shows the responsivity and calculated absorptance spectra. Although the

responsivity peaks are broader than the calculated absorptance peaks, the peak wavelengths agree very well. This indicates that the photocurrent peaks arise from the absorption enhancement by the resonant modes and resultant increase of photogenerated carriers even below Si bandgap energy. The photocurrent spectra are independent of the polarization of incident light because of the symmetric structure(Figure 6-9(c)).

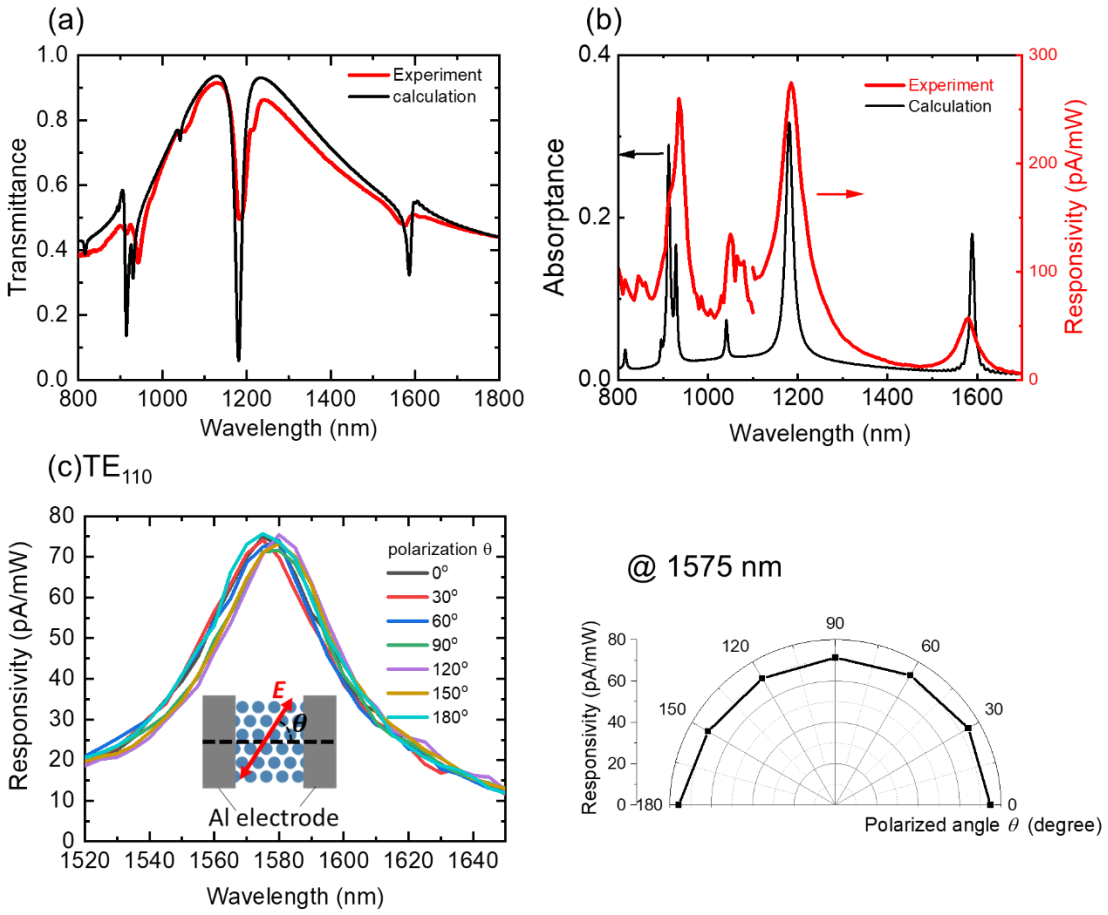

Figure 6-9 *(a) Calculated (black curve, P = 710 nm, D = 550 nm, h = 30 nm, n = 3.1, κ =10^{-2}) and Measured (red curve) transmittance spectra. (b) Calculated absorptance (black curve) and measured photocurrent (red curve) spectra. (c) Measured photocurrent spectra around the TE_{110} resonance for a Si nanodisk hexagonal array (P = 710 nm, D = 550 nm, h = 30 nm, t = 150 nm). The polarization direction of incident light is changed. Polar plot of the responsivity at 1575 nm is also shown.*

Figure 6-10(a-e) shows the transmittance and photocurrent (responsivity) spectra of the devices with t =20, 50, 70, 100 and 150 nm, respectively. The photocurrent spectra of flat Si thin films with the thickness of $t + h$ (= t + 30 nm) are also shown in each spectrum. The resonance wavelengths are well controlled by the Si film thickness from up to below Si bandgap energy.

In Figure 6-10(a-e), at the wavelength of transmittance dips, we can clearly see photocurrent peaks. Figure 6-10(f-j) shows photocurrent enhancement factor spectra obtained by dividing photocurrent of a Si nanodisk hexagonal array with that of a flat Si film in Figure 6-10(a-e), respectively. We can more clearly see photocurrent enhancement by the resonant modes. In the sub-band gap range of Si, the enhancement factor reaches ~30 (1300 nm in Figure 6-10(i)). Even at longer wavelengths, *e.g.*, 1575 nm in Figure 6-10(j), substantial photocurrent enhancement (~6) is observed. The FWHM of the peaks are around 30~60 nm, which is narrower than that reported in Si-based photodetectors using LSPRs of metal nanostructures[70,178].

The narrow polarization-independent photocurrent peaks of the nanodisk arrays can be used for a current-detection type refractive index sensor operating in the NIR range. In contrast to conventional dielectric-metasurface-based refractive index sensors that monitor the intensity of the transmitted or reflected light by external NIR photodetectors [133,194–197], our device does not require the NIR photodetector. This may reduce the size and cost of the system, and potentially improve the sensitivity, especially in the wavelength, where a conventional Si photodetector cannot be used. In order to simulate the effect of refractive index change, we place a thin dielectric layer (30 nm in thickness) with the refractive index of 1.0 (vacuum) to 1.6 on top of a Si nanodisk array and calculate the absorptance spectra. The structural parameters are P =710 nm, D =550 nm, h =30 nm, and t =100 nm. The refractive index of Si is set to 3.1. **Figure 6-11**(a) shows the calculated absorption spectra around the TE_{110} mode. The peak shifts to longer wavelength with increasing the refractive index. The sensitivity defined by $\Delta\lambda/\Delta n$ is approximately 29.6 nm/RIU. The peak absorptance and the FWHM change only slightly. The slight decrease of the FWHM,

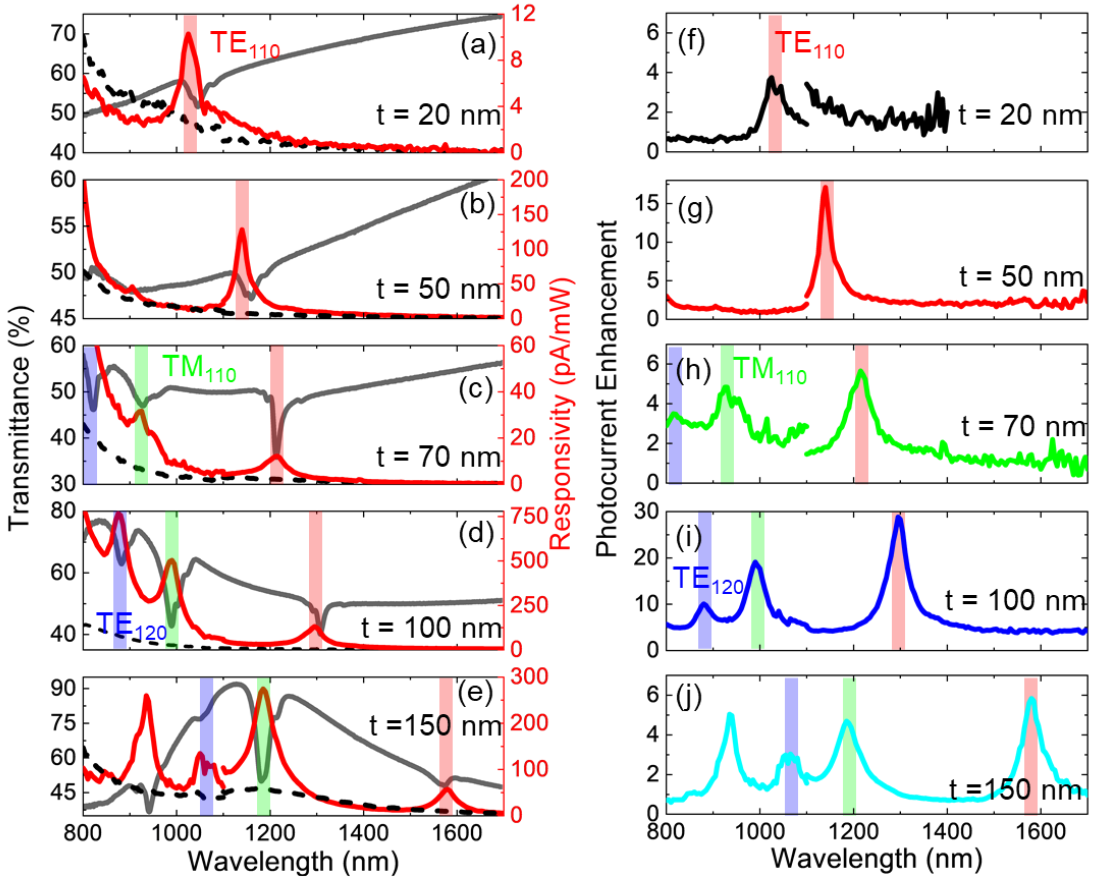

Figure 6-10 *(a-e) Transmittance (gray line) and photocurrent (responsivity) (red) spectra of samples with different Si film thicknesses (t); (a) 20, (b) 50, (c) 70, (d) 100, and (e) 150 nm. Other structural parameters are fixed (P = 710 nm, D = 550 nm, and h = 30 nm). Black broken curves are responsivity of flat Si films with the thicknesses of t + h (=t + 30 nm). (f-j) Photocurrent enhancement factor spectra obtained by dividing photocurrent of a Si nanodisk hexagonal array with that of a flat Si film in (c)–(g), respectively.*

i.e., from 2.6 to 2.1 nm, is due to the decrease of the radiation loss caused by the reduced refractive index contrast between the substrate and the surrounding medium.

In order to experimentally prove detection of a refractive index change by the photocurrent, we deposit a 30 nm thick polystyrene film (n =~1.59) on top of the device in Figure 6-10(d) by spin coating and measured the transmittance and photocurrent spectra. Figure 6-11(b) shows the results around the TE_{110} mode. Both the transmittance dip and the photocurrent peak

shift to longer wavelength by the polystyrene deposition. The photocurrent peak shifts 13 nm, which is close to the expected value (17.8 nm). Therefore, the TD resonances of a Si nanodisk array can be used as a current-detection type refractive index sensor.

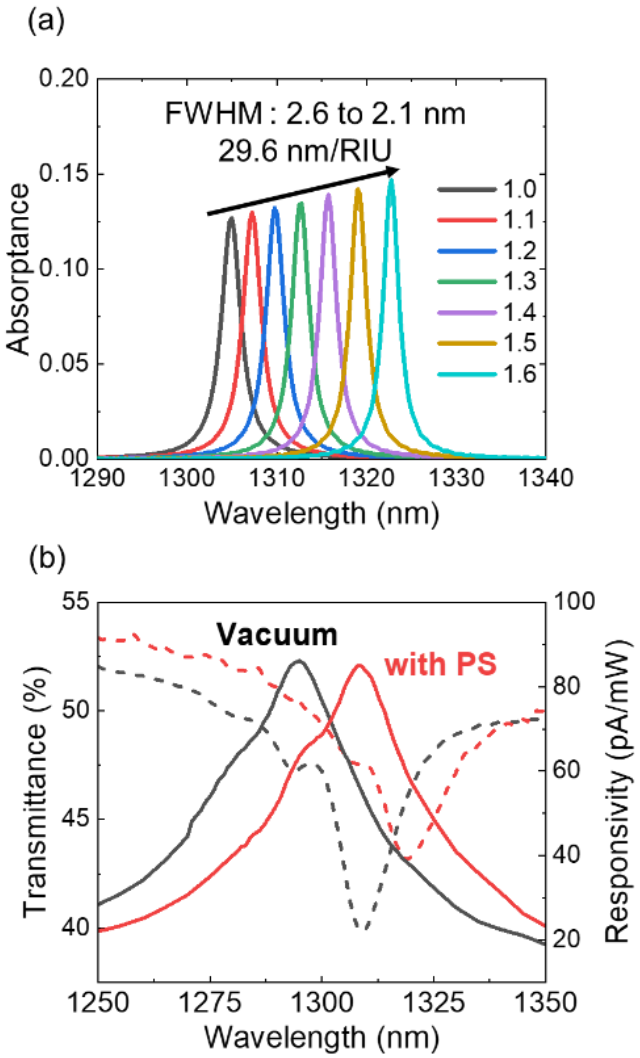

Figure 6-11 *(a) Calculated absorption spectra of Si nanodisk hexagonal arrays (P = 710 nm, D = 550 nm, h = 30 nm, and t = 100 nm, n = 3.1, κ = 10^{-3}). A thin dielectric layer (30 nm in thickness) with the refractive index of 1.0 (vacuum) to 1.6 is placed on the top. (b) Measured transmittance (broken curves) and photocurrent spectra (solid curves) of a Si nanodisk hexagonal array with (red curves) and without a 30 nm thick polystyrene film (black curves).*

6.4 Conclusion

The hexagonal array of Si nanodisks formed on a Si thin film possesses anapole states that strongly enhance light absorption in a sub-band gap wavelength region where the extinction coefficient is very small. Because of the non-radiating nature of the anapole state and the small material loss, the absorption peaks are very narrow. We have demonstrated that the narrow-band absorption enhancement can be utilized to enhance the photocurrent of a Si thin film in the sub-band gap wavelength range. The nanodisk array can thus be used as a narrow-band photodetector operating below the band gap. We experimentally showed that the resonance wavelength can be controlled in a wide wavelength range and the photocurrent is at maximum ~30-fold enhanced at 1300 nm. We showed that the photocurrent peaks shift depending on the refractive index of surrounding medium, and thus the device can be used as a current-detection type refractive index sensor operating in the sub-band gap wavelength range of Si.

Chapter 7

Summary and Outlook

Throughout this thesis, we have developed toroidal dipole metasurface which are composed of hexagonal arraigned thin Si nanodisks and demonstrated their application utilizing their strong electromagnetic enhancements from two aspects: using confined electromagnetic fields for other materials or self-absorption enhancement. We summarize their achievements and outlook in this chapter.

In Chapter 2, we proposed a metasurface composed of two-dimensional hexagonal array of very thin (height: 20 ~ 50 nm, diameter: 300 ~ 450 nm) Si nanodisk supporting toroidal dipole mode. We revealed that the metasurface we proposed supports intra- and inter-nanodisk toroidal dipole moments, which results in a high Q resonance and a strong electromagnetic field confinement inside the structures. We find strong absorption enhancement (120-fold) compared to a same thickness Si flat film even though the Si volume is 26% reduced. Additionally, the enhanced magnetic field by coupled TD resonance leaks outside the structure, which can be utilized for magnetic-light-matter interaction enhancement. Then, we fabricated the structures over cm^2 area with a colloidal lithography method following the design of the structure by numerical simulations. We tuned the toroidal dipole resonances by changing both diameters and heights with a Si deposition time and a polystyrene musk etching time. We demonstrated the electromagnetic field enhancement by the absorption measurements experimentally.

In Chapter 3, we studied the coupling effect between dipole emitters and a toroidal dipole resonance of a silicon hexagonal array. We conducted lifetime and angle resolved PL measurements of Si quantum dots placed on a Si metasurface. We observed that the photoluminescence was specially modified which results in the collection efficiency enhancement. This is useful for low N.A. optics. However, the nonradiative decay rate was also enhanced due to the loss of Si, which limits the PL enhancement. The nonradiative enhancement can be

suppressed if we use low-loss materials (*e.g.* single crystalline Si) or emitters that have photoluminescence at longer wavelengths. Additionally, if we tune other resonances to the excitation wavelength, we can obtain further PL enhancements.

In Chapter 4 and Chapter 5, we tried to enhance the S-T direct excitation of Ru complex by a magnetic field enhanced by a toroidal dipole resonance and to apply it for a new photochemical platform. We showed about 40-fold S-T absorption enhancement from PLE measurements and promoting photosensitizing activity with a singlet oxygen generation as a model reaction in the S-T transition energy range which is under ~400 meV below the S-S transition. We revealed the magnetic field enhancement contributed to these enhancements compared to the calculation results. However, the volume of enhanced magnetic field is small (a few hundred nm× the area of excitation light) although it is much larger than molecules. We have to consider the structures to expand the enhanced magnetic field for commercial applications. Additionally, we have not discussed direct evidence that shows the triplet state excitation directly. If we conduct a transient absorption spectroscopy[198] or a time-resolved electron paramagnetic resonance study[199] and obtain the evidence, we can propose this metasurface for further photochemical applications.

In Chapter 6, we experimentally showed that the resonance wavelength can be controlled in a wide wavelength range and the photocurrent was at maximum ~30-fold enhanced at 1300 nm. We revealed that we can obtain high absorption to control the quality factor of the resonances even though the extinction coefficient is very small. from the coupling mode theory. However, the absorption was limited to 50% because we utilized only a toroidal dipole resonance. We can overcome this limit and obtain perfect absorption introducing a backreflector and coupling a toroidal dipole resonance with its mirror dipole mode[200]. Additionally, we also showed that the photocurrent peaks shift depending on the refractive index of surrounding medium. Thus the device can be used as a current-detection type refractive index sensor such as biosensor operating in the sub-band gap wavelength range of Si.

Reference

(1) Yu, N.; Capasso, F. Flat Optics with Designer Metasurfaces. *Nature Materials*. 2014, pp 139–150. https://doi.org/10.1038/nmat3839.

(2) Novotny, L.; Bharadwaj, P.; Deutsch, B. Optical Antennas. *Adv. Opt. Photonics, Vol. 1, Issue 3, pp. 438-483* **2009**, *1* (3), 438–483. https://doi.org/10.1364/AOP.1.000438.

(3) Mie, G. Articles on the Optical Characteristics of Turbid Tubes, Especially Colloidal Metal Solutions. *Ann. Phys.* **1908**, *25* (25), 377–445.

(4) Liang, Z.; Sun, J.; Jiang, Y.; Jiang, L.; Chen, X. Plasmonic Enhanced Optoelectronic Devices. *Plasmonics*. Springer February 14, 2014, pp 859–866. https://doi.org/10.1007/s11468-014-9682-7.

(5) Soukoulis, C. M.; Wegener, M. Past Achievements and Future Challenges in the Development of Three-Dimensional Photonic Metamaterials. *Nature Photonics*. 2011, pp 523–530. https://doi.org/10.1038/nphoton.2011.154.

(6) Enkrich, C.; Wegener, M.; Linden, S.; Burger, S.; Zschiedrich, L.; Schmidt, F.; Zhou, J. F.; Koschny, T.; Soukoulis, C. M. Magnetic Metamaterials at Telecommunication and Visible Frequencies. *Phys. Rev. Lett.* **2005**, *95* (20), 203901. https://doi.org/10.1103/PhysRevLett.95.203901.

(7) Linden, S.; Enkrich, C.; Wegener, M.; Zhou, J.; Koschny, T.; Soukoulis, C. M. Magnetic Response of Metamaterials at 100 Terahertz. *Science (80-.).* **2004**, *306* (5700), 1351–1353. https://doi.org/10.1126/science.1105371.

(8) Kuznetsov, A. I.; Miroshnichenko, A. E.; Fu, Y. H.; Zhang, J.; Lukyanchukl, B. Magnetic Light. *Sci. Rep.* **2012**, *2*. https://doi.org/10.1038/srep00492.

(9) Kuznetsov, A. I.; Miroshnichenko, A. E.; Brongersma, M. L.; Kivshar, Y. S.; Luk'yanchuk, B. Optically Resonant Dielectric Nanostructures. *Science*. 2016. https://doi.org/10.1126/science.aag2472.

(10) Murai, S.; Abujetas, D. R.; Castellanos, G. W.; Sánchez-Gil, J. A.; Zhang, F.; Rivas, J. G. Bound States in the Continuum in the Visible Emerging from Out-of-Plane Magnetic Dipoles. *ACS Photonics* **2020**, *7* (8), 2204–2210. https://doi.org/10.1021/ACSPHOTONICS.0C00723.

(11) Hinamoto, T.; Hotta, S.; Sugimoto, H.; Fujii, M. Colloidal Solutions of Silicon Nanospheres toward All-Dielectric Optical Metafluids. *Nano Lett.* **2020**, *20* (10), 7737–7743. https://doi.org/10.1021/ACS.NANOLETT.0C03295/SUPPL_FILE/NL0C03295_SI_001.PDF.

(12) Papasimakis, N.; Fedotov, V. A.; Savinov, V.; Raybould, T. A.; Zheludev, N. I. Electromagnetic Toroidal Excitations in Matter and Free Space. *Nat. Mater.* **2016**, *15* (3), 263–271. https://doi.org/10.1038/nmat4563.

(13) Y.B Zeldyich. Electromagnetic Interaction with Parity Violation. *J. Exp. Theor. Phys* **1957**, *33*, 1531–1533.

(14) Flambaum, V. V.; Murray, D. W. Anapole Moment and Nucleon Weak Interactions. *Phys. Rev. C* **1997**, *56* (3), 1641. https://doi.org/10.1103/PhysRevC.56.1641.

(15) Cabral-Rosetti, L. G.; Mondragón, M.; Reyes-Pérez, E. Anapole Moment of the Lightest Neutralino in the CMSSM. *Nucl. Phys. B* **2016**, *907*, 1–17. https://doi.org/10.1016/j.nuclphysb.2016.03.025.

(16) Ho, C. M.; Scherrer, R. J. Anapole Dark Matter. *Phys. Lett. B* **2013**, *722*, 341–346. https://doi.org/10.1016/j.physletb.2013.04.039.

(17) Spaldin, N. A.; Fiebig, M.; Mostovoy, M. The Toroidal Moment in Condensed-Matter

Physics and Its Relation to the Magnetoelectric Effect. *J. Physics-Condensed Matter* **2008**, *20* (43), 15. https://doi.org/10.1088/0953-8984/20/43/434203.

(18) Hayami, S.; Yatsushiro, M.; Yanagi, Y.; Kusunose, H. Classification of Atomic-Scale Multipoles under Crystallographic Point Groups and Application to Linear Response Tensors. *Phys. Rev. B* **2018**, *98*, 165110. https://doi.org/10.1103/PhysRevB.98.165110.

(19) Dubovik, V. M.; Martsenyuk, M. A.; Saha, B. Material Equations for Electromagnetism with Toroidal Polarizations. *Phys. Rev. E - Stat. Physics, Plasmas, Fluids, Relat. Interdiscip. Top.* **2000**, *61* (6 B), 7087–7097. https://doi.org/10.1103/PhysRevE.61.7087.

(20) Totero Gongora, J. S.; Miroshnichenko, A. E.; Kivshar, Y. S.; Fratalocchi, A. Anapole Nanolasers for Mode-Locking and Ultrafast Pulse Generation. *Nat. Commun.* **2017**, *8*. https://doi.org/10.1038/ncomms15535.

(21) Hüttenhofer, L.; Golibrzuch, M.; Bienek, O.; Wendisch, F. J.; Lin, R.; Becherer, M.; Sharp, I. D.; Maier, S. A.; Cortés, E. Metasurface Photoelectrodes for Enhanced Solar Fuel Generation. *Adv. Energy Mater.* **2021**, *11* (46), 2102877. https://doi.org/10.1002/aenm.202102877.

(22) Grinblat, G.; Li, Y.; Nielsen, M. P.; Oulton, R. F.; Maier, S. A. Enhanced Third Harmonic Generation in Single Germanium Nanodisks Excited at the Anapole Mode. *Nano Lett.* **2016**, *16* (7), 4635–4640. https://doi.org/10.1021/acs.nanolett.6b01958.

(23) Wang, R.; Dal Negro, L. Engineering Non-Radiative Anapole Modes for Broadband Absorption Enhancement of Light. *Opt. Express* **2016**, *24* (17), 19048. https://doi.org/10.1364/OE.24.019048.

(24) Baryshnikova, K. V.; Smirnova, D. A.; Luk'yanchuk, B. S.; Kivshar, Y. S. Optical Anapoles: Concepts and Applications. *Adv. Opt. Mater.* **2019**, *7* (14), 1–13. https://doi.org/10.1002/adom.201801350.

(25) Alaee, R.; Rockstuhl, C.; Fernandez-Corbaton, I. An Electromagnetic Multipole Expansion beyond the Long-Wavelength Approximation. *Opt. Commun.* **2018**, *407*, 17–21. https://doi.org/10.1016/J.OPTCOM.2017.08.064.

(26) Radescu, E. E.; Vaman, G. Exact Calculation of the Angular Momentum Loss, Recoil Force, and Radiation Intensity for an Arbitrary Source in Terms of Electric, Magnetic, and Toroid Multipoles. *Phys. Rev. E - Stat. Physics, Plasmas, Fluids, Relat. Interdiscip. Top.* **2002**, *65* (4), 47. https://doi.org/10.1103/PhysRevE.65.046609.

(27) Fernandez-Corbaton, I.; Nanz, S.; Rockstuhl, C. On the Dynamic Toroidal Multipoles from Localized Electric Current Distributions. *Sci. Rep.* **2017**, *7* (1). https://doi.org/10.1038/s41598-017-07474-4.

(28) Zhang, M. L.; Peng, K. Q.; Fan, X.; Jie, J. S.; Zhang, R. Q.; Lee, S. T.; Wong, N. B. Preparation of Large-Area Uniform Silicon Nanowires Arrays through Metal-Assisted Chemical Etching. *J. Phys. Chem. C* **2008**, *112* (12), 4444–4450. https://doi.org/10.1021/jp077053o.

(29) Miroshnichenko, A. E.; Kivshar, Y. S. Fano Resonances in All-Dielectric Oligomers. *Nano Lett.* **2012**, *12* (12), 6459–6463. https://doi.org/10.1021/nl303927q.

(30) Dubovik, V. M.; Tugushev, V. V. Toroid Moments in Electrodynamics and Solid-State Physics. *Phys. Rep.* **1990**, *187* (4), 145–202. https://doi.org/10.1016/0370-1573(90)90042-Z.

(31) Yang, Z. J.; Deng, Y. H.; Yu, Y.; He, J. Magnetic Toroidal Dipole Response in Individual All-Dielectric Nanodisk Clusters. *Nanoscale* **2020**, *12* (19), 10639–10646. https://doi.org/10.1039/D0NR01440K.

(32) Yang, R.; Xu, J.; Shen, N. H.; Zhang, F.; Fu, Q.; Li, J.; Li, H.; Fan, Y. Subwavelength Optical Localization with Toroidal Excitations in Plasmonic and Mie Metamaterials. *InfoMat* **2021**, *3* (5), 577–597. https://doi.org/10.1002/INF2.12174.

(33) Basharin, A. A.; Kafesaki, M.; Economou, E. N.; Soukoulis, C. M.; Fedotov, V. A.; Savinov, V.; Zheludev, N. I. Dielectric Metamaterials with Toroidal Dipolar Response. https://doi.org/10.1103/PhysRevX.5.011036.

(34) Ögüt, B.; Talebi, N.; Vogelgesang, R.; Sigle, W.; Van Aken, P. A. Toroidal Plasmonic Eigenmodes in Oligomer Nanocavities for the Visible. *Nano Lett.* **2012**, *12* (10), 5239–5244. https://doi.org/10.1021/NL302418N/SUPPL_FILE/NL302418N_SI_001.PDF.

(35) Hüttenhofer, L.; Tittl, A.; Kühner, L.; Cortés, E.; Maier, S. A. Anapole-Assisted Absorption Engineering in Arrays of Coupled Amorphous Gallium Phosphide Nanodisks. *ACS Photonics* **2021**, *8* (5), 1469–1476. https://doi.org/10.1021/acsphotonics.1c00238.

(36) Miroshnichenko, A. E.; Evlyukhin, A. B.; Yu, Y. F.; Bakker, R. M.; Chipouline, A.; Kuznetsov, A. I.; Luk'yanchuk, B.; Chichkov, B. N.; Kivshar, Y. S. Nonradiating Anapole Modes in Dielectric Nanoparticles. *Nat. Commun.* **2015**, *6*, 1–8. https://doi.org/10.1038/ncomms9069.

(37) Wei, L.; Xi, Z.; Bhattacharya, N.; Urbach, H. P. Excitation of the Radiationless Anapole Mode. *Optica* **2016**, *3* (8), 799. https://doi.org/10.1364/optica.3.000799.

(38) Kerker, M.; Wang, D. S.; Giles, C. L. Electromagnetic Scattering By Magnetic Spheres. *J. Opt. Soc. Am.* **1983**, *73* (6), 765–767. https://doi.org/10.1364/JOSA.73.000765.

(39) Kruk, S.; Kivshar, Y. Functional Meta-Optics and Nanophotonics Govern by Mie Resonances. *ACS Photonics* **2017**, *4* (11), 2638–2649. https://doi.org/10.1021/ACSPHOTONICS.7B01038.

(40) Fu, Y. H.; Kuznetsov, A. I.; Miroshnichenko, A. E.; Yu, Y. F.; Luk'yanchuk, B. Directional Visible Light Scattering by Silicon Nanoparticles. *Nat. Commun.* **2013**, *4*, 1–6. https://doi.org/10.1038/ncomms2538.

(41) Lai, Y.; Cui, X.; Li, N.; Shao, L.; Zhang, W.; Wang, J.; Lin, H.-Q.; Lai, Y. H.; Cui, X. M.; Li, N. N.; Wang, J. F.; Shao, L.; Lin, H.; Zhang, W. Asymmetric Light Scattering on Heterodimers Made of Au Nanorods Vertically Standing on Au Nanodisks. *Adv. Opt. Mater.* **2021**, *9* (3), 2001595. https://doi.org/10.1002/ADOM.202001595.

(42) Albella, P.; Shibanuma, T.; Maier, S. A. Switchable Directional Scattering of Electromagnetic Radiation with Subwavelength Asymmetric Silicon Dimers. *Sci. Rep.* **2015**, *5* (1), 1–8. https://doi.org/10.1038/srep18322.

(43) Shegai, T.; Johansson, P.; Langhammer, C.; Käll, M. Directional Scattering and Hydrogen Sensing by Bimetallic Pd-Au Nanoantennas. *Nano Lett.* **2012**, *12* (5), 2464–2469. https://doi.org/10.1021/NL300558H/SUPPL_FILE/NL300558H_SI_001.PDF.

(44) Sun, S.; Wang, D.; Feng, Z.; Tan, W. Highly Efficient Unidirectional Forward Scattering Induced by Resonant Interference in a Metal–Dielectric Heterodimer. *Nanoscale* **2020**, *12* (43), 22289–22297. https://doi.org/10.1039/D0NR07010F.

(45) Vercruysse, D.; Sonnefraud, Y.; Verellen, N.; Fuchs, F. B.; Di Martino, G.; Lagae, L.; Moshchalkov, V. V.; Maier, S. A.; Van Dorpe, P. Unidirectional Side Scattering of Light by a Single-Element Nanoantenna. *Nano Lett.* **2013**, *13* (8), 3843–3849. https://doi.org/10.1021/nl401877w.

(46) Yu, Y.; Liu, J.; Yu, Y.; Qiao, D.; Li, Y.; Salas-Montiel, R. Broadband Unidirectional Transverse Light Scattering in a V-Shaped Silicon Nanoantenna. *Opt. Express* **2022**, *30* (5). https://doi.org/10.1364/OE.450943.

(47) Maksymov, I. S.; Staude, I.; Miroshnichenko, A. E.; Kivshar, Y. S. Optical Yagi-Uda Nanoantennas. *Nanophotonics* **2012**, *1* (1), 65–81. https://doi.org/10.1515/nanoph-2012-0005.

(48) Curto, A. G.; Volpe, G.; Taminiau, T. H.; Kreuzer, M. P.; Quidant, R.; Van Hulst, N. F. Unidirectional Emission of a Quantum Dot Coupled to a Nanoantenna. *Science (80-.).* **2010**, *329* (5994), 930–933. https://doi.org/10.1126/science.1191922.

(49) Krasnok, A. E.; Miroshnichenko, A. E.; Belov, P. A.; Kivshar, Y. S. All-Dielectric Optical Nanoantennas. *Opt. Express* **2012**, *20* (18), 20599. https://doi.org/10.1364/oe.20.020599.

(50) Pakizeh, T.; Käll, M. Unidirectional Ultracompact Optical Nanoantennas. *Nano Lett.* **2009**, *9* (6), 2343–2349. https://doi.org/10.1021/NL900786U.

(51) Zhu, F.; Sanz-Paz, M.; Fernández-Domínguez, A. I.; Zhuo, X.; Liz-Marzán, L. M.; Stefani, F. D.; Pilo-Pais, M.; Acuna, G. P. DNA-Templated Ultracompact Optical Antennas for Unidirectional Single-Molecule Emission. *Nano Lett.* **2022**, *22* (15), 6402–6408. https://doi.org/10.1021/acs.nanolett.2c02424.

(52) Krasnok, A. E.; Simovski, C. R.; Belov, P. A.; Kivshar, Y. S. Superdirective Dielectric Nanoantennas. *Nanoscale* **2014**, *6* (13), 7354–7361. https://doi.org/10.1039/c4nr01231c.

(53) Cihan, A. F.; Curto, A. G.; Raza, S.; Kik, P. G.; Brongersma, M. L. Silicon Mie Resonators for Highly Directional Light Emission from Monolayer MoS2. *Nat. Photonics* **2018**, *12* (5), 284–290. https://doi.org/10.1038/s41566-018-0155-y.

(54) Yeşilyurt, A. T. M.; Sanz-Paz, M.; Zhu, F.; Wu, X.; Sunil, K. S.; Acuna, G. P.; Huang, J.-S. Unidirectional Meta-Emitters Based on the Kerker Condition Assembled by DNA Origami. *ACS Nano* **2023**, *34*, 39. https://doi.org/10.1021/acsnano.3c05649.

(55) Yao, K.; Liu, Y. Controlling Electric and Magnetic Resonances for Ultracompact Nanoantennas with Tunable Directionality. *ACS Photonics* **2016**, *3* (6), 953–963. https://doi.org/10.1021/ACSPHOTONICS.5B00697.

(56) Purcell, E. M. Spontaneous Emission Probabilities at Radio Frequencies. *Phys. Rev.* **1946**, *69* (11–12), 674–674. https://doi.org/10.1103/PhysRev.69.674.2.

(57) Drexhage, K. H. Influence of a Dielectric Interface on Fluorescence Decay Time. *J. Lumin.* **1970**, *1–2* (C), 693–701. https://doi.org/10.1016/0022-2313(70)90082-7.

(58) Adachi, M.; Sugimoto, H.; Nishimura, Y.; Morita, K.; Ogino, C.; Fujii, M. Fluorophore-Decorated Mie Resonant Silicon Nanosphere for Scattering/Fluorescence Dual-Mode Imaging. *Small* **2023**, *19* (14). https://doi.org/10.1002/SMLL.202207318.

(59) Akselrod, G. M.; Argyropoulos, C.; Hoang, T. B.; Ciracì, C.; Fang, C.; Huang, J.; Smith, D. R.; Mikkelsen, M. H. Probing the Mechanisms of Large Purcell Enhancement in Plasmonic Nanoantennas. *Nat. Photonics* **2014**, *8* (11), 835–840. https://doi.org/10.1038/nphoton.2014.228.

(60) Pelton, M. Modified Spontaneous Emission in Nanophotonic Structures. *Nature Photonics*. 2015, pp 427–435. https://doi.org/10.1038/nphoton.2015.103.

(61) Muskens, O. L.; Giannini, V.; Sánchez-Gil, J. A.; Gómez Rivas, J. Strong Enhancement of the Radiative Decay Rate of Emitters by Single Plasmonic Nanoantennas. *Nano Lett.* **2007**, *7* (9), 2871–2875. https://doi.org/10.1021/NL0715847.

(62) Rolly, B.; Bebey, B.; Bidault, S.; Stout, B.; Bonod, N. Promoting Magnetic Dipolar Transition in Trivalent Lanthanide Ions with Lossless Mie Resonances. *Phys. Rev. B - Condens. Matter Mater. Phys.* **2012**, *85* (24), 245432. https://doi.org/10.1103/PhysRevB.85.245432.

(63) Feng, T.; Zhang, W.; Liang, Z.; Xu, Y.; Miroshnichenko, A. E. Isotropic Magnetic Purcell Effect. *ACS Photonics* **2018**, *5* (3), 678–683. https://doi.org/10.1021/acsphotonics.7b01016.

(64) Li, J.; Verellen, N.; Van Dorpe, P. Enhancing Magnetic Dipole Emission by a Nano-Doughnut-Shaped Silicon Disk. *ACS Photonics* **2017**, *4* (8), 1893–1898. https://doi.org/10.1021/ACSPHOTONICS.7B00509/ASSET/IMAGES/LARGE/PH-2017-00509Y_0004.JPEG.

(65) Baranov, D. G.; Savelev, R. S.; Li, S. V.; Krasnok, A. E.; Alù, A. Modifying Magnetic Dipole Spontaneous Emission with Nanophotonic Structures. *Laser Photonics Rev.* **2017**, *11* (3). https://doi.org/10.1002/LPOR.201600268.

(66) Sugimoto, H.; Fujii, M. Magnetic Purcell Enhancement by Magnetic Quadrupole Resonance of Dielectric Nanosphere Antenna. *ACS Photonics* **2021**, *8* (6), 1794–1800. https://doi.org/10.1021/acsphotonics.1c00375.

(67) Wu, D. M.; García-Etxarri, A.; Salleo, A.; Dionne, J. A. Plasmon-Enhanced Upconversion. *Journal of Physical Chemistry Letters*. American Chemical Society November 20, 2014, pp 4020–4031. https://doi.org/10.1021/jz5019042.

(68) Zhou, Z. X.; Ye, M. J.; Yu, M. W.; Yang, J. H.; Su, K. L.; Yang, C. C.; Lin, C. Y.; Babicheva, V. E.; Timofeev, I. V.; Chen, K. P. Germanium Metasurfaces with Lattice Kerker Effect in Near-Infrared Photodetectors. *ACS Nano* **2022**, *16* (4), 5994–6001. https://doi.org/10.1021/acsnano.1c11326.

(69) Ho, J.; Dong, Z.; Leong, H. S.; Zhang, J.; Tjiptoharsono, F.; Rezaei, S. D.; Hwa Goh, K. C.; Wu, M.; Li, S.; Chee, J.; Yu Wong, C. P.; Kuznetsov, A. I.; Yang, J. K. W. Miniaturizing Color-Sensitive Photodetectors via Hybrid Nanoantennas toward Submicrometer Dimensions. *Sci. Adv.* **2022**, *8* (47). https://doi.org/10.1126/sciadv.add3868.

(70) Li, W.; Valentine, J. Metamaterial Perfect Absorber Based Hot Electron Photodetection. *Nano Lett.* **2014**, *14* (6), 3510–3514. https://doi.org/10.1021/nl501090w.

(71) Garín, M.; Fenollosa, R.; Alcubilla, R.; Shi, L.; Marsal, L. F.; Meseguer, F. All-Silicon Spherical-Mie-Resonator Photodiode with Spectral Response in the Infrared Region. *Nat. Commun.* **2014**, *5* (1), 3440. https://doi.org/10.1038/ncomms4440.

(72) Hüttenhofer, L.; Eckmann, F.; Lauri, A.; Cambiasso, J.; Pensa, E.; Li, Y.; Cortés, E.; Sharp, I. D.; Maier, S. A. Anapole Excitations in Oxygen-Vacancy-Rich TiO2- x Nanoresonators: Tuning the Absorption for Photocatalysis in the Visible Spectrum. *ACS Nano* **2020**, *14* (2), 2456–2464. https://doi.org/10.1021/acsnano.9b09987.

(73) Zhang, T.; Che, Y.; Chen, K.; Xu, J.; Xu, Y.; Wen, T.; Lu, G.; Liu, X.; Wang, B.; Xu, X.; Duh, Y. S.; Tang, Y. L.; Han, J.; Cao, Y.; Guan, B. O.; Chu, S. W.; Li, X. Anapole Mediated Giant Photothermal Nonlinearity in Nanostructured Silicon. *Nat. Commun.* **2020**, *11* (1), 1–9. https://doi.org/10.1038/s41467-020-16845-x.

(74) González-Colsa, J.; Olarte-Plata, J. D.; Bresme, F.; Albella, P. Enhanced Thermo-Optical Response by Means of Anapole Excitation. *J. Phys. Chem. Lett.* **2022**, *13* (26), 6230–6235. https://doi.org/10.1021/acs.jpclett.2c00870.

(75) Zograf, G. P.; Petrov, M. I.; Zuev, D. A.; Dmitriev, P. A.; Milichko, V. A.; Makarov, S. V.; Belov, P. A. Resonant Nonplasmonic Nanoparticles for Efficient Temperature-Feedback Optical Heating. *Nano Lett.* **2017**, *17* (5), 2945–2952. https://doi.org/10.1021/acs.nanolett.7b00183.

(76) Grinblat, G.; Li, Y.; Nielsen, M. P.; Oulton, R. F.; Maier, S. A. Efficient Third Harmonic Generation and Nonlinear Subwavelength Imaging at a Higher-Order Anapole Mode in a Single Germanium Nanodisk. *ACS Nano* **2017**, *11* (1), 953–960. https://doi.org/10.1021/acsnano.6b07568.

(77) Kruk, S. S.; Camacho-Morales, R.; Xu, L.; Rahmani, M.; Smirnova, D. A.; Wang, L.; Tan, H. H.; Jagadish, C.; Neshev, D. N.; Kivshar, Y. S. Nonlinear Optical Magnetism Revealed by Second-Harmonic Generation in Nanoantennas. *Nano Lett.* **2017**, *17* (6), 3914–3918. https://doi.org/10.1021/acs.nanolett.7b01488.

(78) Ashkin, A.; Dziedzic, J. M.; Bjorkholm, J. E.; Chu, S. Observation of a Single-Beam Gradient Force Optical Trap for Dielectric Particles. *Opt. Angular Momentum* **2016**, *11* (5), 196–198. https://doi.org/10.1364/ol.11.000288.

(79) Lukas Novotny, B. H. *Principles of Nano-Optics*, Second Edi.; Cambridge University Press, 2012.

(80) Canós Valero, A.; Kislov, D.; Gurvitz, E. A.; Shamkhi, H. K.; Pavlov, A. A.; Redka, D.;

Yankin, S.; Zemánek, P.; Shalin, A. S. Nanovortex-Driven All-Dielectric Optical Diffusion Boosting and Sorting Concept for Lab-on-a-Chip Platforms. *Adv. Sci.* **2020**, *7* (11). https://doi.org/10.1002/advs.201903049.

(81) Hong, I.; Anyika, T.; Hong, C.; Yang, S.; Ndukaife, J. C. Hybrid Optical and Diffusiophoretic Nanomanipulation Using All-Dielectric Anapole-Enhanced Thermonanophotonics. *ACS Photonics* **2023**. https://doi.org/10.1021/ACSPHOTONICS.3C00983.

(82) Zhang, Y.; Min, C.; Dou, X.; Wang, X.; Urbach, H. P.; Somekh, M. G.; Yuan, X. Plasmonic Tweezers: For Nanoscale Optical Trapping and Beyond. *Light: Science and Applications*. 2021, pp 2047–7538. https://doi.org/10.1038/s41377-021-00474-0.

(83) Hong, I.; Hong, C.; Tutanov, O. S.; Massick, C.; Castleberry, M.; Zhang, Q.; Jeppesen, D. K.; Higginbotham, J. N.; Franklin, J. L.; Vickers, K.; Coffey, R. J.; Ndukaife, J. C. Anapole-Assisted Low-Power Optical Trapping of Nanoscale Extracellular Vesicles and Particles. *Nano Lett.* **2023**, *23*, 7507. https://doi.org/10.1021/acs.nanolett.3c02014.

(84) Xu, Z.; Song, W.; Crozier, K. B. Optical Trapping of Nanoparticles Using All-Silicon Nanoantennas. *ACS Photonics* **2018**, *5* (12), 4993–5001. https://doi.org/10.1021/acsphotonics.8b01250.

(85) Chen, M. K.; Wu, Y.; Feng, L.; Fan, Q.; Lu, M.; Xu, T.; Tsai, D. P. Principles, Functions, and Applications of Optical Meta-Lens. *Adv. Opt. Mater.* **2021**, *9* (4). https://doi.org/10.1002/ADOM.202001414.

(86) Lee, G. Y.; Sung, J.; Lee, B. Metasurface Optics for Imaging Applications. *MRS Bull.* **2020**, *45* (3), 202–209. https://doi.org/10.1557/mrs.2020.64.

(87) Engelberg, J.; Levy, U. The Advantages of Metalenses over Diffractive Lenses. *Nat. Commun. 2020 111* **2020**, *11* (1), 1–4. https://doi.org/10.1038/s41467-020-15972-9.

(88) Paniagua-Domínguez, R.; Yu, Y. F.; Khaidarov, E.; Choi, S.; Leong, V.; Bakker, R. M.; Liang, X.; Fu, Y. H.; Valuckas, V.; Krivitsky, L. A.; Kuznetsov, A. I. A Metalens with a Near-Unity Numerical Aperture. *Nano Lett.* **2018**, *18* (3), 2124–2132. https://doi.org/10.1021/ACS.NANOLETT.8B00368.

(89) Feng, T.; Xu, Y.; Liang, Z.; Zhang, W. All-Dielectric Hollow Nanodisk for Tailoring Magnetic Dipole Emission. *Opt. Lett.* **2016**, *41* (21), 5011. https://doi.org/10.1364/ol.41.005011.

(90) Ni, X.; Emani, N. K.; Kildishev, A. V.; Boltasseva, A.; Shalaev, V. M. Broadband Light Bending with Plasmonic Nanoantennas. *Science*. American Association for the Advancement of Science January 27, 2012, p 427. https://doi.org/10.1126/science.1214686.

(91) Yu, N.; Genevet, P.; Kats, M. A.; Aieta, F.; Tetienne, J. P.; Capasso, F.; Gaburro, Z. Light Propagation with Phase Discontinuities: Generalized Laws of Reflection and Refraction. *Science (80-.).* **2011**, *334* (6054), 333–337. https://doi.org/10.1126/science.1210713.

(92) Paniagua-Domínguez, R.; Yu, Y. F.; Khaidarov, E.; Choi, S.; Leong, V.; Bakker, R. M.; Liang, X.; Fu, Y. H.; Valuckas, V.; Krivitsky, L. A.; Kuznetsov, A. I. A Metalens with a Near-Unity Numerical Aperture. *Nano Lett.* **2018**, *18* (3), 2124–2132. https://doi.org/10.1021/acs.nanolett.8b00368.

(93) Yang, Y.; Kravchenko, I. I.; Briggs, D. P.; Valentine, J. All-Dielectric Metasurface Analogue of Electromagnetically Induced Transparency. *Nat. Commun.* **2014**, *5*. https://doi.org/10.1038/ncomms6753.

(94) Yang, Y.; Wang, W.; Boulesbaa, A.; Kravchenko, I. I.; Briggs, D. P.; Puretzky, A.; Geohegan, D.; Valentine, J. Nonlinear Fano-Resonant Dielectric Metasurfaces. *Nano Lett* **2015**, *15*, 7388–7393. https://doi.org/10.1021/acs.nanolett.5b02802.

(95) Kravets, V. G.; Kabashin, A. V; Barnes, W. L.; Grigorenko, A. N. Plasmonic Surface

Lattice Resonances: A Review of Properties and Applications. *Chemical Reviews*. 2018, pp 5912–5951. https://doi.org/10.1021/acs.chemrev.8b00243.

(96) Babicheva, V. E. Lattice Effect in Mie-Resonant Dielectric Nanoparticle Array under Oblique Light Incidence. *MRS Commun.* **2018**, *8* (4), 1455–1462. https://doi.org/10.1557/mrc.2018.216.

(97) Babicheva, V. E.; Moloney, J. V. Lattice Effect Influence on the Electric and Magnetic Dipole Resonance Overlap in a Disk Array. *Nanophotonics* **2018**, *7* (10), 1663–1668. https://doi.org/10.1515/nanoph-2018-0107.

(98) Castellanos, G. W.; Bai, P.; Gómez Rivas, J. Lattice Resonances in Dielectric Metasurfaces. *J. Appl. Phys.* **2019**, *125* (21). https://doi.org/10.1063/1.5094122.

(99) Hsu, C. W.; Zhen, B.; Stone, A. D.; Joannopoulos, J. D.; Soljacic, M. Bound States in the Continuum. *Nature Reviews Materials*. Nature Publishing Group July 19, 2016, pp 1–13. https://doi.org/10.1038/natrevmats.2016.48.

(100) Koshelev, K.; Lepeshov, S.; Liu, M.; Bogdanov, A.; Kivshar, Y. Asymmetric Metasurfaces with High- Q Resonances Governed by Bound States in the Continuum. *Phys. Rev. Lett.* **2018**, *121* (19), 193903. https://doi.org/10.1103/PhysRevLett.121.193903.

(101) Liu, S.; Vaskin, A.; Addamane, S.; Leung, B.; Tsai, M. C.; Yang, Y.; Vabishchevich, P. P.; Keeler, G. A.; Wang, G.; He, X.; Kim, Y.; Hartmann, N. F.; Htoon, H.; Doorn, S. K.; Zilk, M.; Pertsch, T.; Balakrishnan, G.; Sinclair, M. B.; Staude, I.; Brener, I. Light-Emitting Metasurfaces: Simultaneous Control of Spontaneous Emission and Far-Field Radiation. *Nano Lett.* **2018**, *18* (11), 6906–6914. https://doi.org/10.1021/acs.nanolett.8b02808.

(102) Zhang, X.; Liu, Y.; Han, J.; Kivshar, Y.; Song, Q. Chiral Emission from Resonant Metasurfaces. *Science (80-.).* **2022**, *377* (6611), 1215–1218. https://doi.org/10.1126/science.abq7870.

(103) Zhang, Z.; Xu, C.; Liu, C.; Lang, M.; Zhang, Y.; Li, M.; Lu, W.; Chen, Z.; Wang, C.; Wang, S.; Li, X. Dual Control of Enhanced Quasi-Bound States in the Continuum Emission from Resonant c-Si Metasurfaces. *Nano Lett.* **2023**, *27*, 26. https://doi.org/10.1021/acs.nanolett.3c02148.

(104) Tian, J.; Li, Q.; Belov, P. A.; Sinha, R. K.; Qian, W.; Qiu, M. High- Q All-Dielectric Metasurface: Super and Suppressed Optical Absorption. *ACS Photonics* **2020**, *7* (6), 1436–1443. https://doi.org/10.1021/acsphotonics.0c00003.

(105) Woltersdorff, W. Uber Die Optischen Konstanten Diinner MetaUschichten Im Langwelligen Ultrarot. *Zeitschrift für Phys.* **1934**, *91*, 230.

(106) Tian, J.; Luo, H.; Li, Q.; Pei, X.; Du, K.; Qiu, M. Near-Infrared Super-Absorbing All-Dielectric Metasurface Based on Single-Layer Germanium Nanostructures. *Laser Photonics Rev.* **2018**, *12* (9). https://doi.org/10.1002/lpor.201800076.

(107) Kim, S. J.; Park, J.; Esfandyarpour, M.; Pecora, E. F.; Kik, P. G.; Brongersma, M. L. Superabsorbing, Artificial Metal Films Constructed from Semiconductor Nanoantennas. *Nano Lett* **2016**, *16*. https://doi.org/10.1021/acs.nanolett.6b01198.

(108) Fan, S.; Suh, W.; Joannopoulos, J. D. Temporal Coupled-Mode Theory for the Fano Resonance in Optical Resonators. *J. Opt. Soc. Am. A* **2003**, *20* (3), 569–572.

(109) Piper, J. R.; Liu, V.; Fan, S. Total Absorption by Degenerate Critical Coupling. *Appl. Phys. Lett.* **2014**, *104* (25), 251110. https://doi.org/10.1063/1.4885517/891654.

(110) Xu, R.; Takahara, J. All-Dielectric Perfect Absorber Based on Quadrupole Modes. *Opt. Lett.* **2021**, *46* (15), 3596. https://doi.org/10.1364/ol.431398.

(111) Tian, J.; Luo, H.; Li, Q.; Pei, X.; Du, K.; Qiu, M. Near-Infrared Super-Absorbing All-Dielectric Metasurface Based on Single-Layer Germanium Nanostructures. *Laser Photonics Rev.* **2018**, *12* (9), 1800076. https://doi.org/10.1002/lpor.201800076.

(112) Yang, C. Y.; Yang, J. H.; Yang, Z. Y.; Zhou, Z. X.; Sun, M. G.; Babicheva, V. E.; Chen, K. P. Nonradiating Silicon Nanoantenna Metasurfaces as Narrowband Absorbers. *ACS Photonics* **2018**, *5* (7), 2596–2601. https://doi.org/10.1021/acsphotonics.7b01186.

(113) Zhou, Z. X.; Ye, M. J.; Yu, M. W.; Yang, J. H.; Su, K. L.; Yang, C. C.; Lin, C. Y.; Babicheva, V. E.; Timofeev, I. V.; Chen, K. P. Germanium Metasurfaces with Lattice Kerker Effect in Near-Infrared Photodetectors. *ACS Nano* **2022**, *16* (4), 5994–6001. https://doi.org/10.1021/acsnano.1c11326.

(114) Tseng, M. L.; Jahani, Y.; Leitis, A.; Altug, H. Dielectric Metasurfaces Enabling Advanced Optical Biosensors. *ACS Photonics* **2021**, *8* (1), 47–60. https://doi.org/10.1021/ACSPHOTONICS.0C01030.

(115) Moitra, P.; Slovick, B. A.; Li, W.; Kravchencko, I. I.; Briggs, D. P.; Krishnamurthy, S.; Valentine, J. Large-Scale All-Dielectric Metamaterial Perfect Reflectors. *ACS Photonics* **2015**, *2* (6), 692–698. https://doi.org/10.1021/ACSPHOTONICS.5B00148.

(116) Huang, Y.; Xu, H.; Lu, Y.; Chen, Y. All-Dielectric Metasurface for Achieving Perfect Reflection at Visible Wavelengths. *J. Phys. Chem. C* **2018**, *122* (5), 2990–2996. https://doi.org/10.1021/ACS.JPCC.7B10417/ASSET/IMAGES/LARGE/JP-2017-104178_0006.JPEG.

(117) Li, Z.; Kong, X.; Zhang, J.; Shao, L.; Zhang, D.; Liu, J.; Wang, X.; Zhu, W.; Qiu, C. W. Cryptography Metasurface for One-Time-Pad Encryption and Massive Data Storage. *Laser Photon. Rev.* **2022**, *16* (8), 2200113. https://doi.org/10.1002/LPOR.202200113.

(118) Zheng, P.; Dai, Q.; Li, Z.; Ye, Z.; Xiong, J.; Liu, H. C.; Zheng, G.; Zhang, S. Metasurface-Based Key for Computational Imaging Encryption. *Sci. Adv.* **2021**, *7* (21), 363–384. https://doi.org/10.1126/SCIADV.ABG0363/SUPPL_FILE/ABG0363_SM.PDF.

(119) Kim, J.; Jeon, D.; Seong, J.; Badloe, T.; Jeon, N.; Kim, G.; Kim, J.; Baek, S.; Lee, J. L.; Rho, J. Photonic Encryption Platform via Dual-Band Vectorial Metaholograms in the Ultraviolet and Visible. *ACS Nano* **2022**, *16* (3), 3546–3553. https://doi.org/10.1021/ACSNANO.1C10100/SUPPL_FILE/NN1C10100_SI_001.PDF.

(120) Kaelberer, T.; Fedotov, V. A.; Papasimakis, N.; Tsai, D. P.; Zheludev, N. I. Toroidal Dipolar Response in a Metamaterial. *Science (80-.).* **2010**, *330* (6010), 1510–1512. https://doi.org/10.1126/science.1197172.

(121) Huang, Y.-W.; Chen, W. T.; Wu, P. C.; Fedotov, V.; Savinov, V.; Ho, Y. Z.; Chau, Y.-F.; Zheludev, N. I.; Tsai, D. P. Design of Plasmonic Toroidal Metamaterials at Optical Frequencies. *Opt. Express* **2012**, *20* (2), 1760. https://doi.org/10.1364/oe.20.001760.

(122) Liu, Z.; Du, S.; Cui, A.; Li, Z.; Fan, Y.; Chen, S.; Li, W.; Li, J.; Gu, C. High-Quality-Factor Mid-Infrared Toroidal Excitation in Folded 3D Metamaterials. *Adv. Mater.* **2017**, *29* (17). https://doi.org/10.1002/adma.201606298.

(123) Zhang, G.; Lan, C.; Gao, R.; Wen, Y.; Zhou, J. Toroidal Dipole Resonances in All-Dielectric Oligomer Metasurfaces. *Adv. Theory Simulations* **2019**, *2* (10), 1900123. https://doi.org/10.1002/ADTS.201900123.

(124) Tuz, V. R.; Khardikov, V. V.; Kivshar, Y. S. All-Dielectric Resonant Metasurfaces with a Strong Toroidal Response. *ACS Photonics* **2018**, *5* (5), 1871–1876. https://doi.org/10.1021/ACSPHOTONICS.8B00098/SUPPL_FILE/PH8B00098_SI_003.AVI.

(125) Bao, Y.; Zhu, X.; Fang, Z. Plasmonic Toroidal Dipolar Response under Radially Polarized Excitation. *Sci. Rep.* **2015**, *5*, 11793. https://doi.org/10.1038/srep11793.

(126) Ahmadivand, A.; Semmlinger, M.; Dong, L.; Gerislioglu, B.; Nordlander, P.; Halas, N. J. Toroidal Dipole-Enhanced Third Harmonic Generation of Deep Ultraviolet Light Using Plasmonic Meta-Atoms. *Nano Lett.* **2019**, *19* (1), 605–611. https://doi.org/10.1021/ACS.NANOLETT.8B04798/ASSET/IMAGES/MEDIUM/NL-

2018-04798C_M002.GIF.

(127) Algorri, J. F.; Zografopoulos, D. C.; Ferraro, A.; García-Cámara, B.; Vergaz, R.; Beccherelli, R.; Sánchez-Pena, J. M. Anapole Modes in Hollow Nanocuboid Dielectric Metasurfaces for Refractometric Sensing. *Nanomaterials* **2019**, *9* (1). https://doi.org/10.3390/nano9010030.

(128) Han, B.; Li, X.; Sui, C.; Diao, J.; Jing, X.; Hong, Z. Analog of Electromagnetically Induced Transparency in an E-Shaped All-Dielectric Metasurface Based on Toroidal Dipolar Response. *Opt. Mater. Express* **2018**, *8* (8), 2197. https://doi.org/10.1364/ome.8.002197.

(129) Zografopoulos, D. C.; Ferraro, A.; Algorri, J. F.; Martín-Mateos, P.; García-Cámara, B.; Moreno-Oyervides, A.; Krozer, V.; Acedo, P.; Vergaz, R.; Sánchez-Pena, J. M.; Beccherelli, R. All-Dielectric Silicon Metasurface with Strong Subterahertz Toroidal Dipole Resonance. *Adv. Opt. Mater.* **2019**, *7* (19). https://doi.org/10.1002/adom.201900777.

(130) Liu, S.-D.; Wang, Z.-X.; Wang, W.-J.; Chen, J.-D.; Chen, Z.-H. High Q-Factor with the Excitation of Anapole Modes in Dielectric Split Nanodisk Arrays. *Opt. Express* **2017**, *25* (19), 22375. https://doi.org/10.1364/oe.25.022375.

(131) Gupta, M.; Singh, R. Toroidal Metasurfaces in a 2D Flatland. *Reviews in Physics*. 2020. https://doi.org/10.1016/j.revip.2020.100040.

(132) Ahmadivand, A.; Gerislioglu, B.; Ahuja, R.; Mishra, Y. K. Toroidal Metaphotonics and Metadevices. *Laser and Photonics Reviews*. 2020. https://doi.org/10.1002/lpor.201900326.

(133) Jeong, J.; Goldflam, M. D.; Campione, S.; Briscoe, J. L.; Vabishchevich, P. P.; Nogan, J.; Sinclair, M. B.; Luk, T. S.; Brener, I. High Quality Factor Toroidal Resonances in Dielectric Metasurfaces. *ACS Photonics* **2020**, *7* (7), 1699–1707. https://doi.org/10.1021/acsphotonics.0c00179.

(134) Tripathi, A.; Kim, H. R.; Tonkaev, P.; Lee, S. J.; Makarov, S. V; Kruk, S. S.; Rybin, M. V; Park, H. G.; Kivshar, Y. Lasing Action from Anapole Metasurfaces. *Nano Lett.* **2021**, *21* (15), 6563–6568. https://doi.org/10.1021/acs.nanolett.1c01857.

(135) Cui, C.; Yuan, S.; Qiu, X.; Zhu, L.; Wang, Y.; Li, Y.; Song, J.; Huang, Q.; Zeng, C.; Xia, J. Light Emission Driven by Magnetic and Electric Toroidal Dipole Resonances in a Silicon Metasurface. *Nanoscale* **2019**, *11* (30), 14446–14454. https://doi.org/10.1039/c9nr03172c.

(136) Conteduca, D.; Brunetti, G.; Barth, I.; Quinn, S. D.; Ciminelli, C.; Krauss, T. F. Multiplexed Near-Field Optical Trapping Exploiting Anapole States. *ACS Nano* **2023**, *17*, 16695–16702. https://doi.org/10.1021/acsnano.3c03100.

(137) Zenin, V. A.; Evlyukhin, A. B.; Novikov, S. M.; Yang, Y.; Malureanu, R.; Lavrinenko, A. V.; Chichkov, B. N.; Bozhevolnyi, S. I. Direct Amplitude-Phase Near-Field Observation of Higher-Order Anapole States. *Nano Lett.* **2017**, *17* (11), 7152–7159. https://doi.org/10.1021/acs.nanolett.7b04200.

(138) Totero Gongora, J. S.; Favraud, G.; Fratalocchi, A. Fundamental and High-Order Anapoles in All-Dielectric Metamaterials via Fano-Feshbach Modes Competition. *Nanotechnology* **2017**, *28* (10), 104001. https://doi.org/10.1088/1361-6528/aa593d.

(139) Zhou, C.; Li, S.; Wang, Y.; Zhan, M. Multiple Toroidal Dipole Fano Resonances of Asymmetric Dielectric Nanohole Arrays. *Phys. Rev. B* **2019**, *100* (19), 195306. https://doi.org/10.1103/PhysRevB.100.195306.

(140) Galli, M.; Portalupi, S. L.; Belotti, M.; Andreani, L. C.; O'Faolain, L.; Krauss, T. F. Light Scattering and Fano Resonances in High-Q Photonic Crystal Nanocavities. *Appl. Phys. Lett.* **2009**, *94* (7), 71101. https://doi.org/10.1063/1.3080683.

(141) Mie resonance-based dielectric metamaterials | Elsevier Enhanced Reader https://reader.elsevier.com/reader/sd/pii/S1369702109703189?token=D64F15BCDD6CADD882929FA744BF0D5CC6B286595E2ED06C332179A3CB0F88DC72A015667C6A0B470B0B91719FC6F232 (accessed Jun 15, 2020).

(142) Odebo Länk, N.; Verre, R.; Johansson, P.; Käll, M. Large-Scale Silicon Nanophotonic Metasurfaces with Polarization Independent Near-Perfect Absorption. *Nano Lett.* **2017**, *17* (5), 3054–3060. https://doi.org/10.1021/acs.nanolett.7b00416.

(143) Inoue, A.; Sugimoto, H.; Fujii, M. Photoluminescence Enhancement of Silicon Quantum Dot Monolayer by Double Resonance Plasmonic Substrate. *J. Phys. Chem. C* **2017**, *121* (21), 11609–11615. https://doi.org/10.1021/acs.jpcc.7b00717.

(144) Sugimoto, H.; Fujii, M.; Imakita, K.; Hayashi, S.; Akamatsu, K. Codoping N- and p-Type Impurities in Colloidal Silicon Nanocrystals: Controlling Luminescence Energy from below Bulk Band Gap to Visible Range. *J. Phys. Chem. C* **2013**, *117* (22), 11850–11857. https://doi.org/10.1021/jp4027767.

(145) Hinamoto, T.; Hamada, M.; Sugimoto, H.; Fujii, M. Angle-, Polarization-, and Wavelength-Resolved Light Scattering of Single Mie Resonators Using Fourier-Plane Spectroscopy. *Adv. Opt. Mater.* **2021**, *9* (8), 2002192. https://doi.org/10.1002/adom.202002192.

(146) Bharadwaj, P.; Novotny, L. Spectral Dependence of Single Molecule Fluorescence Enhancement. *Opt. Express* **2007**, *15* (21), 14266. https://doi.org/10.1364/oe.15.014266.

(147) Sugimoto, H.; Fujii, M.; Fukuda, Y.; Imakita, K.; Akamatsu, K. All-Inorganic Water-Dispersible Silicon Quantum Dots: Highly Efficient near-Infrared Luminescence in a Wide PH Range. *Nanoscale* **2014**, *6* (1), 122–126. https://doi.org/10.1039/c3nr03863g.

(148) Furuta, K.; Fujii, M.; Sugimoto, H.; Imakita, K. Energy Transfer in Silicon Nanocrystal Solids Made from All-Inorganic Colloidal Silicon Nanocrystals. *J. Phys. Chem. Lett.* **2015**, *6* (14), 2761–2766. https://doi.org/10.1021/acs.jpclett.5b01067.

(149) Lindsey, C. P.; Patterson, G. D. Detailed Comparison of the Williams-Watts and Cole-Davidson Functions. *J. Chem. Phys.* **1980**, *73* (7), 3348–3357. https://doi.org/10.1063/1.440530.

(150) Allison, R. R.; Downie, G. H.; Cuenca, R.; Hu, X. H.; Childs, C. J. H.; Sibata, C. H. Photosensitizers in Clinical PDT. *Photodiagnosis Photodyn. Ther.* **2004**, *1* (1), 27–42. https://doi.org/10.1016/S1572-1000(04)00007-9.

(151) Esswein, A. J.; Nocera, D. G. Hydrogen Production by Molecular Photocatalysis. *Chemical Reviews*. 2007, pp 4022–4047. https://doi.org/10.1021/cr050193e.

(152) Zhao, J.; Wu, W.; Sun, J.; Guo, S. Triplet Photosensitizers: From Molecular Design to Applications. *Chem. Soc. Rev.* **2013**, *42* (12), 5323–5351. https://doi.org/10.1039/c3cs35531d.

(153) DeRosa, M. C.; Crutchley, R. J. Photosensitized Singlet Oxygen and Its Applications. *Coordination Chemistry Reviews*. Elsevier 2002, pp 351–371. https://doi.org/10.1016/S0010-8545(02)00034-6.

(154) Zhao, J.; Ji, S.; Guo, H. Triplet-Triplet Annihilation Based Upconversion: From Triplet Sensitizers and Triplet Acceptors to Upconversion Quantum Yields. *RSC Advances*. 2011, pp 937–950. https://doi.org/10.1039/c1ra00469g.

(155) Singh-Rachford, T. N.; Castellano, F. N. Photon Upconversion Based on Sensitized Triplet-Triplet Annihilation. *Coordination Chemistry Reviews*. November 2010, pp 2560–2573. https://doi.org/10.1016/j.ccr.2010.01.003.

(156) Glaser, F.; Wenger, O. S. Sensitizer-Controlled Photochemical Reactivity via Upconversion of Red Light. *Chem. Sci.* **2022**, *14* (1), 149–161. https://doi.org/10.1039/d2sc05229f.

(157) Barron, L. D.; Gray, C. G. The Multipole Interaction Hamiltonian for Time Dependent Fields. *J. Phys. A Gen. Phys.* **1973**, *6* (1), 59–61. https://doi.org/10.1088/0305-4470/6/1/006.

(158) Bellary, V. P.; Balasubramanian, T. K. On the Rotational Intensity Distribution in the A1Δg → X3Σg- Magnetic Dipole Transition of Oxygen Molecule. *J. Mol. Spectrosc.* **1987**, *126* (2), 436–442. https://doi.org/10.1016/0022-2852(87)90248-7.

(159) Baryshnikov, G.; Minaev, B.; Ågren, H. Theory and Calculation of the Phosphorescence Phenomenon. *Chem. Rev.* **2017**, *117* (9), 6500–6537. https://doi.org/10.1021/acs.chemrev.7b00060.

(160) Sugimoto, H.; Fujii, M. Magnetic Purcell Enhancement by Magnetic Quadrupole Resonance of Dielectric Nanosphere Antenna. *ACS Photonics* **2021**, *8* (6), 1794–1800. https://doi.org/10.1021/acsphotonics.1c00375.

(161) Vaskin, A.; Mashhadi, S.; Steinert, M.; Chong, K. E.; Keene, D.; Nanz, S.; Abass, A.; Rusak, E.; Choi, D. Y.; Fernandez-Corbaton, I.; Pertsch, T.; Rockstuhl, C.; Noginov, M. A.; Kivshar, Y. S.; Neshev, D. N.; Noginova, N.; Staude, I. Manipulation of Magnetic Dipole Emission from Eu 3+ with Mie-Resonant Dielectric Metasurfaces. *Nano Lett.* **2019**, *19* (2), 1015–1022. https://doi.org/10.1021/acs.nanolett.8b04268.

(162) Guez, D.; Markovitsi, D.; Sommerauer, M.; Hanack, M. Photophysical Properties of a Ruthenium(II)Phthalocyanine. *Chem. Phys. Lett. ELSEVIER Chem. Phys. Lett.* **1996**, *249*, 309–313.

(163) Ishii, K.; Shiine, M.; Shimizu, Y.; Hoshino, S. I.; Abe, H.; Sogawa, K.; Kobayashi, N. Control of Photobleaching in Photodynamic Therapy Using the Photodecarbonylation Reaction of Ruthenium Phthalocyanine Complexes via Stepwise Two-Photon Excitation. *J. Phys. Chem. B* **2008**, *112* (10), 3138–3143. https://doi.org/10.1021/jp076118k.

(164) Hasebe, H.; Sugimoto, H.; Hinamoto, T.; Fujii, M. Coupled Toroidal Dipole Modes in Silicon Nanodisk Metasurface: Polarization Independent Narrow Band Absorption and Directional Emission. *Adv. Opt. Mater.* **2020**, *8* (22). https://doi.org/10.1002/adom.202001148.

(165) Sortino, L.; Zotev, P. G.; Mignuzzi, S.; Cambiasso, J.; Schmidt, D.; Genco, A.; Aßmann, M.; Bayer, M.; Maier, S. A.; Sapienza, R.; Tartakovskii, A. I. Enhanced Light-Matter Interaction in an Atomically Thin Semiconductor Coupled with Dielectric Nano-Antennas. *Nat. Commun.* **2019**, *10* (1), 5119. https://doi.org/10.1038/s41467-019-12963-3.

(166) Wang, P.; Qin, F.; Zhang, Z.; Cao, W. Quantitative Monitoring of the Level of Singlet Oxygen Using Luminescence Spectra of Phosphorescent Photosensitizer. *Opt. Express* **2015**, *23* (18), 22991. https://doi.org/10.1364/oe.23.022991.

(167) Ijaz, M.; Ghassemlooy, Z.; Rajbhandari, S.; Le Minh, H.; Perez, J.; Gholami, A. Comparison of 830 Nm and 1550 Nm Based Free Space Optical Communications Link under Controlled Fog Conditions. In *Proceedings of the 2012 8th International Symposium on Communication Systems, Networks and Digital Signal Processing, CSNDSP 2012*; 2012. https://doi.org/10.1109/CSNDSP.2012.6292739.

(168) Bünzli, J. C. G.; Eliseeva, S. V. Lanthanide NIR Luminescence for Telecommunications, Bioanalyses and Solar Energy Conversion. *J. Rare Earths* **2010**, *28* (6), 824–842. https://doi.org/10.1016/S1002-0721(09)60208-8.

(169) Yamada, H.; Chu, T.; Ishida, S.; Arakawa, Y. Si Photonic Wire Waveguide Devices. *IEEE J. Sel. Top. Quantum Electron.* **2006**, *12* (6), 1371–1378. https://doi.org/10.1109/JSTQE.2006.880611.

(170) Kaushal, H.; Kaddoum, G. Optical Communication in Space: Challenges and Mitigation Techniques. *IEEE Communications Surveys and Tutorials*. 2017, pp 57–96. https://doi.org/10.1109/COMST.2016.2603518.

(171) Du, H.; Shi, H.; Liu, Y.; Zeng, D.; Mei, T. Towards NIR-VIS Masked Face Recognition. *IEEE Signal Process. Lett.* **2021**, *28*, 768–772. https://doi.org/10.1109/LSP.2021.3071663.

(172) He, R.; Wu, X.; Sun, Z.; Tan, T. Wasserstein CNN: Learning Invariant Features for NIR-VIS Face Recognition. *IEEE Trans. Pattern Anal. Mach. Intell.* **2019**, *41* (7), 1761–1773. https://doi.org/10.1109/TPAMI.2018.2842770.

(173) He, Q.; Lou, M.; Zheng, C.; Ye, W.; Wang, Y.; Tittel, F. K. Repetitively Mode-Locked Cavity-Enhanced Absorption Spectroscopy (RML-CEAS) for near-Infrared Gas Sensing. *Sensors (Switzerland)* **2017**, *17* (12), 2792. https://doi.org/10.3390/s17122792.

(174) Escobedo, J. O.; Rusin, O.; Lim, S.; Strongin, R. M. NIR Dyes for Bioimaging Applications. *Curr. Opin. Chem. Biol.* **2010**, *14* (1), 64–70. https://doi.org/10.1016/j.cbpa.2009.10.022.

(175) Li, Y.; Liu, Y.; Li, Q.; Zeng, X.; Tian, T.; Zhou, W.; Cui, Y.; Wang, X.; Cheng, X.; Ding, Q.; Wang, X.; Wu, J.; Deng, H.; Li, Y.; Meng, X.; Deng, Z.; Hong, X.; Xiao, Y. Novel NIR-II Organic Fluorophores for Bioimaging beyond 1550 Nm. *Chem. Sci.* **2020**, *11* (10), 2621–2626. https://doi.org/10.1039/c9sc06567a.

(176) Hong, G.; Antaris, A. L.; Dai, H. Near-Infrared Fluorophores for Biomedical Imaging. *Nat. Biomed. Eng.* **2017**, *1* (1), 1–22. https://doi.org/10.1038/s41551-016-0010.

(177) Knight, M. W.; Sobhani, H.; Nordlander, P.; Halas, N. J. Photodetection with Active Optical Antennas. *Science (80-.).* **2011**, *332* (6030), 702–704. https://doi.org/10.1126/science.1203056.

(178) Tanzid, M.; Ahmadivand, A.; Zhang, R.; Cerjan, B.; Sobhani, A.; Yazdi, S.; Nordlander, P.; Halas, N. J. Combining Plasmonic Hot Carrier Generation with Free Carrier Absorption for High-Performance Near-Infrared Silicon-Based Photodetection. *ACS Photonics* **2018**, *5* (9), 3472–3477. https://doi.org/10.1021/acsphotonics.8b00623.

(179) Sobhani, A.; Knight, M. W.; Wang, Y.; Zheng, B.; King, N. S.; Brown, L. V.; Fang, Z.; Nordlander, P.; Halas, N. J. Narrowband Photodetection in the Near-Infrared with a Plasmon-Induced Hot Electron Device. *Nat. Commun.* **2013**, *4* (1), 1–6. https://doi.org/10.1038/ncomms2642.

(180) Cao, J.; Sun, T.; Grattan, K. T. V. Gold Nanorod-Based Localized Surface Plasmon Resonance Biosensors: A Review. *Sensors and Actuators, B: Chemical*. Elsevier B.V. 2014, pp 332–351. https://doi.org/10.1016/j.snb.2014.01.056.

(181) Logan, D. F.; Knights, A. P.; Jessop, P. E.; Tarr, N. G. Defect-Enhanced Photo-Detection at 1550 Nm in a Silicon Waveguide Formed via LOCOS. *Semicond. Sci. Technol.* **2011**, *26* (4), 045009. https://doi.org/10.1088/0268-1242/26/4/045009.

(182) Fard, S. T.; Murray, K.; Caverley, M.; Donzella, V.; Flueckiger, J.; Grist, S. M.; Huante-Ceron, E.; Schmidt, S. A.; Kwok, E.; Jaeger, N. A. F.; Knights, A. P.; Chrostowski, L. Silicon-on-Insulator Sensors Using Integrated Resonance-Enhanced Defect-Mediated Photodetectors. *Opt. Express* **2014**, *22* (23), 28517. https://doi.org/10.1364/oe.22.028517.

(183) Bradley, J. D. B.; Jessop, P. E.; Knights, A. P. Silicon Waveguide-Integrated Optical Power Monitor with Enhanced Sensitivity at 1550 Nm. *Appl. Phys. Lett.* **2005**, *86* (24), 1–3. https://doi.org/10.1063/1.1947379.

(184) Reiter, S.; Koper, N.; Reineke-Koch, R.; Larionova, Y.; Turcu, M.; Krügener, J.; Tetzlaff, D.; Wietler, T.; Höhne, U.; Kähler, J. D.; Brendel, R.; Peibst, R. Parasitic Absorption in Polycrystalline Si-Layers for Carrier-Selective Front Junctions. In *Energy Procedia*; Elsevier, 2016; Vol. 92, pp 199–204. https://doi.org/10.1016/j.egypro.2016.07.057.

(185) Casalino, M.; Coppola, G.; De La Rue, R. M.; Logan, D. F. State-of-the-Art All-Silicon Sub-Bandgap Photodetectors at Telecom and Datacom Wavelengths. *Laser and Photonics Reviews*. John Wiley & Sons, Ltd November 1, 2016, pp 895–921. https://doi.org/10.1002/lpor.201600065.

(186) Fan, S.; Suh, W.; Joannopoulos, J. D. Temporal Coupled-Mode Theory for the Fano Resonance in Optical Resonators. *J. Opt. Soc. Am. A* **2003**, *20* (3), 569. https://doi.org/10.1364/josaa.20.000569.

(187) Piper, J. R.; Liu, V.; Fan, S. Total Absorption by Degenerate Critical Coupling. *Appl. Phys. Lett.* **2014**, *104* (25), 251110. https://doi.org/10.1063/1.4885517.

(188) Parker, J. A.; Sugimoto, H.; Coe, B.; Eggena, D.; Fujii, M.; Scherer, N. F.; Gray, S. K.; Manna, U. Excitation of Nonradiating Anapoles in Dielectric Nanospheres. *Phys. Rev. Lett.* **2020**, *124* (9). https://doi.org/10.1103/PhysRevLett.124.097402.

(189) Xu, L.; Rahmani, M.; Zangeneh Kamali, K.; Lamprianidis, A.; Ghirardini, L.; Sautter, J.; Camacho-Morales, R.; Chen, H.; Parry, M.; Staude, I.; Zhang, G.; Neshev, D.; Miroshnichenko, A. E. Boosting Third-Harmonic Generation by a Mirror-Enhanced Anapole Resonator. *Light Sci. Appl.* **2018**, *7* (1). https://doi.org/10.1038/s41377-018-0051-8.

(190) Timofeeva, M.; Lang, L.; Timpu, F.; Renaut, C.; Bouravleuv, A.; Shtrom, I.; Cirlin, G.; Grange, R. Anapoles in Free-Standing III-V Nanodisks Enhancing Second-Harmonic Generation. *Nano Lett.* **2018**, *18* (6), 3695–3702. https://doi.org/10.1021/acs.nanolett.8b00830.

(191) Baranov, D. G.; Verre, R.; Karpinski, P.; Käll, M. Anapole-Enhanced Intrinsic Raman Scattering from Silicon Nanodisks. *ACS Photonics* **2018**, *5* (7), 2730–2736. https://doi.org/10.1021/acsphotonics.8b00480.

(192) Fan, H. Y.; Ramdas, A. K. Infrared Absorption and Photoconductivity in Irradiated Silicon. *J. Appl. Phys.* **1959**, *30* (8), 1127–1134. https://doi.org/10.1063/1.1735282.

(193) Xu, T.; Wheeler, M. S.; Ruda, H. E.; Mojahedi, M.; Aitchison, J. S. The Influence of Material Absorption on the Quality Factor of Photonic Crystal Cavities. *Opt. Express* **2009**, *17* (10), 8343. https://doi.org/10.1364/oe.17.008343.

(194) Yesilkoy, F.; Arvelo, E. R.; Jahani, Y.; Liu, M.; Tittl, A.; Cevher, V.; Kivshar, Y.; Altug, H. Ultrasensitive Hyperspectral Imaging and Biodetection Enabled by Dielectric Metasurfaces. *Nature Photonics*. Nature Publishing Group June 1, 2019, pp 390–396. https://doi.org/10.1038/s41566-019-0394-6.

(195) Tseng, M. L.; Jahani, Y.; Leitis, A.; Altug, H. Dielectric Metasurfaces Enabling Advanced Optical Biosensors. *ACS Photonics*. 2021, pp 47–60. https://doi.org/10.1021/acsphotonics.0c01030.

(196) Wang, J.; Kühne, J.; Karamanos, T.; Rockstuhl, C.; Maier, S. A.; Tittl, A. All-Dielectric Crescent Metasurface Sensor Driven by Bound States in the Continuum. *Adv. Funct. Mater.* **2021**, *31* (46). https://doi.org/10.1002/adfm.202104652.

(197) Algorri, J. F.; Zografopoulos, D. C.; Ferraro, A.; García-Cámara, B.; Beccherelli, R.; Sánchez-Pena, J. M. Ultrahigh-Quality Factor Resonant Dielectric Metasurfaces Based on Hollow Nanocuboids. *Opt. Express* **2019**, *27* (5), 6320. https://doi.org/10.1364/oe.27.006320.

(198) Fuemmeler, E. G.; Sanders, S. N.; Pun, A. B.; Kumarasamy, E.; Zeng, T.; Miyata, K.; Steigerwald, M. L.; Zhu, X. Y.; Sfeir, M. Y.; Campos, L. M.; Ananth, N. A Direct Mechanism of Ultrafast Intramolecular Singlet Fission in Pentacene Dimers. *ACS Cent. Sci.* **2016**, *2* (5), 316–324. https://doi.org/10.1021/acscentsci.6b00063.

(199) Matsuda, S.; Oyama, S.; Kobori, Y. Electron Spin Polarization Generated by Transport of Singlet and Quintet Multiexcitons to Spin-Correlated Triplet Pairs during Singlet Fissions. *Chem. Sci.* **2020**, *11* (11), 2934–2942. https://doi.org/10.1039/c9sc04949e.

(200) Moriasa, K.; Hasebe, H.; Sugimoto, H.; Fujii, M. Bound States in the Continuum (BIC) in Silicon Nanodisk Array on Mirror Structure: Perfect Absorption Associated with Quasi-BIC below the Bandgap. *J. Appl. Phys.* **2023**, *133* (17). https://doi.org/10.1063/5.0146896.

List of Achievement

Publications

[1](Chapter 2,Chapter 3) Hiroaki Hasebe, Hiroshi Sugimoto, Tatsuki Hinamoto, Minoru Fujii, "Coupled Toroidal Dipole Modes in Silicon Nanodisk Metasurface: Polarization Independent Narrow Band Absorption and Directional Emission", Advanced Optical Materials, Vol. 20, Issue 22 pp.2001148 (2020).

[2](Chapter 6) Hiroaki Hasebe, Keisuke Moriasa, Kaito Yamashita, Hiroshi Sugimoto, Minoru Fujii, "Toroidal dipole-induced photocurrent enhancement in Si nanodisk hexagonal array below the band gap", ACS Photonics, Vol. 9, Issue 10, pp.3302-3309 (2022).

[3](Chapter 4) Hiroshi Sugimoto, Hiroaki Hasebe, Taniyuki Furuyama and Minoru Fujii, "Direct excitation of triplet state of molecule by enhanced magnetic field of dielectric metasurfaces", Small, Vol. 17, Issue 47, pp.2104458 (2021)

[4](Chapter 5) Hiroaki Hasebe, Hiroshi Sugimoto, Yoshino Katsurayama, Taniyuki Furuyama, Minoru Fujii, "Photosensitizing Metasurface Empowered by Enhanced Magnetic Field of Toroidal Dipole Resonance", Small, Vol. , Issue , pp. 230519 (2023)

[5] Keisuke Moriasa, Hiroaki Hasebe, Hiroshi Sugimoto, Minoru Fujii, "Bound States in the Continuum (BIC) in Silicon Nanodisk Array on Mirror Structure: Perfect Absorption Associated with Quasi-BIC below the Band Gap", Journal of Applied Physics, Vol. 133, Issue 17, pp.173102 (2023)

[6] Sumana Paul, Joydip Ghosh, Tarik Hossain, Hiroaki Hasebe, Hiroshi Sugimoto, Minoru Fujii, Pravat Giri, "Interfacial Charge Transfer Induced Enhanced Near-Infrared Photoluminescence and Enhanced Visible Photodetection in 2D/0D Bi2Se3/CsPbBr2I Heterojunction with Type-I Band Alignment", The Journal of Physical Chemistry C, Vol. 126, Issue 39, pp.16721-16731 (2022).

Conference

- International conference

[1](Oral) Hiroaki Hasebe, Hiroshi Sugimoto, Minoru Fujii, “Enhancing Forbidden Transition in Molecules by Toroidal Dipole Metasurface for Novel Photochemical Reactions”, EL16.13.04, 2023 MRS Spring Meeting, April 10-14(2023), San Francisco(USA)

[2](Oral) Hiroaki Hasebe, Hiroshi Sugimoto, Minoru Fujii, “Near Infrared Absorption and Photocurrent Enhancement by Coupled Toroidal Dipole Modes in Silicon Metasurfaces”, EQ05.21.05, 2021 MRS Fall Meeting, December 6-8, Virtual Meeting

- Domestic conference

[3] (口頭)長谷部　宏明, 杉本　泰, 古山　渓行, 藤井　稔, “誘電体メタサーフェスによる分子の S-T 吸収と光反応への応用”, 講演番号　3D02, 2023 年光化学討論会, 2023 年 9 月 5-7 日, 広島国際会議場

[4] (Oral)Hiroaki Hasebe、Hiroshi Sugimoto、Minoru Fujii, "Enhancement of photosensitizing activity of ruthenium complex by resonant dielectric nanodisk array" 講演番号 20p-C304-9, 2022 年度 第 83 回応用物理学会秋季学術講演会、 2022 年 9 月 20~23 日、 東北大学 川内キャンパス, JSAP-OSA Joint Symposia

[5] (口頭)長谷部　宏明、森朝　啓介、杉本　泰、藤井　稔, "シリコンナノディスクアナポールメタサーフェスによる狭帯域近赤外吸収" session 5, 2022 年 PICS 研究会 2022 年 7 月 14,15 日, グランドホテル浜松

[6] (ポスター)長谷部　宏明 、杉本　泰、古山　渓行、藤井　稔"シリコンメタサーフェスによる分子のスピン反転励起増強" 講演番号 P-20, 応用物理学会関西支部 2021 年度第 2 回応用物理学会秋季学術講演会、2021 年 10 月 15 日 、オンライン

[7] (口頭)長谷部　宏明 、杉本　泰、古山　渓行、藤井　稔, "誘電体メタサーフェスによる一重項ー三重項遷移増強" 講演番号 13p-N324-9, 2021 年 第 82 回応用物理学会秋季学術講演会、2021 年 9 月 10~13 日(口頭発表)、9 月 21~23 日(ポスター発表) 、オンライン

[8] (口頭)長谷部　宏明、杉本　泰、雛本　樹生、藤井　稔　"誘電体メタサーフェスのトロイダル双極子共鳴による発光特性制御" "講演番号 19a-Z08-6", 2021 年 第 68 回応用物理学会春季学術講演会、2021 年 3 月 16-19 日 、オンライン

[9] 長谷部　宏明、杉本　泰、雛本　樹生、藤井　稔 "トロイダル双極子結合によるシリコンメタサーフェスの吸収増強” 講演番号 IB-40, 2020 年 第 31 回光物性研究会、2020 年 12 月 11,12 日 、オンライン

[10] 長谷部　宏明、杉本　泰、雛本　樹生、藤井　稔　"高屈折率誘電体ナノディスクアレイの形成と光学応答制御(II)" 講演番号 11a-Z17-10, 2020 年 第 81 回応用物理学会秋季学術講演会、2020 年 9 月 8-11 日 、オンライン

[11] 長谷部　宏明、雛本　樹生、杉本　泰、藤井　稔　"高屈折率誘電体ナノディスクアレイの光学応答制御" Poster number B20, 2019 年 神戸大学研究基盤センター「若手フロンティア研究会 2019」、2019 年 12 月 19 日、神戸大学百年記念館

[12] 長谷部　宏明、雛本　樹生、杉本　泰、藤井　稔, "高屈折率誘電体ナノディスクアレイの大面積形成と光学応答制御（I）" 講演番号　19p-PA6-13, 2019 年 第 80 回応用物理学会秋季学術講演会、2019 年 9 月 18―21 日、北海道大学　札幌キャンパス

Award

[1] 電子情報通信学会　PICS 研究会 学生講演奨励賞　2022 年 7 月 15 日

[2] 竹水会優秀論文賞 2021 年 3 月 15 日

神戸大学博士論文「トロイダル双極子共鳴を有するシリコンメタサーフェスの開発と応用」全 119 頁
提出日 2024 年 1 月 17 日

Doctor Thesis, Kobe University
“Development and Application of Silicon Metasurface with Toroidal Dipole Resonance”

119pages

Submitted on January 17th, 2024
When published on the Kobe University institution repository */Kernel/,* the publication date shall appear in the cover of the repository version.